CHARACTERIZATION OF HYDROGEN-TERMINATED DIAMOND DEVICES FOR EXTREME ENVIRONMENT APPLICATIONS

A DISSERTATION
SUBMITTED TO THE DEPARTMENT OF ELECTRICAL ENGINEERING
AND THE COMMITTEE ON GRADUATE STUDIES
OF STANFORD UNIVERSITY
IN PARTIAL FULFILLMENT OF THE REQUIREMENTS
FOR THE DEGREE OF
DOCTOR OF PHILOSOPHY

Ricardo Peterson

December 2020

This dissertation is online at: http://purl.stanford.edu/jv865pq0434

I certify that I have read this dissertation and that, in my opinion, it is fully adequate in scope and quality as a dissertation for the degree of Doctor of Philosophy.

Debbie Senesky, Primary Adviser

I certify that I have read this dissertation and that, in my opinion, it is fully adequate in scope and quality as a dissertation for the degree of Doctor of Philosophy.

Srabanti Chowdhury

I certify that I have read this dissertation and that, in my opinion, it is fully adequate in scope and quality as a dissertation for the degree of Doctor of Philosophy.

Krishna Saraswat

Approved for the Stanford University Committee on Graduate Studies.

Stacey F. Bent, Vice Provost for Graduate Education

This signature page was generated electronically upon submission of this dissertation in electronic format. An original signed hard copy of the signature page is on file in University Archives.

Abstract

This thesis presents diamond as a promising platform for devices and electronics for harsh environment operation. However, the theme of this work is not to present wildly innovative device architectures, but rather, to gain an understanding of the properties that substantiate the promise of new materials for devices. Namely, for the case of diamond, the experimental electrical performance is thus far limited. To realize diamond's full potential, it is therefore essential to illuminate the fundamental barriers that inhibit its performance. This thesis is dedicated to this understanding.

In the first part of this thesis, a fabrication process for hydrogen-terminated diamond (H:diamond) devices is presented. Moreover, a theoretical model is developed to understand the hole mobility of the *p*-type conductive channel on the diamond surface (2DHG). The model is used to fit to experimental measurements to demonstrate that multiple mobility-limiting mechanisms exist for the diamond surface conductive channel, and one of these mechanisms are widely unaccounted for in literature.

Next, H:diamond-based field effect transistor operation is demonstrated. The transfer characteristics exhibit high ON/OFF ratios and good sub-threshold slopes. Further, the oxide quality is robust, as shown by the capacitance measurements, as well as the high-temperature Hall-effect measurements up to 700 K. The resistance to radiation was demonstrated by irradiating the diamond substrates to 2 MeV proton irradiation at multiple fluences. It was shown that negative charge build-up is generated in the oxide, which degrades the mobility and enhances the 2DHG accumulation (thus increasing the sheet density). In order to illuminate all of the mobility-limiting mechanisms as induced via irradiation, unpassivated H:diamond samples were also irradiated. It was shown that the conductivity also decreased. It is reasoned that lattice damage is unlikely the cause of this degradation. Rather, the degradation is likely caused by the proton-induced ionization, which can dissociate the C-H surface dipoles. These results further support the conclusion that surface disorder related to the C-H dipoles contributes significantly to the degraded 2DHG mobility.

Finally, this thesis contributes to a well-known phenomenon related to the irradiation-induced annealing. This is in the context of 3C-silicon carbide (SiC), which, also has a diamond crystal structure. When defective 3C-SiC is irradiated with high-energy ions, annealing is observed. Similar effects are observed in other polytypes, such as 4H-SiC. It is demonstrated that when such ionization events occur in the vicinity of high electric fields, the annealing effect can be enhanced. This provides avenues for applications requiring low-temperature and localized annealing solutions.

Acknowledgments

I would like to thank all of those who have aided me throughout my life, and over the past five years. The work presented in this thesis could not have been possible without the support of my colleagues, friends, and family.

I met my advisor, Prof. Debbie Senesky, in February of 2015 during a campus visit day for new admits. At the time, I was unsure which group I would ultimately join, but I always had the XLab in mind in the months that followed. Once I rotated with the XLab, my desire to stay was a quick decision. Debbie somehow made our technical discussions something to look forward to the most, and her feedback and mentorship have instilled professional and personal virtues that I will carry on indefinitely. I have no doubt that she has always acted in my best interests, whether that meant challenging me or lifting my spirits. For these reasons and more, I thank Debbie dearly.

I have also had the fortune to work alongside a fantastic team of researchers. I thank (in no particular order!) Dr. Ateeq Suria, Dr. Caitlin Chapin, Dr. Karen Dowling, Dr. Ananth Yalamarthy, Dr. Minmin Hu, Dr. Ruth Miller, Dr. Hannah Alpert, Dr. Jessica Frick, Dr. Saleh Kargarrazi, Dr. Hoang-Phuong Phan, Savannah Benbrook, Tom Heuser, Ruiqi Chen, Max Holliday, Chen Liu, Anand Lalwani, Jiya Janowitz, and other XLabbers for the enlightening discussions and positive spirits.

It would also like to thank my reading committee, Prof. Krishna Saraswat and Prof. Srabanti Chowdhury. From the beginning of my PhD, Prof. Saraswat was always very welcoming in his office. For years, I would turn to Prof. Saraswat's advice and the notes I saved from his courses EE311 and EE312. His guidance and expertise was immensly appreciated.

I remember meeting with Prof. Chowdhury when she was interviewed at Stanford, and was immediately thrilled that she would join the EE faculty. It has been an immense pleasure having multiple technical discussions, and I am grateful for her insight. I would also like to thank her lab members, especially Mohamad Malakoutian. It was a pleasure working alongside him at UC Davis. Although the drives to Davis were long, I always looked forward to them (to be

honest, they gave me the time to catch up with my podcasts!). Mohamad was constantly open to collaboration and technical discussions, which made much of the work in this thesis possible.

Special thanks to Yongqiang Wong and his team from the Los Alamos National Laboratory. They were very welcome when I visited the facilities. I also appreciate their flexibility in accommodating my irradiation runs, despite being occupied running many other experiments.

In addition, my work would not have been possible without the SNF and SNSF staff. Special thanks to Xiaoqing Xu for her expertise and guidance, as well as to Michelle Rincon, Graham Ewing, Jim Haydon, Carsen Kline, Swaroop Kommera, and the rest of the staff. They have always been swift in resolving equipment issues, and they have always been open to providing insight to a wide range of processes. Facility users are lucky to have such an amazing staff.

On a personal note, I would like to acknowledge those who have supported me in my life. First and foremost, my mother and father. Thus far, I have spent my young adult life traveling the world and receiving an incredible education. In short, I have pursued my dreams relentlessly. As I write these words, I regret never having asked my parents what their dreams were. As immigrants, they spent their young adult years working tirelessly to provide for their children, all while adapting to a new culture. Their sacrifices were immense, and I have tried my best to compensate with my accomplishments. I hope I have made them proud.

On that note, my sister Alex and brother Daniel have always been the most fun and supportive siblings that one can ask for. I feel most at home in their presence. My sister's children, Liam, Oliver, and Lincoln, lift our spirits like no one else. With no offense to the rest of my family, I look forward to seeing my nephews the most when I return home!

Finally, I reserve my final gratitude for my beloved wife, Mavi. She has been nothing short of an enormous blessing. Since I have met her, she has been a beacon of hope and joy, shining brighter by the day. Words cannot express my emotions.

Contents

List of Tables

List of Figures

Chapter 1

Introduction

1.1 Wide Band-gap Semiconductors for Harsh Environment Applications

Wide band-gap materials have long gifted us with the capacity to design technology that is capable of operating in the harshest conditions. Such conditions arise inevitably by the forces of nature, whether it is in the depths of terrestrial boreholes or on the surface of celestial bodies in space. Moreover, harsh conditions arise within our own inventions, such as in gas turbines, electric vehicles, or nuclear reactors. The moment one wishes to probe and quantify a quantity in such a harsh environment, a need arises for electronics (e.g., transistors, sensors, etc.) that are robust enough to sustain those conditions. For this reason, quantitative information within harsh environments is as precious as it is difficult to obtain. It paves new avenues for curious minds, and can enable solutions to important problems. In aircraft, for example, monitoring the air-to-fuel ratio and combustion temperatures of the turbine is necessary to improve efficiency, reduce emissions, and provide crucial information for quality control [1]. Automobiles usually require chemical sensors in their exhaust, which should operate at temperatures exceeding 300°C [2, 3]. On the other hand, the study of Venus (which has an average surface temperature of 460°C) may answer deep questions regarding Earth's fate as it grapples with greenhouse gas emissions. Venus probes are extremely difficult to engineer, the most recent being the Soviet Venera 13 from 1982, which survived a mere two hours due to thermal failure of the on-board electronics [4]. On the other temperature extreme, cryogenic electronics are necessary for space applications and highly sensitive sensors [5, 6]. A diagram depicting this is shown in Fig. 1.1. Thus, in the dedicated efforts of designing electronics for harsh environment applications, the structural and electronic

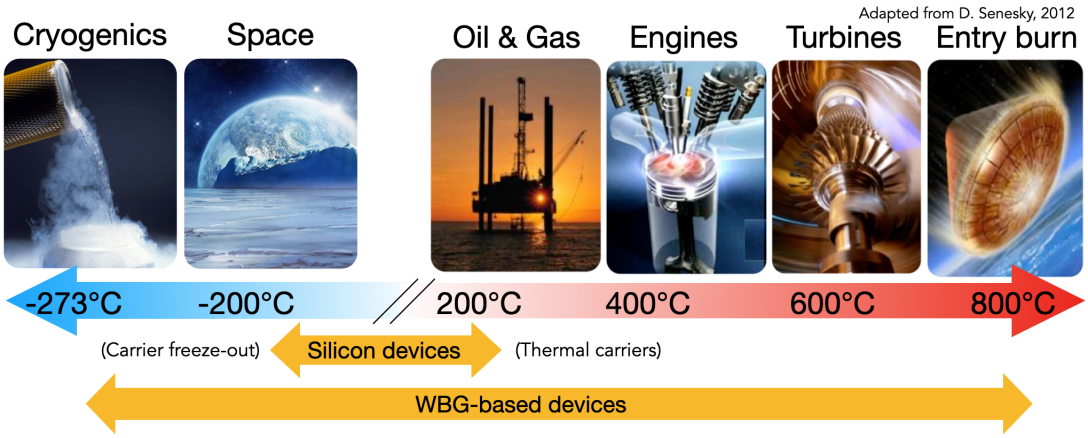

Figure 1.1: Temperature operation range of silicon and special WBG-based heterostructures. The potential for WBG technology spans a vast range of temperature environments, making it attractive for harsh environment applications. One example of such a heterostructure, as discussed in this thesis, is oxide-passivated hydrogen-terminated diamond.

properties of wide band-gap semiconductor materials have been of great interest for decades.

1.2 State-of-the-Art Harsh Environment Electronics

Researchers continue to push the limits of robust electronics for harsh environment applications by exploiting the fundamental properties of the underlying semiconducting materials. This also includes circumventing any drawbacks imposed by these properties and the fabrication process, such as in sub-par carrier mobilities and difficulties in doping. The most widely used semiconductor is silicon, owing to its highly developed supply chain. Unfortunately, due to its low band-gap of 1.12 eV, silicon-based technology is vulnerable at temperatures exceeding 150°C since its intrinsic regions (or, indeed, any region that must be insulating for proper device operation) become conductive. The heat dissipation and current leakage that ensue are thus unacceptable. Moreover, in power electronics, attractive material properties include a high electric field breakdown and a high thermal conductivity, both of which are sub-par in silicon.

Due to the aforementioned limitations, alternative materials with much larger bandgaps are desired. These are known as wide bandgap (WBG) materials, examples of which include silicon carbide (SiC), gallium nitride (GaN), and diamond. The former two, SiC and GaN, are well studied materials whose hexagonal crystal structures have band-gaps ranging around 3.4 eV. Although this bandgap is 3x that of silicon, the electric field breakdown is over 10x, and the device operation can remain stable at temperatures exceeding 700°C. Moreover, the drift saturation velocity is superior in SiC and GaN, which can enable more efficient power conversion systems.

Lastly, each atom within SiC and GaN is energetically more stable than in silicon. Thus, WBG materials can usually operate robustly in radiation-rich environments, as it takes more energy to displace an atom and induce crystal defects.

Diamond, however, is a special WBG material that remains largely unexplored. Owing to the tight lattice spacing of carbon, diamond exhibits exceptional material properties that can be exploited for operation in harsh conditions. Table 1.1 summarizes the various the key properties for Si, 4H-SiC, GaN, and diamond [7, 8]. Of these properties, diamond exceeds in the parameters that are most critical for high temperature, high power, and high frequency operation.

1.3 Diamond's Potential for Harsh Environment Operation

It is a cherished fortune that diamond, the material possessing the highest thermal conductivity, happens to be a WBG semiconductor with superb electrical properties. Additionally, diamond is chemically inert to most corrosive substances, which makes it robust for reactive environments. Despite the importance of all these material properties, diamond would not be nearly as attractive without its wide bandgap of 5.5 eV. The extent to which WBG materials allow for high temperature operation can be most elegantly expressed by their intrinsic carrier concentration n_i as a function of temperature. The temperature dependent n_i is given by

$$n_i = \sqrt{N_c N_v} \exp\left(-E_g/(k_B T)\right), \tag{1.1}$$

where N_c and N_v are the conduction and valence band density of states, k_B is the Boltzmann constant, T is temperature. Fig. 1.2 shows this relationship for Si, GaN, and diamond. It is evident from this plot that Si is subpar for high temperature operation. For example, n_i for Si

Table 1.1: Material parameters for various semiconductor materials [7, 8].

Parameter	Si	4H-SiC	GaN	Diamond
Bandgap (eV)	1.12	3.26	3.45	5.5
Dielectric Constant	11.9	10.1	10.4	5.7
Critical Electric Field (MV/cm)	0.3	2.2	3.9	13
Electron Mobility ($cm^2/(V\cdot s)$)	1500	900	2260	4500
Hole Mobility ($cm^2/(V\cdot s)$)	600	115	850	3800
Thermal Conductivity ($W/(m\cdot K)$)	150	490	230	2290-3450
Saturation Velocity ($\times 10^7$ m/s)	1.0	2	2.2	1.3(h), 2.3(e)

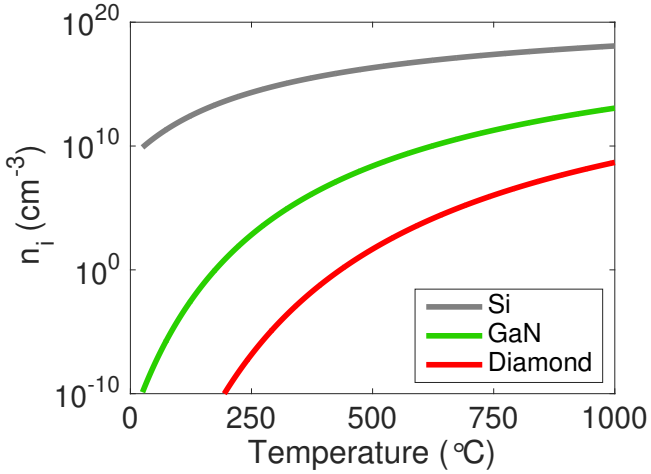

Figure 1.2: Intrinsic carrier concentration for Si, GaN, and diamond.

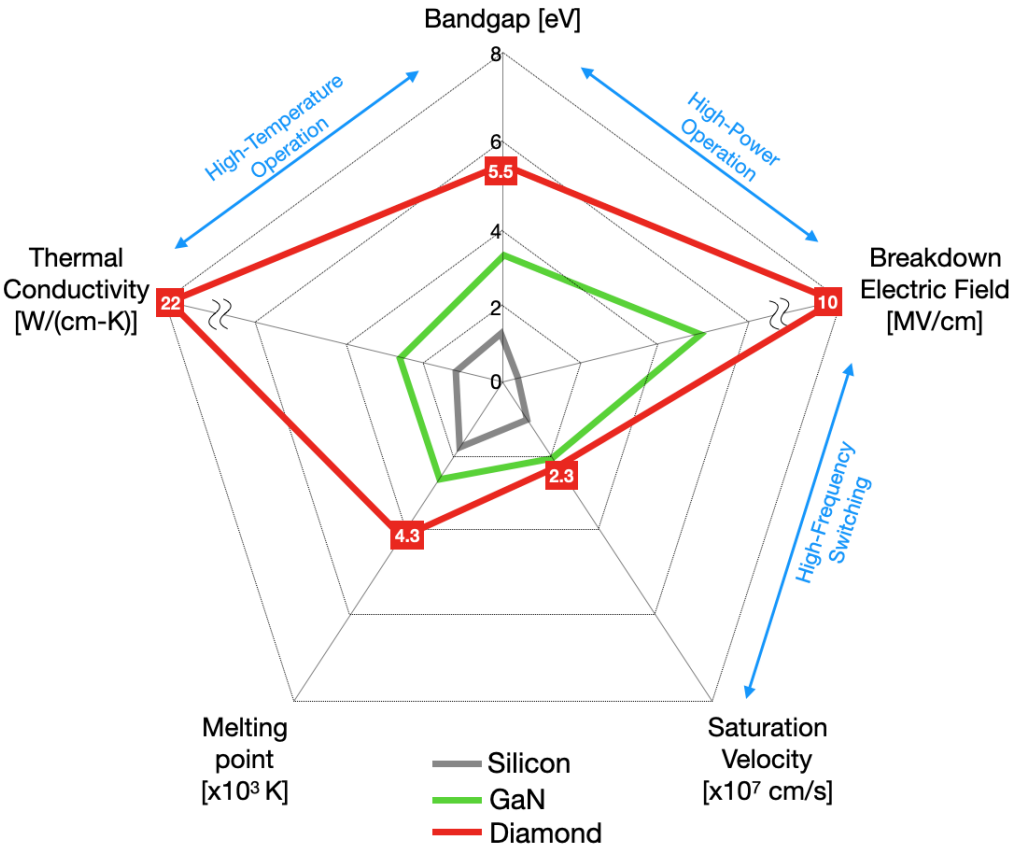

Figure 1.3: Comparison of properties for Si, GaN, and diamond.

begins to exceed $\sim 10^{15}$ cm^{-2} at 300°C, at which point the conductivity of all regions, doped or undoped, begins to rise significantly. By comparison, at this same temperature, WBG materials such as GaN or diamond have approximate intrinsic concentrations of 10^5 and 10^{-5} cm^{-2}, respectively. Diamond is especially attractive, given that temperatures as high as 1000°C still yield very low n_i values ($\sim 10^8$ cm^{-2}). Thus, these theoretical indicators solidify the potential for diamond-based electronics for high temperature and high power applications. A diagram demonstrating this across multiple properties is shown in Fig. 1.3.

As diamond-based technology is advancing in all fronts, it is finding greater use in industry and the research community. Unfortunately, one drawback of diamond is in increasing its conductivity via dopants. As will be discussed in this thesis, a special configuration of diamond, known as hydrogen-terminated diamond, allows its surface to conduct despite the lack of dopants. This is attractive in that the activation and deactivation behavior of dopants is circumvented, and robust operation across a wide temperatures can be achieved (Fig. 1.1).

Due to reliability constraints, industries are dependent on materials like diamond for electronic applications, including aerospace & defense [9], lasers & optics [10], and other R&D [11]. Satellite communications and military equipment, for example, have a great demand for high power and high frequency device operation. Additionally, research facilities, such as in nuclear and high energy physics, can exploit diamond's inherent hardness for radiation detection [12]. Finally, the laser and optics community find great use of diamond, owing to its relatively constant absorption and dielectric constant across wide wavelengths, as well as its small thermal expansion coefficient (which suppresses thermal lensing effects).

1.3.1 Advancing technology

Of course, challenges are expected for any immature technology. Other WBG materials have had their share of immense scrutiny, and have now matured to become a semiconductor that is increasingly adopted for various applications. For example, for decades, researchers attempted to reduce the defect density of GaN, which was a challenging feat due to the lack of native substrates and thermal expansion coefficient mismatches [13]. Moreover, unintentional doping and sub-par electron mobility values were difficult to optimize [14, 15]. Nonetheless, the market demand for GaN-based technology has expanded significantly, owing to the research development in growth techniques, fabrication processes, and structural designs.

The interest for diamond applications is, in part, driven by the advances made in synthesizing large-area substrates [8]. Diamond is routinely synthesized using microwave plasma chemical vapor deposition (MPCVD). Substantial progress has been made on this front, allowing the

growth of nanocrystalline, polycrystalline, and single-crystalline diamond [8]. Using MPCVD, ultra-high diamond quality has been demonstrated, with impurities on the order of a few parts-per-billion and moderate dislocation densities. This applies to growth thicknesses ranging from nanometers to millimeters, and diameters reaching 2 inches [16, 17]. The MPCVD method also permits the growth of multiple diamond films with varying properties, such as in doping. The growth techniques for large-area substrates have been attempted, including homoepitaxial, heteroepitaxial, and mosiac tiling growth [18, 19]. Multiple companies have arisen as a result of these methods, which they use to profit from diamond applications and sequentially contribute in advancing the synthesis process. Many challenges remain, however. Among these are the vacuum chamber constraints (which limits scaling), straining issues (as seen in heteroepitaxial growth methods), dopant activation (especially n-type), and sub-par experimental conductivity (a main topic of this thesis) [8]. To optimize the performance of diamond-based electronics, these issues need to be addressed.

The design and fabrication of the devices on diamond is equally critical in the research and development process. Fundamentally, this involves identifying the hurdles that are limiting their development. Stable metal contacts (ohmic and Schottky), oxide passivation, etching, and cleaning/polishing are among the many steps that must be understood in the fabrication process. Unique challenges are also posed by the constraints of operating these devices in harsh conditions, such as in metal contact diffusion and non-linearities related to dopant activation. To resolve the aforementioned limitations, a thorough understanding of their underlying mechanisms is required. Poor contact behavior, for example, may be a limiting factor at high temperature operation, which calls for an in-depth analysis of the metal/diamond interface. In this thesis, one such limiting factor in diamond – a low hole-channel mobility that is frequently observed – is studied in depth. Given the fundamental nature of semiconductor transport properties, the impact of this study spans every researcher who is dedicated to the advancement of this technology.

1.4 Major Contributions

The major contributions of this work are the following:

- A micro-fabrication process has been developed for diamond-based devices, including field effect transistors and hall-effect devices. Operational stability at high temperatures and transfer characteristics have been demonstrated.
- A scattering model has been developed to model the hole mobility for a wide range of

temperatures. A multi-band treatment of diamond valence bands was included by using a Schrödinger/Poisson solver.

- Experimental Hall-effect measurements for wide temperature ranges was performed to deduce the various mechanisms that are degrading the hole mobility, including one mechanism that has been largely overlooked.

- Performance of proton-irradiated H:diamond devices has been shown for the first time. It was demonstrated that Al_2O_3 builds up negative bulk charge. More importantly, it was demonstrated that irradiation-induced ionization degraded the hole mobility and sheet density, an effect attributed to the dissociation of C-H dipoles at the surface. This study provides a holistic understanding of the degradation mechanisms of all H:diamond devices, passivated or not.

- It is shown, via modeling, that defective silicon carbide can be annealed via heavy-ion irradiation, and that this annealing can be enhanced in the presence of high background fields. This deepens our understanding of irradiated diamond-like materials, as well as advances fabrication processing technology for low-temperature annealing solutions.

1.5 Thesis Overview

- Chapter 2 provides a background overview of the diamond technology described in this thesis and lays the technical foundation for the reader to understand the details presented in the subsequent chapters. First, the surface conduction properties is reviewed, including the physical properties of various diamond terminations and surface transfer doping. This is followed by a background of the experimentally-measured and theoretically-calculated hole mobilities. Finally, ionizing radiation in semiconductors and its physical manifestations are discussed.

- Chapter 3 discusses the fabrication process of devices on hydrogen-terminated diamond. Extensive Hall-effect measurements are demonstrated for wide temperature ranges, and a theoretical model is introduced to understand the experimental results. Finally, good transistor transfer characteristics were demonstrated using conventional electrical measurement techniques. The details on the mobility model and the micro-fabrication runsheet are available in Appenices A and B, respectively.

- Chapter 4 demonstrates the electrical performance of the diamond-based devices after being irradiated with 2 MeV protons at two fluences. This was performed on both oxide-passivated and unpassivated samples, in order to decouple the degradation induced in the oxide from the degradation induced in the C-H surface. A classical model is also utilized to gain insight as to how the C-H surface degrades with radiation.

- Chapter 5 contributes to the novel annealing solutions in defective silicon carbide, which can be annealed locally utilizing energetic heavy-ion irradiation. Molecular Dynamics and Ensemble Monte Carlo models are used to demonstrate how, in the presence of high electric fields, this annealing can be enhanced significantly. This also deepens our understanding of irradiated devices with sensitive active regions.

- Chapter 6 concludes this thesis and suggests multiple future directions to progress the work presented in this thesis.

Chapter 2

Background

2.1 Challenges of Doping Diamond

As a semiconductor material, diamond has exceptional figures of merit due to its wide band gap, high breakdown voltage, high thermal conductivity, and high carrier mobility. However, doping of diamond has been a challenge. The doping process aims to generate additional charge carriers by introducing the atoms in a semiconductor with foreign atoms, which are referred to as dopants. These dopants, which have more or less valence electrons than the host material, are ideally substituted in original lattice sites, although incorporating the dopant as an interstitial is also a possibility. In both instances, however, the dopant must become activated. For a donor (n-type dopant), activation implies that the atom's extra valence electron transitions into the material's conduction band. Conversely, in the case of an acceptor (p-type dopant), a vacancy in the atom's valence shells is filled by an electron, thus emitting a hole into the host material's valence band. This activation mechanism also ionizes the dopant, which fulfills the charge neutrality condition. The end result is a host material with a partially occupied conduction band (n-type semiconductor) or valence band (p-type semiconductor), thus facilitating charge mobility and increasing the conductivity.

Unfortunately, the activation process of dopants has been a notorious challenge to researchers. Without activation, the doping process is futile and often results in a defective and electrically unstable material. For silicon, the boron activation energy is 0.045 eV, which is relatively low and allows for feasible fabrication of p-type silicon. In the case of diamond, the boron activation energy is 0.37 eV, which is drastically higher and makes p-type doping of diamond a great challenge. Unfortunately, all other known dopants of diamond exhibit even higher activation

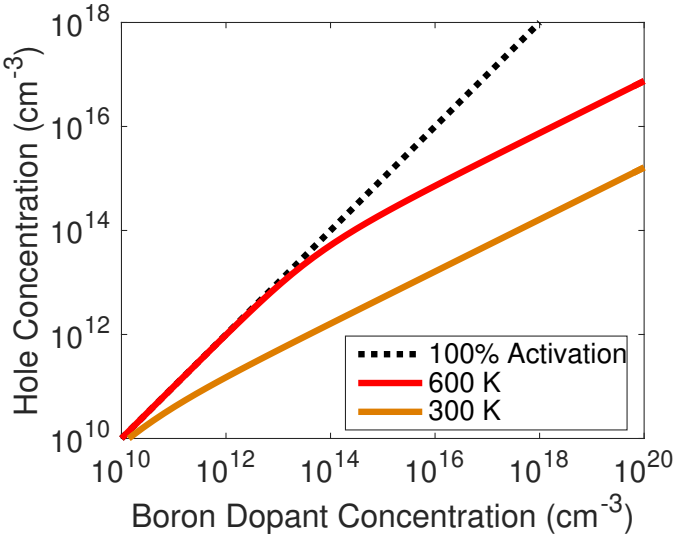

Figure 2.1: Hole concentration vs. Boron dopants. This demonstrates the highly degenerate doping density that is required for reasonable p-type conduction.

energies. For example, the activation energies for phosphorus and nitrogen (both donors) are 0.60 and 1.7 eV, respectively.

The concentration of holes p as a function of boron concentration N_A and activation energy E_A can be expressed as,

$$\frac{p^2}{N_A - p} = \left(\frac{2\pi m^* k_B T}{h^2}\right)^{3/2} \exp\left(-E_A/k_B T\right), \tag{2.1}$$

where m^* is the hole effective mass, k_B is the Boltzmann constant, T is temperature, and h is Planck's constant. Note that for simplicity, Eq. (2.1) neglects a donor concentration. Fig. 2.1 plots this function at 300 and 600 K, presuming $E_A = 0.37$ eV. At room temperature, a degenerate doping level $N_A = 10^{19}$ cm^{-3} results in $p \approx 10^{19}$ cm^{-3}. In other words, about one in 10^4 boron acceptors are activated at room temperature. Thus, highly degenerate concentrations of boron acceptors are required to induce acceptable conductivity values. Effective doping processes are currently being investigated by researchers. Among these are co-dopants, where the incorporation of a compound (as opposed to an element) acts as a dopant. Doping with boron and sulfur, for instance, has been shown to produce n-type diamond [20]. The reliable control of diamond's conductivity remains a challenge, however, but it is key to unlocking its potential as a semiconductor material for device applications.

2.2 Two-Dimensional p-type Conduction on H:diamond Surfaces

Processing concerns over dopant activation is not unusual in the semiconductor industry. Dopant activation of wide band-gap semiconductors are a great challenge, such as in p-type doping in gallium nitride [21] and silicon carbide [22]. A variety of heterostructures exist where a dense concentration of 2D electron gas (2DEG) is formed along the interface, such as in AlGaAs/GaAs, AlGaN/GaN, and $SrTiO_3/LaAlO_3$. For applications requiring n-type conduction only, the need for doping can be circumvented using these heterostructure technologies with high-mobility 2DEGs [23]. Similarly, p-type conduction on diamond can be realized without doping since a 2D hole gas (2DHG) can be generated on its surface. To understand how 2DHGs are formed, we briefly discuss the physics of the hydrogen and oxygen-terminated diamond surface, and how they can be exploited to form well-defined planar devices.

2.2.1 Surface Termination

For all crystals, a disruption in the lattice periodicity results in the rearrangement of the local atomic structure. Vacancies and interstitials, for example, may contract or expand the lattice positions in their immediate vicinity as a means of minimizing the energy. The surfaces of these crystals behave similarly, in that the disruption of the lattice periodicity and the resulting dangling bonds induce a rearrangement of the atomic structure that is unlike the atomic lattice positions in the bulk. In the (100) surface of diamond, carbon atoms undergo a 2×1 reconstruction in the form of π-bonded dimers. If the surface is exposed to elemental hydrogen, such as in a hydrogen plasma, these C-C dimers can be converted to a single bond with one H-atom attached to each carbon. This termination neutralizes dangling bonds and surface states [24]. Similarly, an oxygen plasma creates C-O bonds at the surface. The former is referred to as a hydrogen-terminated diamond surface, whereas the latter is oxygen-terminated. In this thesis, we refer to these as H:diamond and O:diamond, respectively.

The reconstruction of the surface, as well as the surface termination, has physical implications that open the door to a variety of applications. Most importantly, the electron affinity depends drastically on the surface termination, and is defined as the energy difference between the conduction band minimum E_{CBM} and the vacuum level E_{VAC}, given by

$$\chi = E_{\mathrm{VAC}} - E_{\mathrm{CBM}}. \tag{2.2}$$

A clean reconstructed surface with no termination possesses a χ value of around 0.4 eV, which is fairly low for most semiconductors [25]. This value can be further increased with oxygen termination, where χ increases to around 1.7 eV [26]. This is caused by the higher electronegativity of oxygen relative to carbon, which results in a negative charge δ^- on the O atom and a positive charge δ^+ on the neighboring carbon atom. For H:diamond surfaces, the opposite phenomenon occurs. In this configuration, the polarization of the C-H bond is due to hydrogen having a lower electronegativity than carbon, resulting in δ^+ on the H atom and δ^- on the neighboring C atom. This polarization induces a steep potential drop perpendicular to the surface over a distance equal to the C-H bond length, as shown in Fig. 2.2. The result is a negative electron affinity (NEA) $\chi \approx -1.3$ eV, which means that electron emission into the vacuum requires less energy than a transition from the valence band to the conduction band. A NEA is a highly unusual phenomenon, but with attractive applications. For one, efficient photoemitters and cold cathode field emitters can be developed using H:diamond [27]. However, as is the subject of this work, H:diamond can be exploited to provide a high p-type surface conductivity for electronic device applications. This is made possible via a charge transfer process between the VBM of the diamond surface and lower energy states provided by atmospheric molecules or oxide films, a mechanism denoted as surface transfer doping.

2.2.2 Surface Transfer Doping

Surface transfer doping of diamond surfaces has garnered much attention, as it circumvents the great challenges posed by the conventional substitution of the donor/acceptor atoms in the tight diamond lattice. This transfer mechanism is facilitated by the NEA of hydrogen-terminated diamond, where the VBM is energy level is high with respect to the vacuum energy level, which in turn is higher than the lowest unoccupied molecular orbitals (LUMOs) of many atmospheric molecules. Thus, these LUMO act as accessible acceptor levels, which become ionized (or filled) by the electron transfer from the VBM of diamond. The result is, thus, a depleted hole quantum well (i.e., a 2DHG) and a compensating sheet of negative charge by the acceptors. An example of these acceptors are contained in the mildly acidic water in our atmosphere. Chemically, the electron exchange from the VBM of H:diamond to the adsorbed water layer is governed by the redox reaction $2H_3O^+ + 2e^- \rightleftharpoons H_2 + 2H_2O$ [28]. The space charge produced in the adsorbates compensates the hole accumulation layer until equilibrium is reached between the Fermi level and the chemical potential of the H:diamond and water layer, respectively. An alternative formation of the 2DHG is via oxide passivation films. If the electron affinity of the oxide film is sufficiently large, its CBM may lie below the VBM of the H:diamond, thus providing

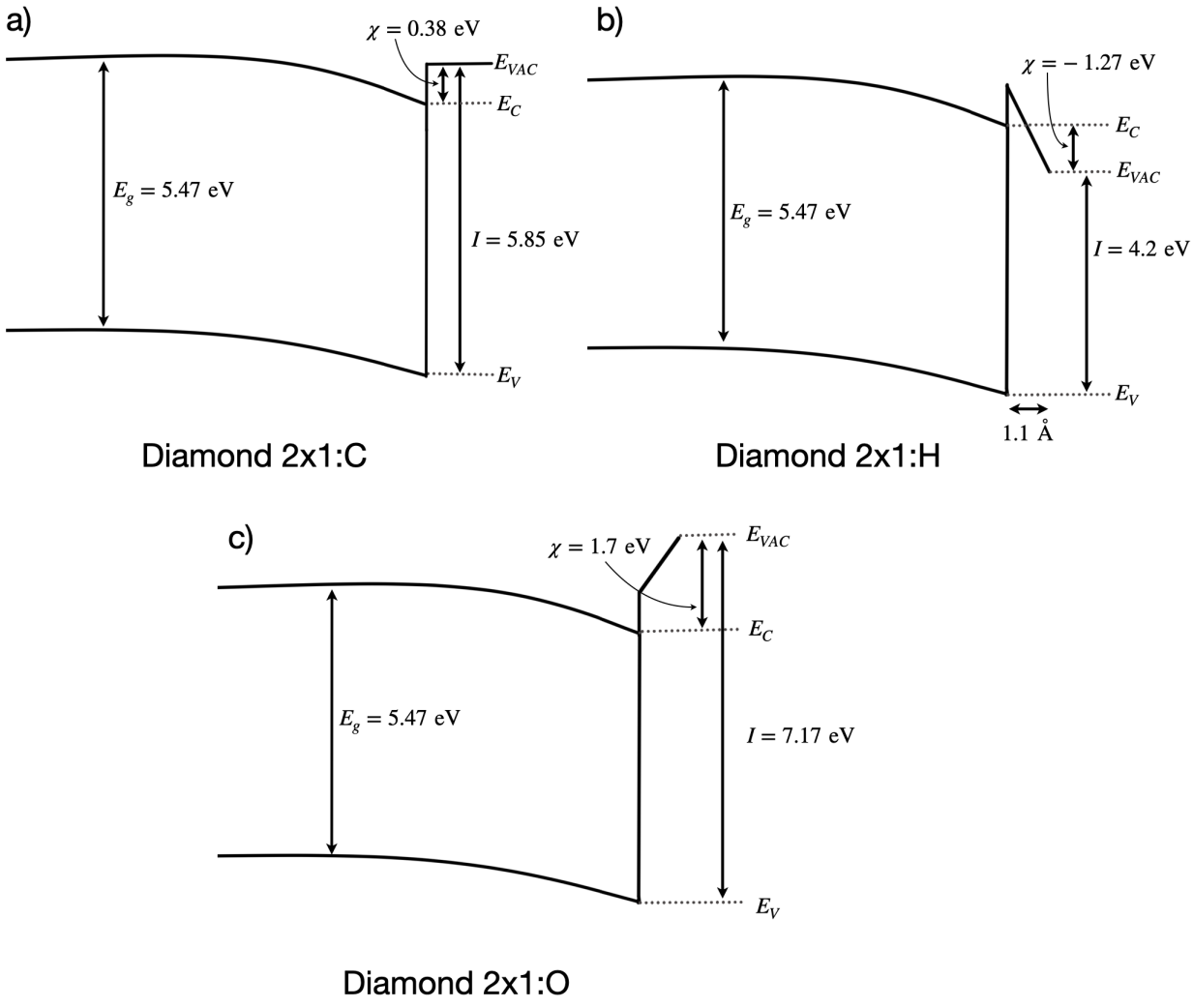

Figure 2.2: Band diagram of a diamond surface for various terminations. a) Clean (2×1) reconstructed surface with a positive electron affinity, b) Hydrogen-terminated surface with a negative electron affinity (NEA). The NEA of the H:diamond surface is induced by the C-H dipole, which produces a steep potential step over the C-H bond length of 1.1 Å, and c) Oxygen-terminated surface with the highest electron affinity.

a large density of available states for electron transfer and 2DHG formation. Transition metal oxides such as WO_3 and V_2O_5 are two examples that have been shown to induce especially high 2DHG densities. Finally, the 2DHG can be formed by energy states provided by oxide defects. For example, defects in Al_2O_3 are believed to produce available states well below the VBM of H:diamond [29, 30]. Thus, despite the ultra-wide band gap of ∼7 eV, a 2DHG has been observed for Al_2O_3-passivated H:diamond. As will be discussed later in this work, Al_2O_3 is especially stable at a wide range of temperatures, which can resolve the notoriously unstable electrical properties observed in air-adsorbed H:diamond [31].

2.2.3 Operational Issues of Air-adsorbed H:diamond

Upon hydrogen-terminating a clean diamond surface, an immediate source of acceptors is provided by the atmosphere. As discussed previously, this is believed to be governed by a redox reaction with an adsorbed water layer, resulting in an electron exchange and a 2DHG formation. Additionally, exposure to different gases, such as O_3, NO_2, and NO, contributes to a varying density of these acceptors, which therefore modulate the 2DHG concentration [32]. Exposure to HCl, H_2SO_4, and HNO_3 also exhibits an increase in the 2DHG density, as reported in [33]. Unfortunately, despite the achievable conductivity, air-doped H:diamond is notorious for being thermally unstable and difficult to reproduce. As shown in Fig. 2.3, the hole sheet density degrades rapidly at higher temperatures for air-doped diamond. Since the air acceptors are bounded weakly via van der Waals forces on the diamond surface, they desorb quickly with temperature, thus making air-doped diamond unsuitable for device applications.

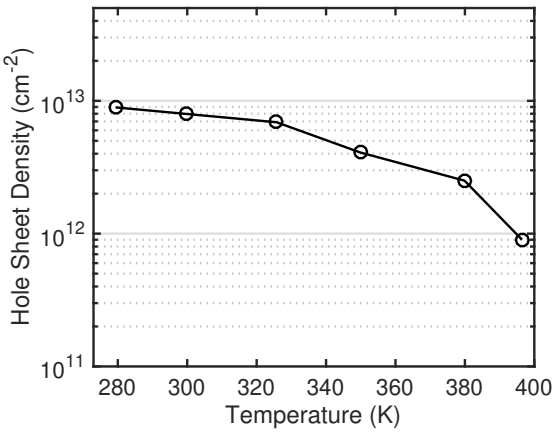

Figure 2.3: Air-doped sheet density as function of temperature. Since the sheet density drops rapidly with temperature, air-doped diamond is unsuitable for high temperature operation.

2.2.4 Robust Performance via Oxide-Passivation

Fortunately, oxide passivation has been shown to stabilize the conductivity while providing a respectable (and in some cases, superior) density of acceptors. For example, H:diamond surfaces passivated with Al_2O_3 stabilizes the 2DHG density at temperatures up to 700 K [31, 34]. For this reason, oxide passivation for H:diamond surfaces are regarded as the key to robust device performance. Multiple oxides have been explored as potential passivation films, including Al_2O_3, HfO_2, and SiO_2. Moreover, transition metal oxides (TMOs) have exhibited especially high sheet densities. Examples include WO_3, Nb_2O_5, MoO_3, and V_2O_5 [31], all of which boost the sheet density to values well over $1{\times}10^{13}$ cm^{-2}. This boost is owed to the high electron affinity of these TMOs, which place the CBM energy below the VBM of the H:diamond surface. Thus, we would expect the sheet density to correlate with the electron affinity magnitude of the TMO, which is precisely what was observed in Ref. [31].

2.3 Studying the Hole Transport Properties of H:diamond

In this section, an experimental and theoretical method of determining the hole mobility is discussed. This lays the groundwork for Chapter 3, where the theoretical model is used to fit to the experimental data, which is key to providing insight into the various scattering mechanisms that are degrading the mobility.

2.3.1 Experimental: The Hall-effect Method

The Hall-effect method is widely used in probing the electrical properties of materials. The fundamental idea of this method is to exploit the Lorentz force on a single charge carrier, given by,

$$\mathbf{F} = e\left(\mathbf{E} + \mathbf{v} \times \mathbf{B}\right), \tag{2.3}$$

where e is the elementary charge, moving with a velocity $\mathbf{v}$ in the presence of an electric field $\mathbf{E}$ and a magnetic field $\mathbf{B}$. Should this current injection occur along a conductive square plane with point-like electrodes on the corners, we can readily measure the voltage that is induced as a result of this force (as depicted in Fig. 2.4), defined by

$$V_{\text{Hall}} = \vec{\nu}_x \vec{B}_z w, \tag{2.4}$$

where w is the width of the conductive region. We also note that the injected current can be defined as $\text{I}_{\text{supply}} = ep_{2d}w\vec{\nu}_x$, where p_{2d} is the hole sheet density. By solving for w and substituting into Eq. (2.4), we can relate p_{2d} with our known variables, as expressed by,

$$V_{\text{Hall}} = \frac{I_{\text{supply}} B_z}{p_{2d} e}. \tag{2.5}$$

Furthermore, the sheet resistance can also be extracted by applying a current between two adjacent electrodes, and measuring the induced voltage across the opposite pair of electrodes. This technique is known as the van der Pauw method. We can enumerate the electrodes from 1 to 4 (in a counter-clockwise order, starting at the top-left electrode, as depicted in Fig. 2.4), and define the following resistance parameter,

$$R_{12,34} = \frac{V_{34}}{I_{12}}. \tag{2.6}$$

The values for $R_{34,12}$, $R_{21,43}$, and $R_{43,21}$ can similarly be calculated, each of which involves applying the current in the vertical direction (across contacts 1↔2 and 3↔4). Averaging these

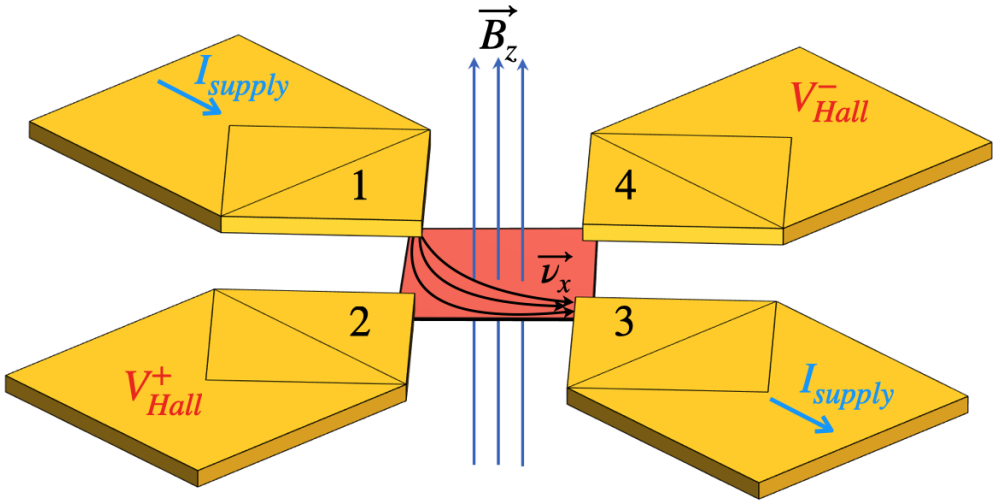

Figure 2.4: Operation of a Hall-effect device and extraction of V_{Hall}.

values yields an average vertical resistance R_{vertical}. We can perform this set of measurements for the horizontal direction (i.e., current along 1↔4 and 2↔3), and finally use the van der Pauw formula, given by,

$$\exp\left(-\pi R_{\text{vertical}}/R_{\text{S}}\right) + \exp\left(-\pi R_{\text{horizontal}}/R_{\text{S}}\right) = 1, \tag{2.7}$$

where R_{S} is the sheet resistance, commonly expressed in units Ω/sq. This can be related to the hole mobility by the expression,

$$\mu_H = \frac{1}{ep_{2d}R_{\text{S}}}. \tag{2.8}$$

Thus, the Hall-effect and the van der Pauw techniques provide the core electrical properties of the active regions in our devices. Moreover, by extracting these properties at multiple points along a wide temperature range (e.g., 50 to 700 K), valuable insight can be inferred on the material properties of the conducting channel, as will be demonstrated in later sections.

2.3.2 Theoretical: Hole Relaxation Time Calculations

In this section, a formulation for the hole relaxation time is presented, from which the theoretical hole mobility is calculated. For 2DHGs in H:diamond, the hole mobility is only limited by phonons at high temperatures. In the low-to-intermediate regime, however, the mobility is theorized to be mostly limited by the Coulombic interactions between the 2DHG and localized fields in-plane, such as those induced by ionized surface acceptors. The relaxation times associated with four hole scattering mechanisms are introduced in Appendix A. This model also uses the hole Fermi energy values and probability density functions for the heavy hole, light hole, and split-off valence bands. This multi-band treatment was performed using a Poisson/Schrödinger solver, the details of which are discussed in Appendix A.

In this model, the 2D holes are characterized by a plane wave along the diamond surface (**r**-plane), and a quantized wave perpendicular to the surface (z-axis). Thus, the incident and final states, expressed as plane waves, are written as $\Psi_i = A^{-1/2}\psi(z)\exp(i\mathbf{k}\cdot\mathbf{r})$ and $\Psi_f = A^{-1/2}\psi(z)\exp(i\mathbf{k'}\cdot\mathbf{r})$, where $\mathbf{k}$ and $\mathbf{k'}$ are the initial and final hole wave vectors, respectively, and $\psi(z)$ is the out-of-plane wave function determined using the Schrödinger/Poisson solver. The factor A is the 2D normalization constant converting the scattering rate per unit

area (also denoted by L^2). The two-dimensional form of scattering rate is expressed by integrating over all possible final states $\mathbf{k}'$ of the scattering matrix $M_i(\mathbf{k}, \mathbf{k})$,

$$\Gamma^i_{\mathbf{k}',\mathbf{k}} = \frac{2\pi}{\hbar}\frac{L^2}{(2\pi)^2}\int d^2\mathbf{k}'|M_i(\mathbf{k}', \mathbf{k})|^2\delta[\mathcal{E}_{\mathbf{k}'} - \mathcal{E}_{\mathbf{k}}], \tag{2.9}$$

where i denotes the scattering mechanism, and the delta function ensures the conservation of energy. The mobility is determined by the transport lifetime (or relaxation time) τ_{rt}, which is a function of the net scattering rates $\Gamma^i_{\mathbf{k}',\mathbf{k}}$ and also a function of the scattering angle between vectors $\mathbf{k}$ and $\mathbf{k}'$, denoted by θ. Via Boltzmann transport equation and the principle of detailed balance, the angle dependence is introduced by the factor $(1-\cos(\theta))$. We can write the relaxation rate in terms of the displacement vector $\mathbf{q} = \mathbf{k}' - \mathbf{k}$,

$$\frac{1}{\tau_i(k)} = \frac{2\pi}{\hbar}\frac{L^2}{(2\pi)^2}\int d^2\mathbf{q}|M_i(\mathbf{q})|^2(1 - \cos(\theta))\delta[\mathcal{E}_{\mathrm{k}'} - \mathcal{E}_{\mathrm{k}}]. \tag{2.10}$$

Presuming each scattering mechanism i is independent, the total relaxation time τ_{tr} is given by

$$\frac{1}{\tau_{tr}(k)} = \sum_i \frac{1}{\tau_i(k)}. \tag{2.11}$$

These relaxation times are numerically calculated and averaged according to the Fermi statistics,

$$\langle\tau_{tr}\rangle_j = \sum_{\mathrm{k}} \mathcal{E}_{\mathrm{k}}\tau^j_{tr}(k)\left(\frac{\partial f(\mathcal{E}_{\mathrm{k}})_j}{\partial\mathcal{E}_{\mathrm{k}}}\right)\Bigg/\sum_{\mathrm{k}}\mathcal{E}_{\mathrm{k}}\left(\frac{\partial f(\mathcal{E}_{\mathrm{k}})_j}{\partial\mathcal{E}_{\mathrm{k}}}\right). \tag{2.12}$$

Here the subscript j was introduced to signify that the relaxation times are unique to each band j, each of which has an effective mass m^*_j, carrier density ρ^j_{2D}, and Fermi energy from Eq. (A.1). The averaged relaxation time is used to deduce the hole mobility, obtained using the widely used relation,

$$\mu_j = \frac{e}{m^*_j}\langle\tau_{tr}\rangle_j. \tag{2.13}$$

Finally, the total mobility can be determined by weight-averaging each band, given by

$$\mu_H = \frac{\sum_j \mu_j \rho_{2D}^j}{\sum_j \rho_{2D}^j}. \tag{2.14}$$

The final result in Eq. (2.14) links this theoretical framework with the measured quantity obtained via Hall-effect measurements (Eq. (2.8)). The scattering mechanisms modeled by the matrix elements in Eq. (2.10), as well as the relaxation averaging of Eq. (2.12), result in μ_H that is a function of temperature, sheet carrier density, impurity density, and other material properties. This modeling framework will thus provide us with a thorough understanding of the limitations to the hole conductivity of 2D hole gases in H:diamond.

2.3.3 Mobility Ceiling

One of the greatest milestones for diamond as an emerging device platform is to maximize the drive current. Among various properties that must be optimized, the hole mobility is most critical, as it is significantly lower than theoretical values. This is shown in Fig. 2.5, which includes hole mobility data points of H:diamond from multiple references [31, 34–39]. While the sheet density has been measured to span over two orders of magnitude (even exceeding 10^{14} cm^{-2}), both for passivated and unpassivated surfaces, the mobility spans a much narrower range, most typically below 100 cm^2/(V·s). The virtual "mobility ceiling" that is produced presents a unique challenge to realize highly conductive H:diamond for device applications.

To see this, we can invoke the scattering rate by surface impurity scattering in Eq. (A.6), which is $\propto N_{si} \cdot \exp(-q(z + |d|))$, where d is the average distance between the 2DHG and the compensating sheet of negatively charged acceptors (N_{si}), and q is the scattering wavevector. This proximity results in strong Coulomb interactions which degrades the hole mobility significantly. Design solutions aiming to increase d (as accomplished with "spacer layers" in III-V heterostructures, for example) may provide an avenue to break through the mobility ceiling and thus decrease the sheet resistivity to acceptable values.

Moreover, as we will discuss in depth in the next chapter, the hole mobility remains low even as N_{si} decreases. If surface impurity scattering via the 2DHG and the compensating negative sheet charge is the dominant scattering mechanism, then per Eq. (A.6), the scattering rate should decrease accordingly at low sheet densities. However, this is not what we see in Fig. 2.5. Thus, the implication here is that an additional scattering mechanism exists, which lays ground to yet another avenue to maximize the hole conductivity.

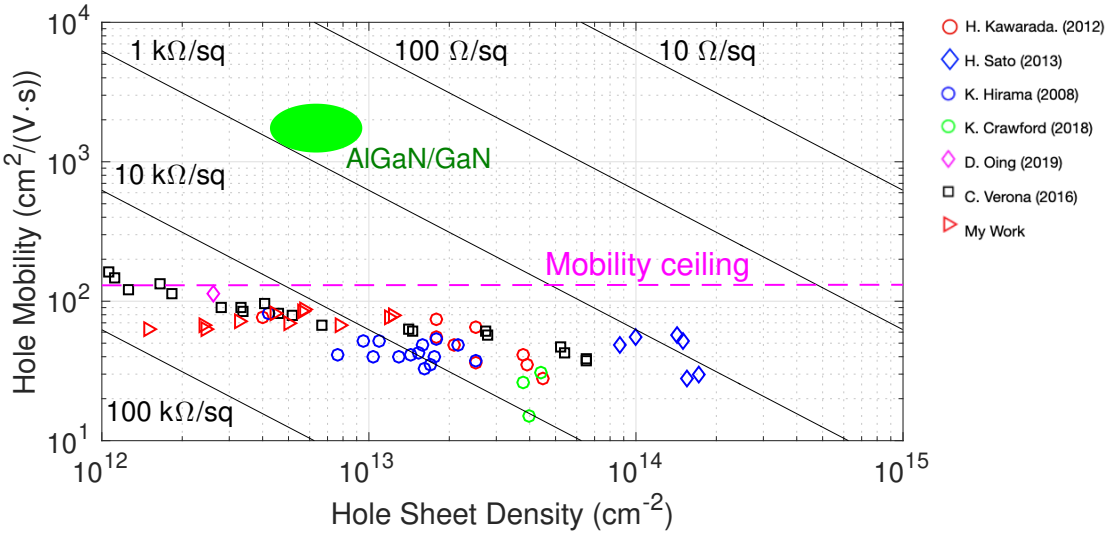

Figure 2.5: Mobility ceiling of 2DHG for various passivated and unpassivated H:diamond structures. While the sheet density has been demonstrated to span over two orders of magnitude, the mobility spans a much narrower range [31, 34–39].

2.4 Ionizing Radiation Effects in Semiconductors

2.4.1 Particle interaction with matter

The terms "harsh" or "extreme" environments often allude to high temperatures. However, environments that are rich in radiation also fit into this category. Particle radiation such as protons, electrons, and alpha particles, for example, are highly invasive as they penetrate sensitive regions in electronics and disrupt their operation – sometimes permanently. Unfortunately, these species of radiation are abundant in space environments, especially during solar particle events, as shown in Fig. 2.6(a) for protons.

Whenever a radiation species penetrates a material, it slows down as it deposits its kinetic energy via ionization and via nuclear interactions. While the former energy deposition is manifested as the emission of electron-hole pairs, the latter induces atomic displacements in the material. These mechanisms of energy loss are commonly referred to as electronic and nuclear stopping power (SP). The proportion of these two mechanisms depend on the particle mass, charge, kinetic energy, as well as the properties of the target material. An instance of this nuclear and electronic SP proportion can be calculated using open source simulators, as shown in Fig. 2.6(b).

For light and energetic particles, electronic SP (i.e., ionizing radiation) is the most common mechanism of energy loss. Since such particles are difficult to absorb, they often pierce through

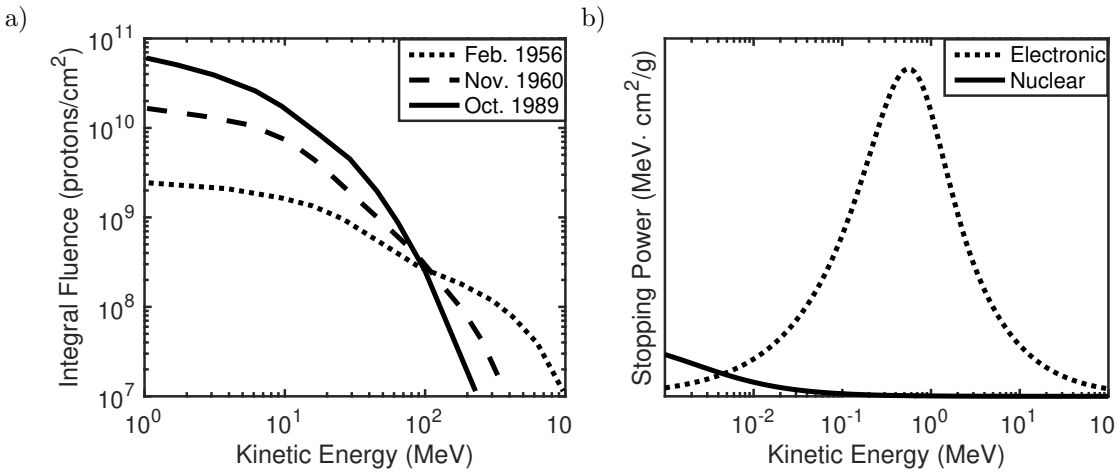

Figure 2.6: (a) Integral fluences of protons during the months of solar particle events, where large quantities of particles radiate into the solar system [40].(b) Nuclear and electronic stopping power of an alpha particle in a hydrogen-rich environment. With the exception of very low kinetic energies, electronic stopping power dominates the energy loss mechanism [41].

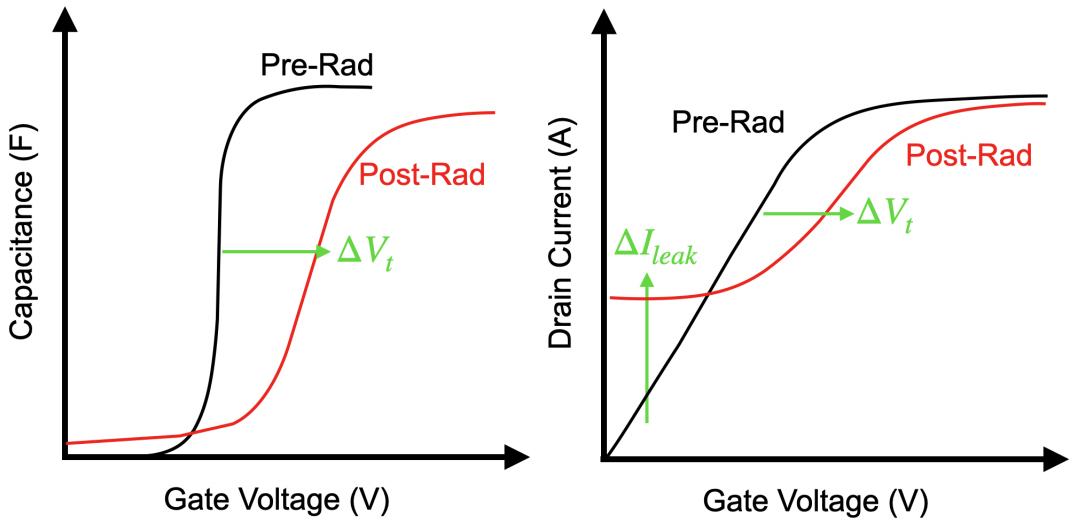

Figure 2.7: TID effects on microelectronic devices, such as a threshold voltage shift and increase in leakage current. These are instances of degradation that become apparent after large doses of radiation.

microelectronic devices and materials, leaving a cylindrical-shaped volume of energetic electron-hole pairs in its track. As a consequence, the key performance metrics of these devices tend to degrade.

2.4.2 Total Ionizing Dose (TID)

In order to make predictions on the robust operation of microelectronic devices in radiation environments, it is useful to quantify the absorbed dose over time. This is commonly referred to as total ionizing dose, or TID, and it is among the most significant failure mechanisms of irradiated devices. The main vulnerability of TID are the oxides, which are intrinsic to many device structures that require insulating layers, such as in metal-oxide-semiconductor and silicon-on-insulator structures. Among many of the key device metrics that degrade are the current leakage, ON resistance, and threshold voltage shifts, as shown schematically in Fig. 2.7. TID effects are most typically induced by energetic ions with low mass, such as protons and electrons in the MeV-range. Thus, space environments [Fig. 2.6(a)] can be regarded as hostile to devices, particularly those with structures involving oxides. To protect against TID degradation, shielding and quality assurance of the on-board electronics may be necessary. Additional solutions include novel device designs and materials that are intrinsically radiation-hardened.

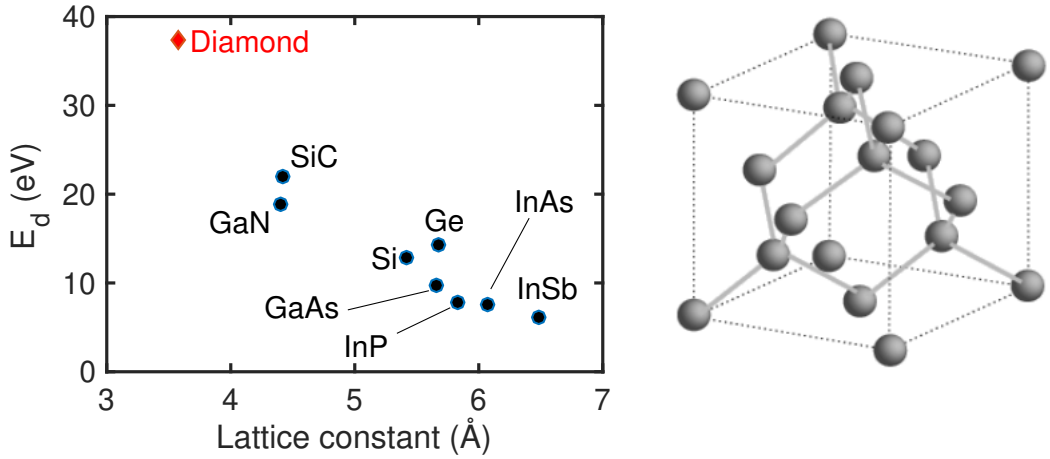

Figure 2.8: Threshold displacement energies of various semiconductors. Due to the tight lattice spacing of diamond (crystal structure shown on the right), more energy is required to fully displace a carbon atom [42–44].

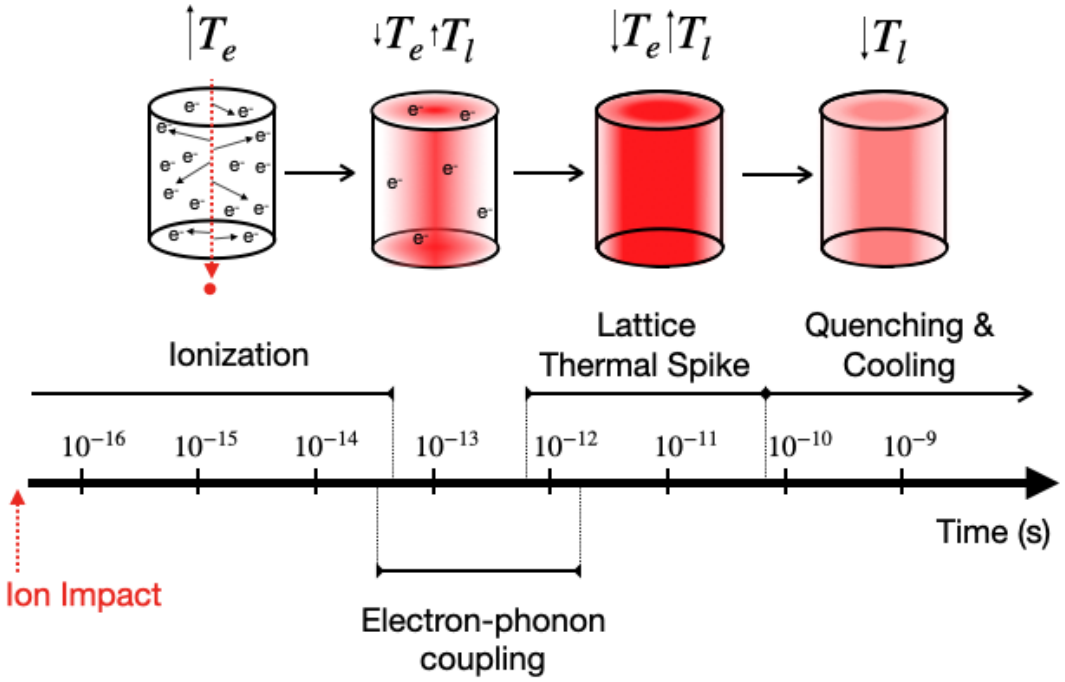

Figure 2.9: Schematic of a thermal spike event as induced by highly energetic ions.

2.4.3 Other Radiation Effects

Nuclear stopping power, which involves energy loss in elastic collisions between the nuclei of the target material and the radiation species, is responsible for atomic displacements that can also alter the structural and electronic properties. Nuclear SP is most prominent the heavier the particle. For charged radiation species, these collisions are driven by repulsive Coloumbic interactions. If the collision imparts energy greater than a certain value, known as the threshold displacement energy E_d, then the target atom (also known as a primary knock-on atom) will be displaced and potentially act as a radiation species of its own – creating a cascade effect with the surrounding atoms. Below E_d, and the target atom is merely perturbed and returns to its original site. Such events can be responsible for producing significant lattice damage, potentially leaving the once-crystalline material amorphous if the dose is large enough. Figure 2.8 shows the threshold displacement energies for various semiconductor materials [42–44]. Due to the tight lattice spacing of diamond, the carbon atoms are highly bound and more energy is required to permanently displace them.

Although heavy particles can induce significant lattice damage via elastic collisions, the profiles shown in Fig. 2.6(b) still hold true. That is, heavy particles penetrating materials at sufficiently high velocities dissipate energy primarily in the form of electronic SP. Such species are

commonly referred to as swift heavy ions (SHIs). SHI species are unique in that they unleash significant quantities of ionization energy, which, via electron-phonon coupling, sequentially raises the lattice temperature to thousands of degrees. Thus, the cylindrical volume that encloses the penetrating SHI (tens of nanometers in diameter) melts the lattice and rapidly freezes as its energy is radially dissipated, all in picosecond-to-nanosecond time scales. This is shown schematically in Fig. 2.9. The effects of this rapid heating and cooling as induced by penetrating ions in materials is largely unexplored. For one, it may render the lattice locally amorphous. However, in some instances, as will be discussed in Chapter 5, such events can annihilate pre-existing defects, thus providing a localized annealing solution that does not require a macroscopic and prolonged heating of the entire substrate. This has significant implications in the realm of ion implantation, ion-beam analytic techniques, neutron irradiation, and the operation of devices in radiation-rich environments. For example, an accurate reliability analysis of such materials in radiation environments hinges on the understanding of how their crystal structure evolves over time. Additionally, calculations of ion implantation profiles may prove to be inaccurate unless this annealing effect is accounted for.

2.5 Chapter Summary

In this chapter we discussed the difficulties of doping and the promise behind hydrogen-terminated diamond surface. By exploiting the negative electron affinity of H:diamond, and the highly positive electron affinity of O:diamond, we can form conductive and insulating regions, thus defining planar devices. We also overviewed the hole transport properties, including a theoretical formulation of the mobility which was used to fit to the experimental Hall-effect measurements. This is accomplished by calculating the relaxation times associated with four hole scattering mechanisms, as formulated in Apprendix A. We also observed how a "ceiling" to the hole mobility is observed throughout literature, where values below 100 $cm^2/(V\text{-}s)$ are measured even at low sheet densities. Thus, we hypothesize that an additional scattering mechanism contributes significantly to the low hole mobility. Finally, we discussed the effects of irradiation in semiconductors, including the TID effects, atomic displacement events, and thermal-spikes induced by highly energetic ions. For the latter, the rapid heating and cooling induced by energetic ions and its effect on materials is largely unexplored. It has been shown, for example, that such events can annihilate pre-existing defects, thus providing localized and low-temperature annealing solutions.

Chapter 3

Fabrication and Characterization of H:diamond Devices

3.1 Fabrication of H:diamond Devices

In this section, we will overview the nature of the conductive and insulating diamond surface, including an outline of the H:diamond fabrication process. The content of this chapter can be found in our published work [39].

3.1.1 Hydrogen and Oxygen Termination of Diamond Surfaces

As discussed in section 2.2, the dipole carbon-hydrogen (C-H) bonds in H:diamond form a steep potential that lowers the vacuum energy level below the conduction band minimum of diamond. As a result, any energy state (i.e., acceptor) below the valence band maximum of H:diamond is accessible for charge transfer. In fact, high work-function oxides (e.g., WO_3, MoO_3, and V_2O_5), have conduction band minima below the diamond's valence band maximum, which introduces a continuum of states and thus a hole sheet density as high as $1{\times}10^{14}$ cm^{-2} [35].

In this process, the H-termination was formed by exposing the diamond samples to a high kW-power plasma in a MPCVD chamber at the University of California, Davis (Fig. 3.1(a)). No substrate heater was used. Instead, the surface temperature was controlled by the plasma power and chamber pressure, and was constantly measured remotely using a pyrometer. The exposure times to the hydrogen plasma ranged from 15 to 30 min. For the formation of insulating regions, a standard lithography process was used to expose the isolation regions of the surface and treat with an oxygen plasma, generated using a standard plasma cleaning tool at 100 W (Fig. 3.1(a))

a) b)

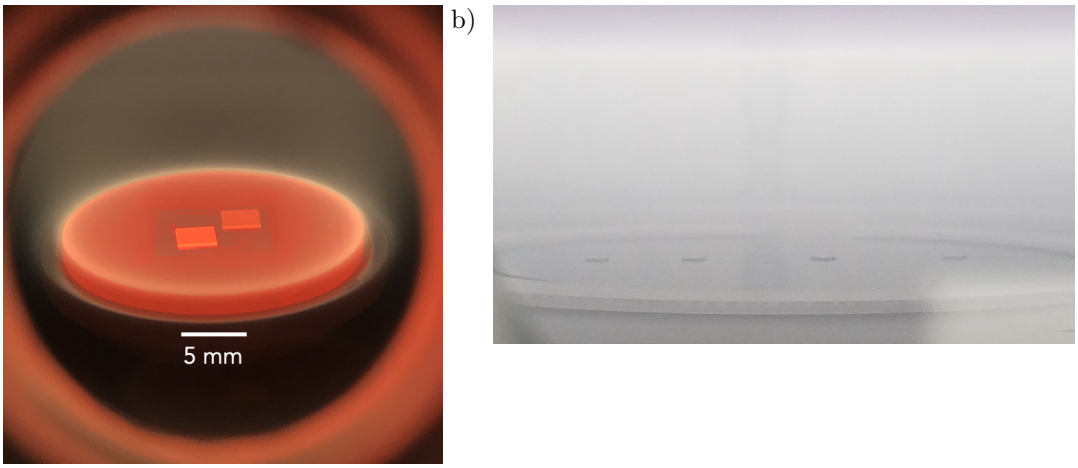

Figure 3.1: (a) Hydrogen-terminating the surface of single-crystal diamond in the microwave-plasma CVD chamber. (b) Oxygen-terminating the isolation regions in an oxygen plasma (using a standard plasma cleaning system).

for 90 seconds. The fabrication process is outlined step-by-step in a later section.

In this work, the 2DHG exhibited a wide range of concentration ($\sim 2\times10^{12} - 1.5\times10^{13}$ cm^{-2}) and mobility ($\sim 30 - 100$ cm^2/(V-s)) values from sample to sample. This, in part, inspired the content of this work, since patterns began to emerge and previous mobility models were inconsistent with experiment. Prior to this realization, however, other processing steps needed to be developed at Stanford's Nanofabrication Facility (SNF), such as metal contacts and passivation layers. This will be the subject of the following sections.

3.1.2 Metal Contacts on H:diamond Surfaces

Ohmic and Schottky Contacts

Metal contacts can exhibit both ohmic and Schottky behavior on H:diamond surfaces. In effect, hydrogen-termination neutralizes the diamond surface states, which results in a linear dependence between the Schottky barrier height (SBH) and the electronegativity [24]. This was first described by Mönch in relating the metal-induced gap states (MIGS) and electronegativity in metal-semiconductor contacts [45]. Thus, since H:diamond conduction is p-type, metals with a high electronegativity, such as Au and Pt, exhibit ohmic behavior and low contact resistance. On the other hand, low electronegativity metals such as Mg, Al, and Ti, exhibit rectifying behavior. This dependence between SBH and electronegativity on H:diamond has been demonstrated by Kawarada *et. al.* for a variety of metals [46]. As will be discussed in a later section, the formation of both ohmic and Schottky contact allows us to realize metal-semiconductor field-effect

transistors (FETs).

Adhesion Issues

In a pristine surface of (100) diamond, the carbon atoms are reconstructed such that the four outermost valence orbitals are bonded, thus forming C-C dimers. The effect of the hydrogen termination process is to break these dimers and form a dipole with each surface carbon atom. Moreover, given the small size of the hydrogen atom, the C-H bond length is very small (1.1 Å), which results in a great force of attraction between the nuclei and forms a highly stable bond. However, this is an unfortunate reality in the context of metal electrodes, whether they be Schottky or ohmic. When evaporated, a metal contact is inert to the C-H surface. This results in a relatively large distance between the metal atoms and the C-H surface, where even mild external forces can be sufficient to physically lift the metal layer. Fig. 3.2 (top) shows that after spraying the surface with solvents, the Ti/Pt/Au layer was lifted.

Poor adhesion makes probing and wirebonding either very difficult or practically impossible, which makes the electrical measurement process challenging. Unfortunately, the rest of the refractory metals (e.g., Mo, W, Cr, and Ta) that are common in metal contact stacks are highly non-adhesive on H:diamond surfaces, according to *ab initio* studies [47, 48]. Fortunately, as demonstrated in this same study, O:diamond adheres very well to such metals. Thus, by oxygen-terminating the diamond surface via an oxygen plasma, adhesion is achieved. Although this added another lithography step in our fabrication process, wirebonding and probing on the contacts became trivial. As shown in Fig. 3.2 (bottom), the outer perimeter was treated with oxygen-plasma prior to metal deposition. The resulting adhesion was strong enough for wirebonding.

3.1.3 Al_2O_3 Passivation via Atomic Layer Deposition

As shown in Fig. 3.3, H:diamond surfaces passivated with Al_2O_3 stabilizes the 2DHG density at temperatures exceeding 650 K. Thus, for our metal-insulator-semiconductor (MIS) process, we deposit 25 nm of Al_2O_3 at 250°C. It is worthwhile noting that higher temperature depositions of Al_2O_3 have exhibited greater stability at high temperatures. Diacho *et. al.* showed, for example, that ALD-Al_2O_3 deposited below 400°C produces bubble-like patterns after annealing at 550°C in air [49]. On the other hand, Ren *et. al.* showed that higher temperature depositions produce lower sheet densities, presumably owing to the higher quality oxide (and thus lower acceptor state density) [50]. Thus, part of the design process for ALD-Al_2O_3 deposition is to strike a balance between thermal integrity and electrical performance.

Although the surface transfer mechanism into high-WF oxides is clear (since the CBM of

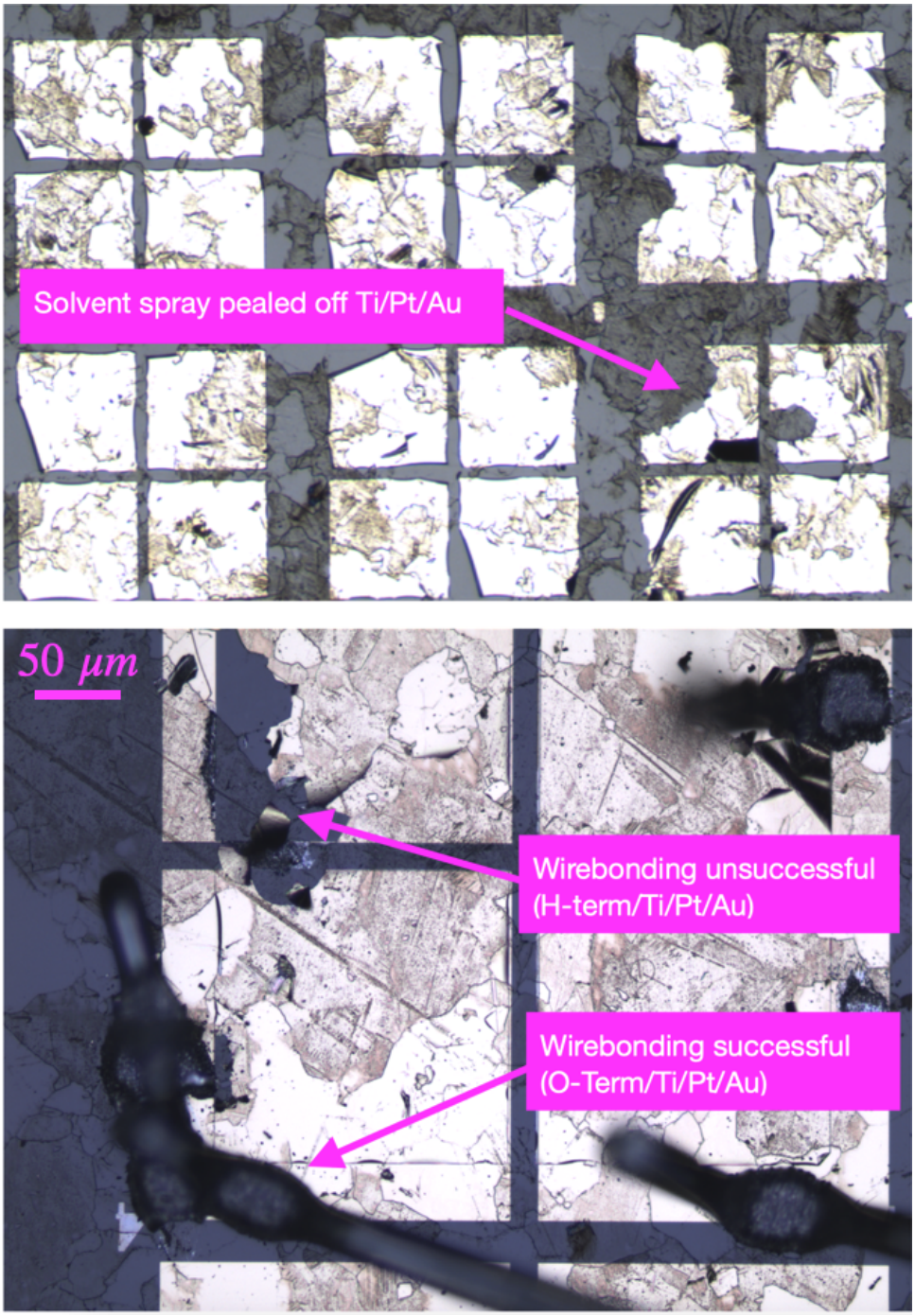

Figure 3.2: (Top) Ti/Pt/Au layer on hydrogen-terminated diamond (polycrystalline in this case, which explains the apparent grain boundaries). The result of spraying with solvents was sufficient to peal off the metal layers. (Bottom) Another Ti/Pt/ Au layer was deposited, this time with oxygen-plasma exposure prior to evaporation+lift-off. The result was strong adhesion, thus allowing for wirebonding.

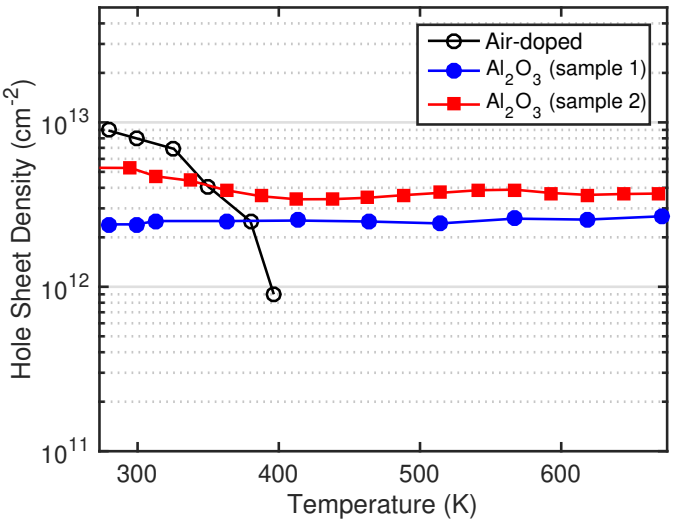

Figure 3.3: Sheet density of air-doped and Al_2O_3-passivated H:diamond at high temperatures. The sheet density of air-doped diamond drops precipitously due to the desorption of weakly-bounded air dopants. In contrast, Al_2O_3-passivated H:diamond exhibits high stability, as shown here for two separate samples. The ALD temperature was 250°C for both samples.

the oxide is below the VBM of the H:diamond), the mechanism behind the surface transfer into Al_2O_3 is less certain. For one, the bandgap of Al_2O_3 exceeds 6 eV, and its CBM is well above the diamond's VBM. For this reason, it is speculated that the 2DHG is a consequence of electron transfer into unoccupied energy states in the Al_2O_3, arising from its vacancies and interstitials [51]. Oxygen interstitials (O_i) and aluminum vacancies (Al_v) are two such species that may be responsible for these unoccupied states. Since the O_i and Al_v energy levels are near the VBM of Al_2O_3, this implies that charge transfer from the VBM of H:diamond is energetically favorable, thus inducing a 2DHG [51–53]. For this same reason, electron transfer into the unoccupied Al_2O_3 sites has been observed to induce a *p*-type inversion layer in *n*-type silicon surfaces [54]. A schematic depicting this charge transfer mechanism is shown in Fig. 3.4.

3.1.4 Step-by-Step Fabrication Process

The fabrication process of H:diamond devices can be separated into three categories: the formation of conductive and insulating surfaces, the deposition of ohmic metal contacts, and the passivation of the active regions. The fabrication process of H:diamond devices is summarized below, and a detailed runsheet is available in Appendix B.

The H:diamond devices were fabricated as follows. A schematic of this process is shown in Fig. 3.5(a). (i) The diamond surface was hydrogen-terminated under a high-power plasma in

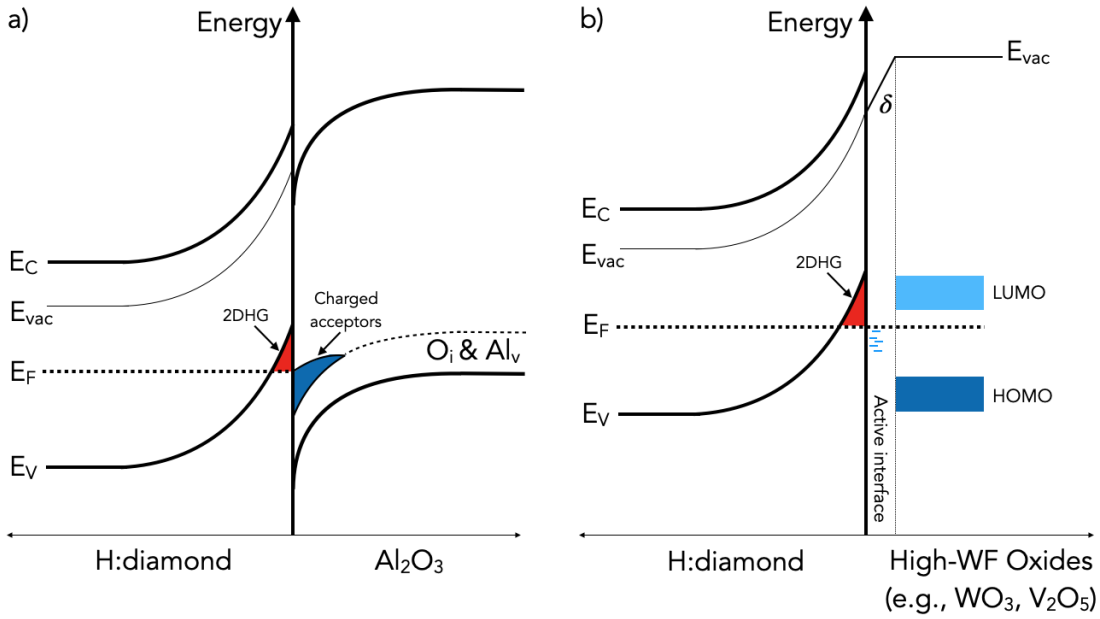

Figure 3.4: Schematic of charge transfer mechanism of H:diamond valence band electrons into (a) Al_2O_3 and (b) High work-function oxides such as WO_3 and V_2O_5.

a microwave CVD-chamber for 30 min. (ii) Bond pads regions were patterned and exposed to 100 W oxygen plasma for 90 seconds. This ensured that the metal bond pads adhered well, as discussed in section 3.1.2. (iii) Ti/Pt (5/20 nm) was evaporated and lifted off to realize metal bond pads. (iv) Au ohmic contacts (100 nm) were deposited using the same procedure as the prior step with the exception of the O-plasma. The Au overlaid the bondpads while making contact with the H-terminated surface. The resulting O:diamond/Ti/Pt/Au pads ensured ease of wirebonding and probing, while leaving the delicate H:diamond/Au in tact. (v) Isolation regions were patterned and exposed to 100 W O-plasma for 90 s. This step defined the active regions and electrically isolated the devices. (vi) The surface was passivated with 25 nm of Al_2O_3 via atomic layer deposition at 250°C. The oxide interface provides acceptor states for the 2DHG formation, and also stabilizes the 2DHG over time and over a wide range of temperatures [31, 39]. Finally, for the fabricated FETs, Al/Pt (30/20 nm) was evaporated and lifted off to realize metal gates.

3.1.5 Types of Devices Fabricated

In order to measure the sheet-conduction properties of H:diamond surfaces, Hall-effect structures were patterned. Moreover, to demonstrate H:diamond as a platform for devices, two types of FETs were patterned: metal semiconductor and metal-insulator-semiconductor (MISFETs and

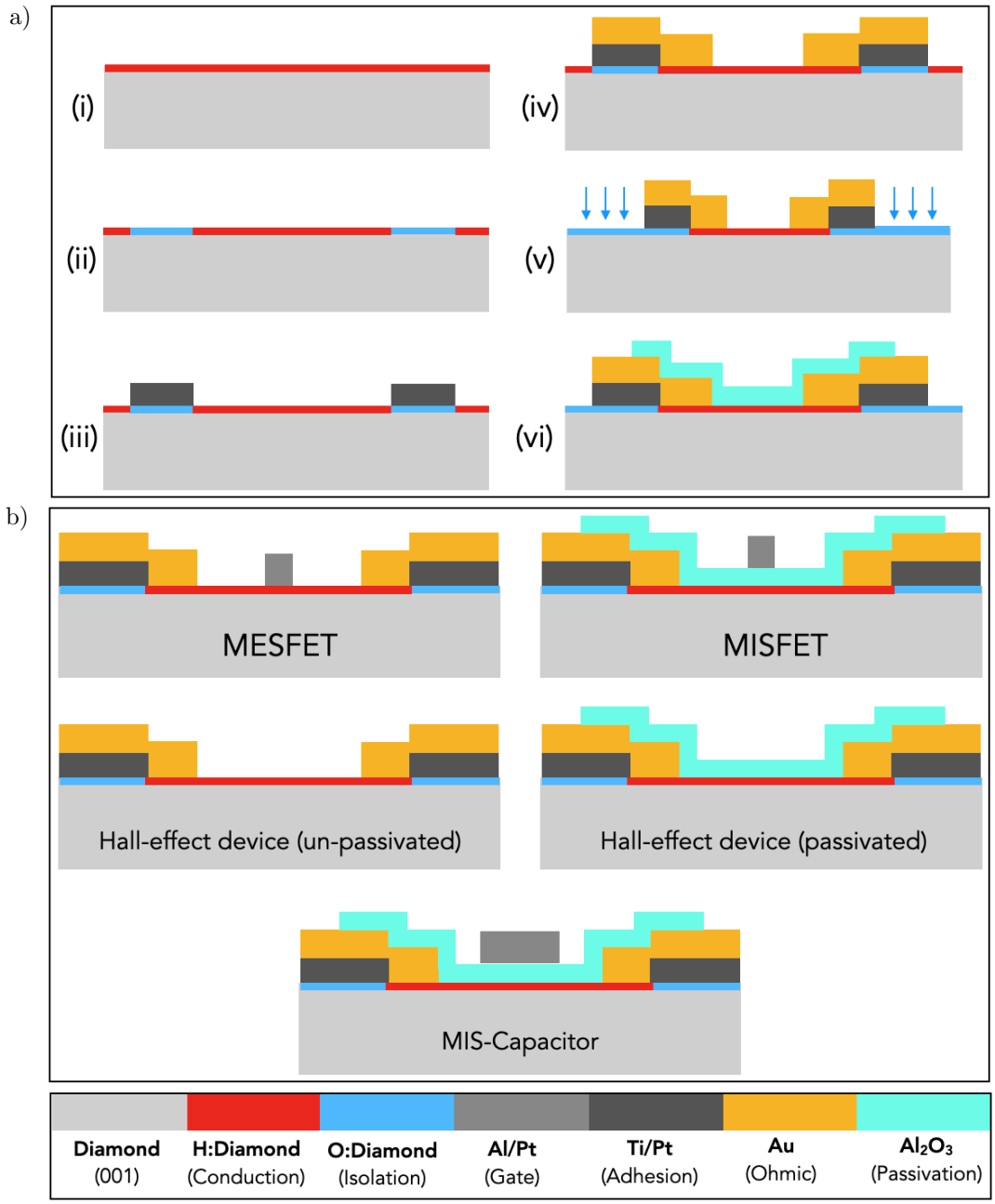

Figure 3.5: (a) Outline of the fabrication process. (i) Hydrogen-termination of (001) diamond surface, (ii) oxygen-termination of bond-pad regions, (iii) Ti/Pt evaporation for bond-pads, (iv) Au evaporation for ohmic contacts, (v) electrical isolation via oxygen-plasma, as indicated by the arrows, and (vi) atomic layer deposition of Al_2O_3. (b) Schematic of each device used in this work.

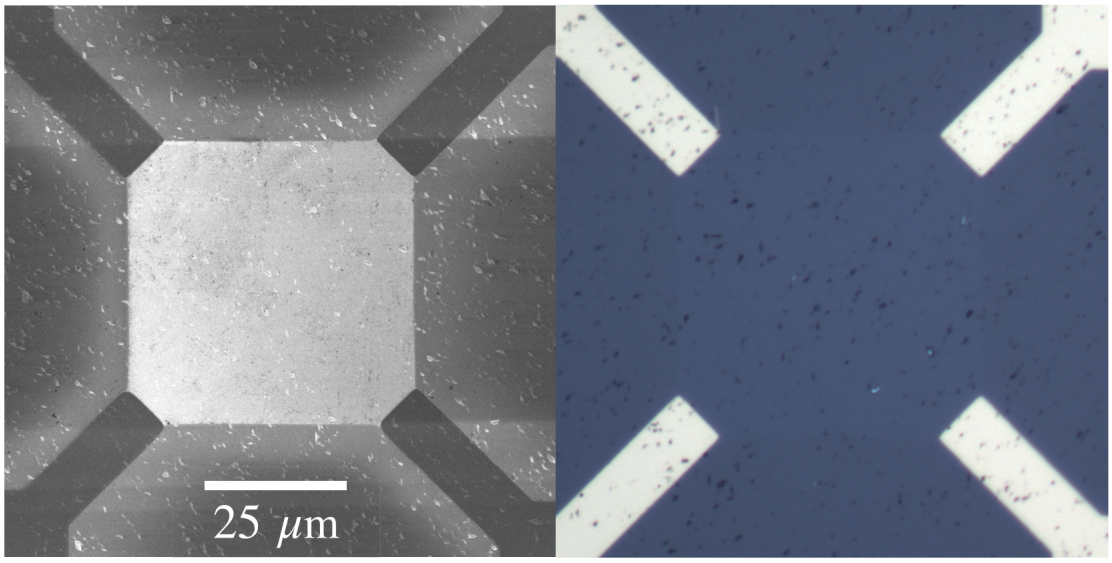

Figure 3.6: Images from a SEM (left) and OM (right) of the fabricated Hall-effect device. The bright square at the center of the SEM image is the H-terminated active region. The bright and dark spots (shown in the SEM and OM images, respectively) are etched pits caused by the H-plasma exposure.

MESFETs). Finally, MIS-capacitors were patterned to characterize the quality of the passivation layer.

Fig. 3.5(b) is a schematic of the H:diamond devices used in this thesis. As discussed previously, Schottky contacts can be used to create MESFETs. This is achieved using a metal with low electronegativity as our gate contact. Aluminum contacts were used in this case.

Show in Fig. 3.6 is a scanning electron microscope (SEM) and optical microscope (OM) image of the resulting Hall-effect device.

3.2 Characterization and Analysis of 2DHG Properties

In this section we analyze the multiple scattering mechanisms associated with hole transport in H:diamond using the experimental data of the fabricated Hall-effect devices. The theoretical mobility model introduced in section 2.3.2 and Appendix A is then used to interpret the experimental results. Four scattering mechanisms are discussed, surface impurity (SI), surface roughness (SR), non-polar optical phonon (NOP) and acoustic phonon (AP) scattering. As discussed in Appendix A, two types of SI scattering is observed, denoted as types (i) and (ii).

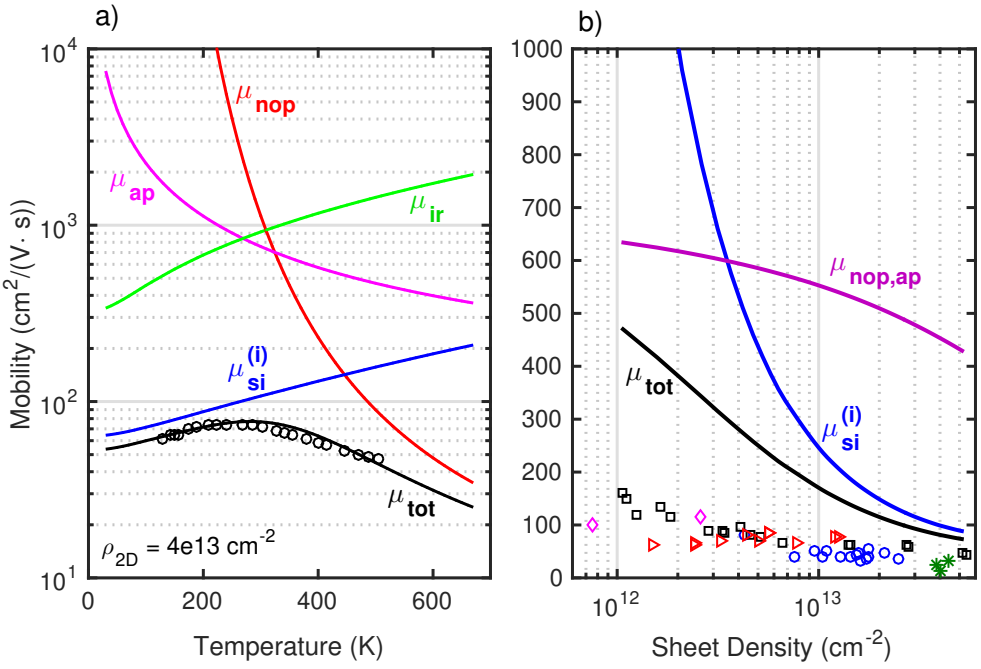

Figure 3.7: (a) Calculated Hall mobility as a function of temperature. The data points are reported by H. Kasu *et al.* [34], where the sheet density was approximately 4×10^{13} cm^{-2}. Surface roughness was fitted with parameters $\Delta = 1.2$ nm and $\Lambda = 5$ nm. (b) Calculated mobilities at T = 300 K with scattering by phonons and SI of type (i) are included. As shown, there is poor agreement with the total mobility and the multiple data points at low sheet density [31, 36, 37, 56].

3.2.1 Testing Mobility Model at High Sheet Density Limit

We begin by comparing our model to a model previously reported by Y. Li *et al.* [55] using experimental data by H. Kasu *et al.* [34], which was reported to have a high sheet density of $\sim 4\times10^{13}$ cm^{-2}. The previous model primarily used SI and SR scattering for fitting to the data at low-to-intermediate temperatures. Here we repeat this fitting using our model, which allows us to test our calculations to the limit of higher sheet densities. This starting point will subsequently illuminate the shortcomings of only considering type (i) SI and SR scattering, which turn out to be insufficient for lower sheet densities. A complete version of the model, which considers type (ii) SI scattering, will be compared to the Hall-effect measurements on the fabricated devices of this work, where sheet densities are as low as $\sim 2\times10^{12}$ cm^{-2}.

The fitting of our calculations to the data by H. Kasu *et al.* is presented in Fig. 3.7(a). The material parameters used are listed in Table 3.1. In the mobility model by Y. Li *et al.*, approximations such as the 2D Fermi wave vector ($k_F = \sqrt{2\pi\rho_{2D}}$) and a single equivalent isotropic valley model were used. This therefore yielded temperature independent functions for SI and SR

Parameter	Symbol (units)	Value [Ref.]
NOP Deformation potential	D_{op} (eV/cm)	1.4e10
AP Deformation potential	D_{ap} (eV)	8 [59]
LO-phonon energy	$\hbar\omega_0$ (meV)	165 [59]
Material density	ρ (kg/m^3)	3515 [60]
Sound velocity	v_s (m/s)	17536 [60]
Dielectric constant	ε_s (ε_0)	5.7 [60]
Surface acceptor separation	d (Å)	2.1

Table 3.1: Material parameters used in the 2DHG H:diamond scattering calculations.

scattering, as well as distinct fitting parameters. To performed this calculation using our multi-band treatment and averaging over energy (Eq. (2.12)), we select the same value for the RMS roughness height as Y. Li *et al.*, $\Delta = 1.2$ nm, which is a reasonable value taken from Ref. [56]. The correlation length Λ was fitted to be 5 nm. For NOP scattering, the coupling constant D_{nop} was fitted to be 1.4×10^{10} eV/cm. As for type (i) SI scattering, it is presumed that the sheet separation of the charged surface acceptors and the 2DHG is the summation of the C-H dipole bond length (~ 1.1 Å, [57]) and half the thickness of the negatively charged acceptors (~ 2 Å, [58]), which gives us $d = 2.1$ Å. Finally, the negative surface acceptor density was presumed to exactly balance the positive sheet density, giving $N_{si}^{(i)} = \rho_{2D}$.

3.2.2 Impurity Scattering by Charged Acceptors

Fig. 3.7(a) shows that SI scattering by negatively charged acceptors (i.e., type (i)) is the dominant mechanism, particularly at low to intermediate temperatures, which is attributed to the high sheet density of $\sim 4 \times 10^{13}$ cm^{-2}. It is important to note the slight decrease in μ_{tot} at lower temperatures. Since ionized impurity scattering is much higher near the valence band edge (e.g., see Fig. 3.9(b)), the Fermi energy averaging of holes (Eq. (2.12)) is necessary to capture this behavior. As shown in Fig. 3.7(b), the type (i) dominance is further evident above 1×10^{13} cm^{-2}, where $\mu_{si}^{(i)}$ drops to commonly measured mobility values. However, as given by the factors in Eqs. (A.6) and (A.8), the SI and SR scattering rates increase with $\rho_{2D} (= N_{si}^{(i)})$ and ρ_{2D}^2, respectively. Thus, at $\rho_{2D} \ll 1 \times 10^{13}$ cm^{-2} and at 300 K, this modeling framework predicts a total hole mobility that is limited by phonons, which is significantly higher than what is measured experimentally, as shown in Fig. 3.7(b). This inaccuracy is further evident at lower temperatures, where scattering by phonons becomes negligible. Thus, it is clear that an additional scattering mechanism is required to explain this behavior.

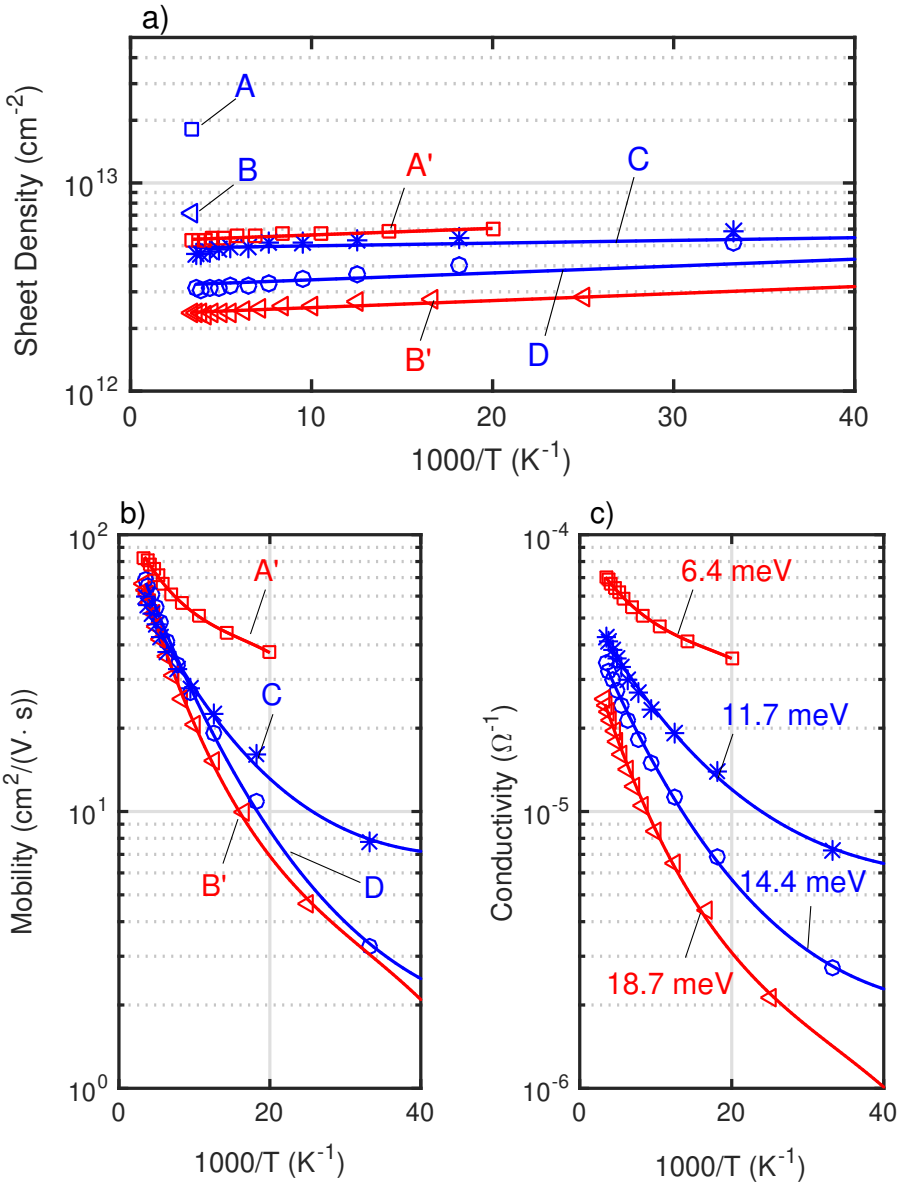

Figure 3.8: Hall measurements of the four fabricated samples as a function of inverse temperature. (a) Measured sheet densities for samples A, B, C, and D. We use the prime notation (i.e., A' and B') to denote passivation with Al_2O_3. The corresponding Hall mobility (b) and conductivity (c) decline at a rate that is dependent on the sheet density (a). The activation energies are labeled in (c).

3.2.3 Impurity Scattering by Surface Disorder of C-H Dipoles

To explore this further, Hall-effect measurements performed on the fabricated Hall-effect devices are presented, followed by an analysis of the data and a fitting to the scattering model. Prior to passivation with Al_2O_3, Hall-effect measurements of the samples, denoted as A, B, C, and D, were performed after several days of being air-exposed. Afterwards, samples A and B were passivated with 25 nm of ALD-Al_2O_3, which we denote as samples A' and B'. Finally, Hall-effect measurements were performed over the range ∼25 K to 300 K. The measurements were taken from RT to low temperatures, and back up to RT, and negligible hysteresis was observed. The results are shown in Fig. 3.8, plotted as a function of inverse temperature.

We first observe that, prior to passivating samples A and B, the sheet densities are significantly higher than their passivated counterparts (A' and B'). As reported in other works, a drop in the sheet density after the deposition of Al_2O_3 is common [31, 50], which is attributed to the lower density of surface acceptors in Al_2O_3 in comparison to air-adsorbates. It is also shown in Fig. 3.8(a) that the ρ_{2D} is rather constant as the substrate temperature drops to <50 K. It is interesting to observe that ρ_{2D} does not drop precipitously at low temperatures, as it has in one study done by C. Nebel *et al.*, where they reported a hole "freeze-out" with a critical temperature of 70 K on H:diamond surface, a phenomenon that is explained by a classical mobility-edge model [61]. Such "freeze-out" of carriers is observed when the sheet density collapses below a critical temperature. For H:diamond, this would be attributed to a confinement of holes into so-called "localized states" existing near the valence band edge, presumed to arise from *short-range* potential fluctuations at the surface. Above the critical temperature, holes would posses the thermal energy to excite into de-localized energy states which span the plane of the 2D well (i.e., "extended states"), thus allowing the holes to conduct freely.

Thermal Activation Energies of Mobility and Conductivity

Such a "freeze-out" phenomenon, however, was not observed here. Instead, our work is consistent with what was reported by J. Garrido *et al.*, whereby the conductive properties of the 2DHG [Fig. 3.8(a)] exhibit a temperature-independent ρ_{2D} [38]. Moreover, a thermal activation energy is observed for the mobility and conductivity, as shown in Figs. 3.8(b) and labeled in (c), respectively. Specifically, the mobility and conductivity of the samples with lower sheet densities have a higher thermal activation energy (i.e., the decrease rate as T→ 0 K is higher), as labeled in Fig. 3.8(c). As discussed by J. Garrido *et al.*, this behavior can be explained by an early model formulated by E. Arnold, which predicted a similar temperature dependence of the Hall mobility, conductivity, and sheet density in the case of inverted 2D electron channels in Si/SiO_2 structures

[62]. Using semi-classical percolation theory, Arnold explained that electrons conduct in the presence of *long-range* potential fluctuations along the conduction band E_C, where "metallic" regions ($E_F > E_C$) coexist with "insulating" regions ($E_F < E_C$). When the Fermi energy range is narrow ($T \rightarrow 0\ K$), electrons percolate around the "insulating" regions via the "metallic" network. Thus, since a lower sheet density has a Fermi level that is much closer to E_C, the rate at which electrons scatter is enhanced as the Fermi energy range is narrowed.

We observe here that Arnold's framework can explain the behavior in Fig. 3.8, and that holes in the 2D well percolate around long-range potential fluctuations induced by the surface impurities of types (i) and (ii). This is evident from the behavior in the mobility and conductivity in Fig. 3.8, where the general trend of increasing activation energy with decreasing sheet density is clearly observed. However, the measurements for samples A' and C exhibit an unusual difference. According to Arnold's framework (subsequently reinforced by J. Garrido *et al.* for H:diamond), the activation energy is primarily determined by the sheet density. However, the sheet densities of samples A' and C are very similar, yet yield significantly different activation energies (6.4 meV and 11.7 meV, respectively) . One explanation that can resolve this inconsistency is to presume that sample A' has a higher periodicity of C-H dipoles at the surface. This presumption is explained by noting the measured sheet density for sample A' prior to passivation (sample A), which was 1.80×10^{13} cm^{-2}. This is four-fold higher than the sheet density of sample C (4.50×10^{12} cm^{-2}). It is reasonable to expect that a high C-H dipole density results in a higher ρ_{2D}. This was reported by K. Hirama *et al.*, who showed that surfaces with a higher C-H density induced a a higher 2DHG density [56]. Thus, if we presume that sample C has a lower C-H dipole density as sample A', then under Arnold's framework, holes would "percolate" around a larger density of "insulating" regions in sample C than in A' [Fig. 3.9]. Moreover, the average energy of the insulating barrier heights would effectively increase, since their larger density would overwhelm the benefit of screening. The result would thus be a higher activation energy for sample C, despite having a comparable sheet density and Fermi energy as sample A'. This phenomenon is discussed further in Chapter 4.

The work by K. Hirama *et al.* was in the context of out-of-plane orientations of single-crystal diamond, where the carbon density of the restructured surface in the (110) orientation is greater than the (001). Hence, after exposure to a hydrogen plasma, the (110) surface yielded a higher C-H and hole sheet density than the (001). Moreover, this same study showed that a higher CVD temperature induced a higher sheet density, which is likely explained by a more complete H-termination. This was shown directly by T. Ando *et al.*, where Fourier-transform infrared spectra exhibited a stronger signal of C-H vibrations for diamond powder that was H-terminated

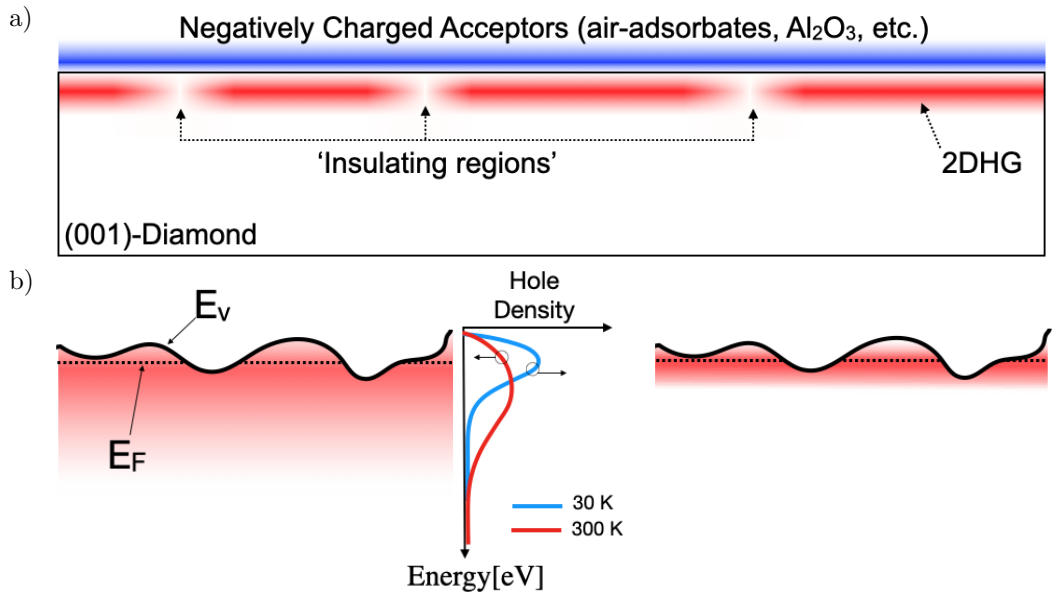

Figure 3.9: (a) Schematic of the "insulating" regions along the 2DHG, presumed to arise from incomplete H-termination. Other irregularities related to the C-H surface may also induce this insulating effect. (b) A schematic demonstrating the hole distribution as a function of energy for low and high temperatures in the presence of valence band ripples (induced by ionized acceptor states, insulating regions, and other surface anomalies). At high temperatures, this scattering rate mechanism decreases since a greater proportion of holes can thermally propogate throughout the well.

at higher CVD temperatures [63]. The authors of the latter study attributed the increased C-H signals to greater adsorption of H atoms on the diamond surface.

Other Sources of Type (ii) Scattering

Alternatively, the nature of the charge transfer mechanism into the acceptor states of Al_2O_3 and air-adsorbates may have a role in the activation energy differences observed between samples A' and C. The acceptor source from the air is believed to arise from water redox reactions [28], whereas trap states near the valence band of Al_2O_3 are believed to act as the acceptors [8, 64]. Depending on the surface temperature and environments throughout fabrication and characterization, the charge transfer process may be kinetically suppressed [65], or the C-H dipoles may react and dissociate with other molecules (e.g., as occurs during NO_2 exposure [66]). However, we note that since negligible hysteresis is observed in the temperature Hall-effect measurements, any additional factors influencing the activation energies are believed to be reversible.

We note that in many diamond substrates, background impurities along the 2DHG channel may also contribute meaningfully to hole scattering. Nitrogen and boron impurities are common

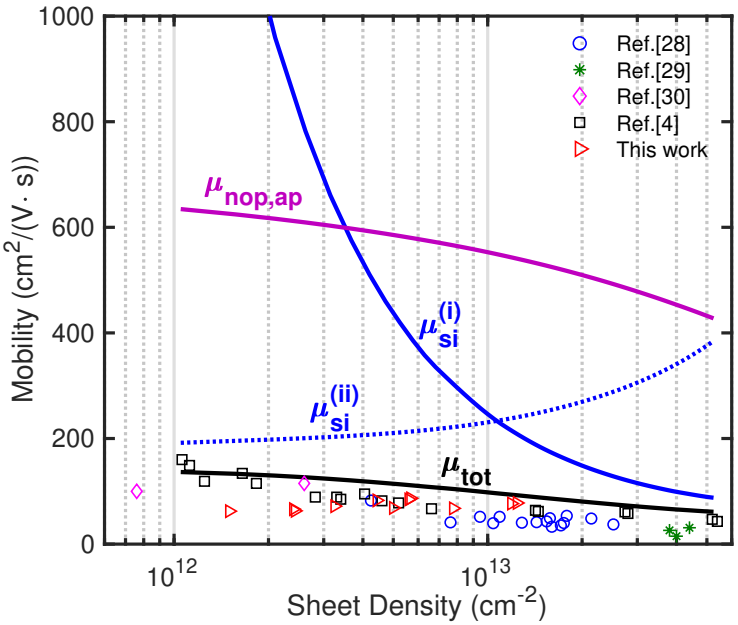

Figure 3.10: Measured and calculated Hall mobilities as a function of sheet density at T = 300 K. A value of $\mathcal{N}_{si}^{(ii)} = 5 \times 10^{12}$ cm^{-2} was arbitrarily selected to qualitatively demonstrate the trend of type (ii) SI scattering as a function of sheet density. Unlike in Fig. 3.7(b), the calculated total mobility is in agreement with the experimental values.

in synthesized diamond, for example, and hydrogen atoms may penetrate through the surface during the H-plasma treatment process. Although the SI relaxation time (Eq. A.6) is for remote impurities, integrating along z yields an expression for bulk impurities, with a fitting parameter in units cm^{-3}. However, one would intuit that background scattering would increase as the H-plasma power and exposure time increase. To the authors' knowledge, there no evidence of this, and one study actually found mobility to increase at higher plasma powers [36]. Finally, other complex surface phenomena, such as a non-homogeneous distribution of surface acceptors [67], the existence of oxygen-related sites [65], or a variation of C-H surface reconstruction [24], may explain this type (ii) SI scattering process.

Importantly, we emphasize that the prevalence of potential fluctuations can explain the discrepancy shown in Fig. 3.7(b), where the experimental mobility remains relatively stagnant even at low sheet densities. Here we attempt to model this phenomenon, which we denote as SI scattering of type (ii). Unlike type (i) where $N_{si}^{(i)} = \rho_{2D}$ and $d > 0$, type (ii) SI scattering is related to the disorder that is prevalent at low ρ_{2D} values, with $d = 0$ and a fitting parameter denoted by $\mathcal{N}_{si}^{(ii)}$. Thus, although $N_{si}^{(i)}$ scales with ρ_{2D}, the value of $\mathcal{N}_{si}^{(ii)}$ remains constant or may increase as ρ_{2D} decreases.

Figure 3.10 is a duplicate of Fig. 3.7(b) with $\mu_{si}^{(ii)}$ included. Here, the fitting parameter $\mathcal{N}_{si}^{(ii)}$

was arbitrarily set to 5×10^{12} cm^{-2} in Eq. (A.6) in order to qualitatively demonstrate type (ii) SI scattering (a precise fit would be needed for each data point). It is evident here that an increasing sheet density – and thus Fermi energy – gives a steady rise in $\mu_{si}^{(ii)}$. This is expected given that SI scattering is more prominent near the valence band edges. On the other hand, however, $N_{si}^{(i)}$ increases with the sheet density, which reduces $\mu_{si}^{(i)}$. Thus, for $\mathcal{N}_{si}^{(ii)} = 5 \times 10^{12}$ cm^{-2}, a cross-over point of SI scattering of types (i) and (ii) arises near 1×10^{13} cm^{-2}. The result of combining both types SI scattering is to effectively create a mobility "ceiling" for holes in H:diamond surfaces, which agrees well with the experimental Hall data from multiple references.

3.2.4 Mobility Model Fit to Fabricated Samples

A precise fitting of the mobility calculations to the experimental data was performed for samples A' and B' from 50 K to 700 K, as shown in Fig. 3.11. As with the low temperature measurements, negligible hysteresis was observed for high temperature measurements. After fabrication of these samples, but prior to passivation, AFM measurements were taken on the active regions (Fig. 3.12). The average measured root-mean-squared height and correlation length were $\Delta \approx 0.80 \pm 0.10$ nm and $\Lambda \approx 60 \pm 10$ nm, respectively. Note that the mobility calculations for SR scattering (μ_{SR}) are absent in Fig. 3.11. This is largely due to the large Λ measured via AFM, which reduces SR scattering significantly. Moreover, since the sheet density is rather low for samples A' and B', the magnitude of SR scattering is further reduced since it is proportional to ρ_{2D}^2 (Eq. (A.8)). Thus, μ_{SR} is ignored here. For higher temperatures, phonon scattering is slightly reduced for lower sheet densities, which is due to a reduction of holes occupying energy states exceeding the LO-phonon energy (and hence reducing scattering by NOP emission). As with Fig. 3.7(a), the coupling constant for NOP is fitted to $D_{nop} = 1.4 \times 10^{10}$ eV/cm. This is in close agreement with values reported for bulk diamond, where Ref. [68] reported 1.2×10^{10} eV/cm and Ref. [59] reported 0.7×10^{10} eV/cm. The AP deformation potential D_{ap} was set to 8 eV, as it has also been fitted experimentally in other works for bulk diamond [59, 69].

As anticipated, SI scattering of types (i) and (ii) are dominant at low-to-intermediate temperatures (up to ~450 K). This is attributed to the close proximity of the charged acceptors (i.e., $\mu_{si}^{(i)}$, $d = 2.1$ Å) and disorder related to the C-H surface (i.e., $\mu_{si}^{(ii)}$, $d = 0$ Å), the latter of which remains prevalent even at lower ρ_{2D} values. For samples A' and B', an increase in the fitting parameter $\mathcal{N}_{si}^{(ii)}$ was required for the lower ρ_{2D}, which suggests that there is an increase in the potential fluctuations induced by C-H related disorder. As discussed earlier, the nature of such disorder may include incomplete H-termination, a hypothesis also mentioned in Refs. [38, 61]. Other complex surface chemistry, as mentioned previously, may also be involved. In addition

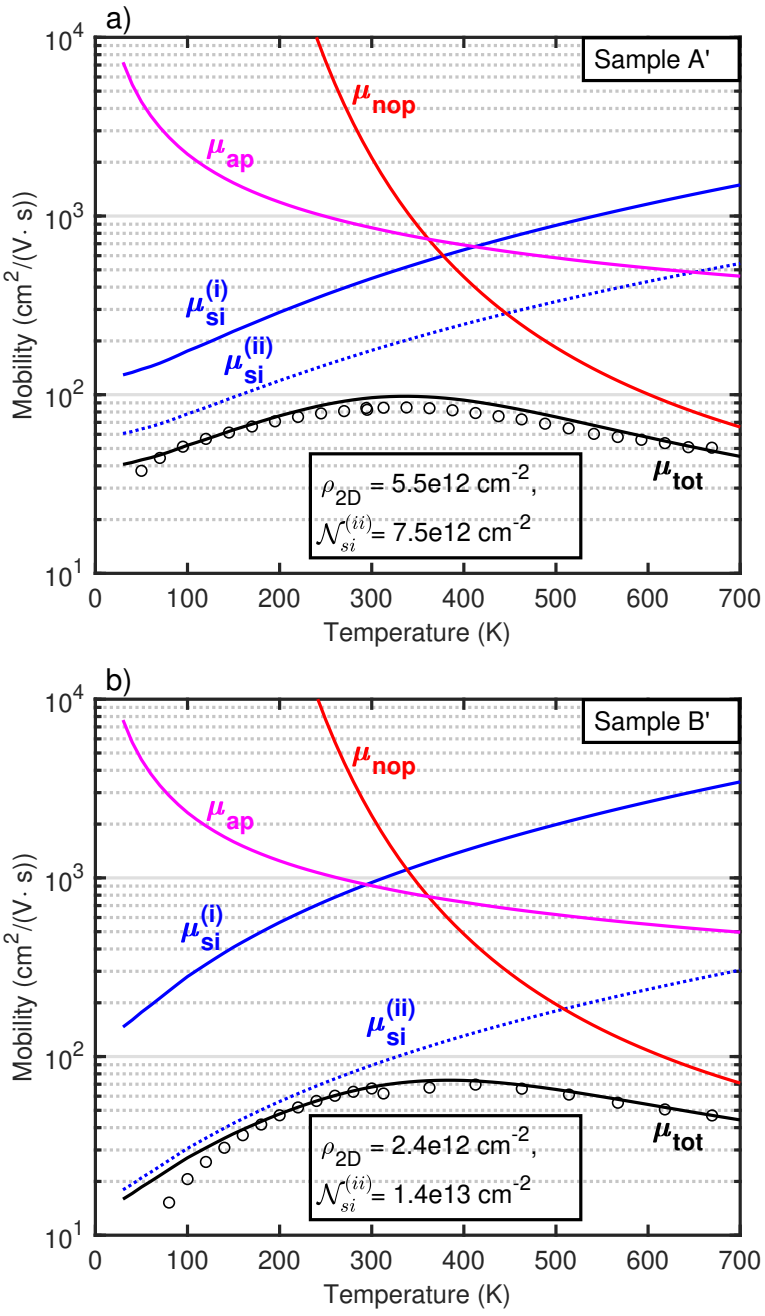

Figure 3.11: Measured and calculated Hall mobilities as a function of temperature for samples A' and B'. (a) Calculations fitted to sample A' data. A moderate sheet density of 5.5×10^{12} cm^{-2} yields a comparable fitting parameter for $\mathcal{N}_{si}^{(ii)}$. (b) Calculations fitted to sample B' data. A low sheet density of 2.4×10^{12} cm^{-2} yields a much higher fitting parameter for $\mathcal{N}_{si}^{(ii)}$.

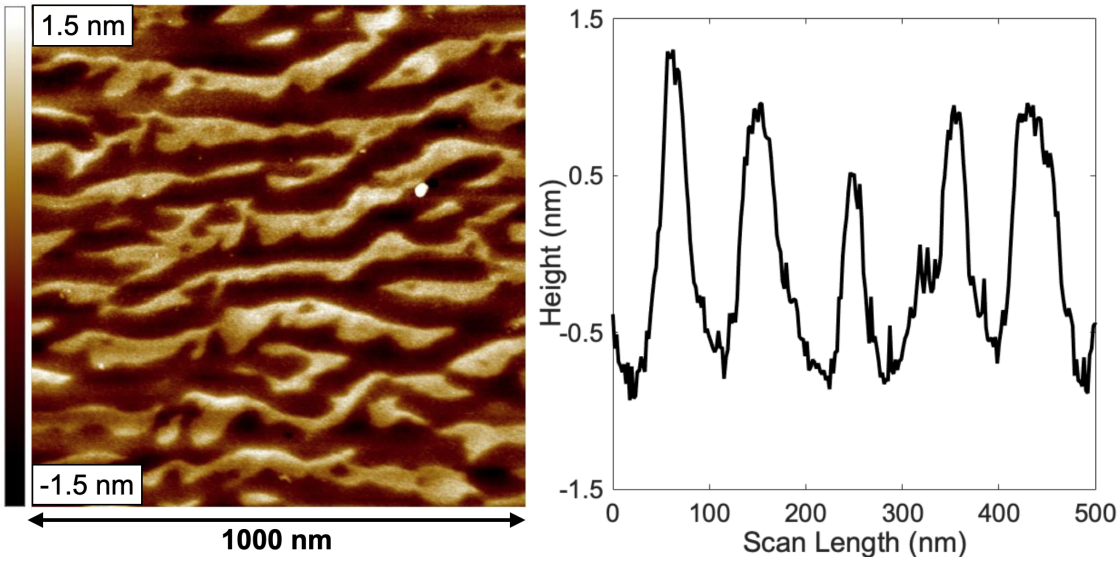

d

Figure 3.12: AFM scan of the active region after H-termination

to the increasing parameter $\mathcal{N}_{si}^{(ii)}$, a lower sheet density [Fig. 3.11(b)] exhibits a steeper decline (and thus a higher activation energy) in both $\mu_{si}^{(i)}$ and $\mu_{si}^{(ii)}$ as T$\rightarrow$ 0 K, which is precisely what is observed in the experimental Hall data. The ρ_{2D}-dependent activation energy is also shown in the 1/T representation of the samples in Fig. 3.8(b) and (c), as well as in Ref. [38]. This effect is attributed to the larger occupation of holes near the valence band edge ($E_V - E_F \rightarrow 0$ eV) where the scattering rate is higher.

Efforts to boost the 2D hole gas conductivity on H:diamond surfaces must therefore attend to two design parameters. The first involves the separation of the charged surface acceptors from the 2D hole gas, evidenced by Eq. ($A.6$) where μ_{si} is exponentially dependent on d. The second is to reduce the effect of type (ii) SI scattering by reducing the potential fluctuations induced by other factors such as incomplete hydrogen termination. However, the exact origins of this scattering type is largely unexplored. Thus, extensive experiments studying the surface chemistry on H:diamond are required to find the solutions necessary to boost the conductivity and advance this promising technology.

3.3 IV/CV Measurements of H:diamond FETs

In addition to Hall-effect devices, standard FET devices were fabricated in an attempt to demonstrate robust behavior on key devices metrics. As discussed in section 3.1.4, the FETs were

fabricated using Ti/Pt/Au metal bond pads for probing, where were the Au was overlaid as the source/drain electrodes. The oxide thickness for the FETs were approximately 25 nm of ALD-Al_2O_3, deposited at a chamber pressure of 250°C. The maskless lithography tool used for exposure had a minimum feature size just below 1 μm. Therefore, of all the fabricated FETs, the shortest gate length L_g and channel length L_{ch} were 1 μm and 6 μm, respectively. The FET channel width was 20 μm. As for the MESFETs, we discussed in section 3.1.2 that metals with a lower electronegativity exhibit Schottky behavior, as is the case with Al/H:diamond contacts. Thus, MESFETs were also fabricated by evaporating Al/Pt (20/30 nm) gate electrodes onto unpassivated H:diamond.

Shown in Fig. 3.13 is the I_DV_G and I_DV_D measurements of the H:diamond MISFETs. Using the linear extrapolation method, a threshold voltage of V_{th}=1.02 V was extracted from the transfer characteristics (note that the x-axes plotted here are flipped in sign) [70]. Shown in Fig. 3.13(b) is good saturation behavior, though there is a moderate dependence of I_D on V_D in the saturation region, which is evidence of channel modulation effects. Unfortunately, the maximum drain current at V_G=-3 V was measured to be ≈11 mA/mm. Hall-effect measurements were performed on this same substrate, and the 2DHG density and mobility were measured to be 3.32×10^{12} cm^{-2} and 53 cm^2/(V·s). Comparing to H:diamond FETs with other passivations, such as MoO_3 or NO_2-doped, this sheet density is over one order of magnitude lower [71–74]. The fixed negative charge is due to the relatively low acceptor density in the Al_2O_3 interface, which is seen commonly in literature [31]. As discussed before, the 2DHG density is dependent on the density of available acceptor states, the sources of which are defect states near the Al_2O_3

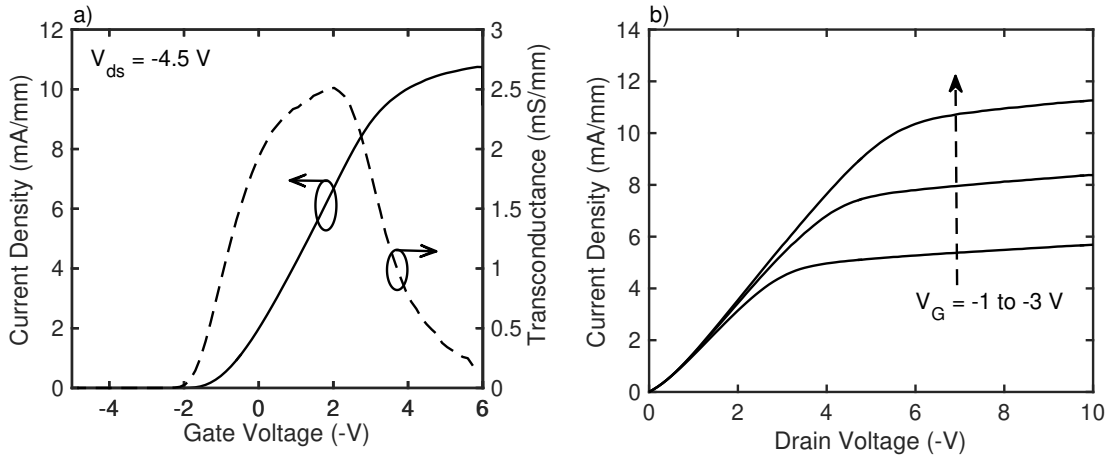

Figure 3.13: Al_2O_3/H:diamond MISFET curves for (a) drain current vs. gate voltage and (b) drain current vs. drain voltage. Gate length and channel are L_g = 1 μm and L_{ch} = 6 μm, respectively.

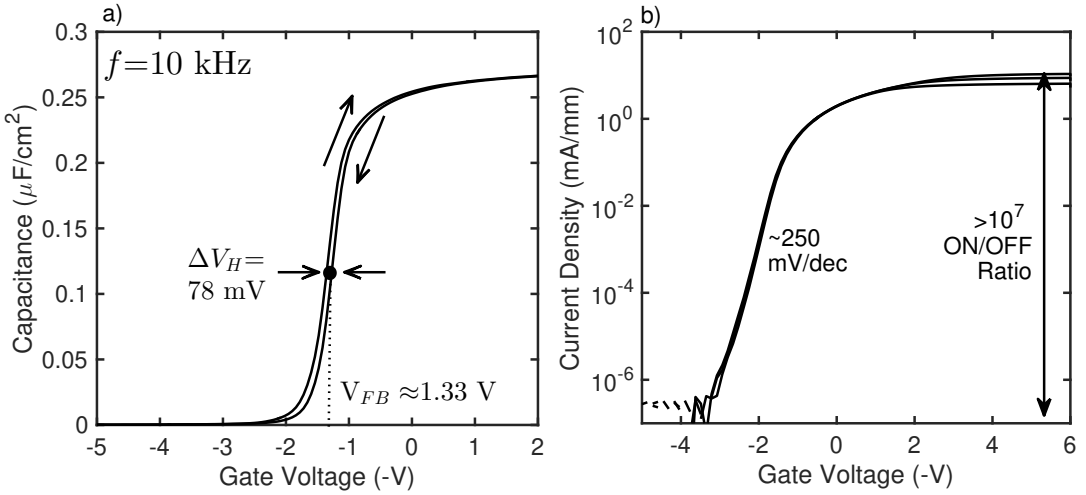

Figure 3.14: (a) Capacitance-voltage curves of MISCAP structures at a 10 kHz frequency. A small hysteresis value of ΔV_H=78 mV was measured. Using the max capacitance value (C_{ox}) and the known thickness of the Al_2O_3, it was determined that the dielectric constant $\epsilon_k \approx 7.34$. (b) Drain current vs. gate voltage plotted on a log scale, thus showing a high ON/OFF ratio and acceptable sub-threshold swing.

valence band [30]. Oxides such as MoO_3, on the other hand, have high work-functions such that the CBM is below the H:diamond VBM.

To further examine MISFET metrics, capacitance voltage curves, the ON/OFF ratio, and the sub-threshold swing were measured, as shown in Fig. 3.14. The maximum accumulation capacitance, also known as the oxide capacitance $C_{ox} \approx 0.26$ μF/cm^2, which corresponds to a dielectric constant $\epsilon_k = 7.34$ assuming a 25 nm-thick Al_2O_3 passivation layer. This agrees reasonably well for ALD-Al_2O_3 films [75]. Using the second derivative method (i.e., $d^2C(V)/dV^2 \approx 0$ when $V=V_{FB}$ [76]), a flatband voltage of $V_{FB} \approx 1.33$ V was extracted. This compares to the ideal flatband voltage of V_{FB0}=0.62 V, calculated using the work functions of Al (4.28 eV) and H:diamond (4.9 eV) [30, 74]. This positive shift in V_{FB} from the theoretical to experimental value suggests that there is a moderate concentration of fixed negative charge in the oxide, which can contribute to the 2DHG density by attracting holes to the surface. This charge can be estimated using the simple expression,

$$Q = C_{ox}\Delta V/q, \tag{3.1}$$

where q is the elementary charge magnitude. Thus, by substituting (V_{FB} - V_{FB0}) for ΔV, this corresponds to a fixed negative charge density $Q_f = 1.15\times10^{12}$ cm^{-2}. Further, the CV curve

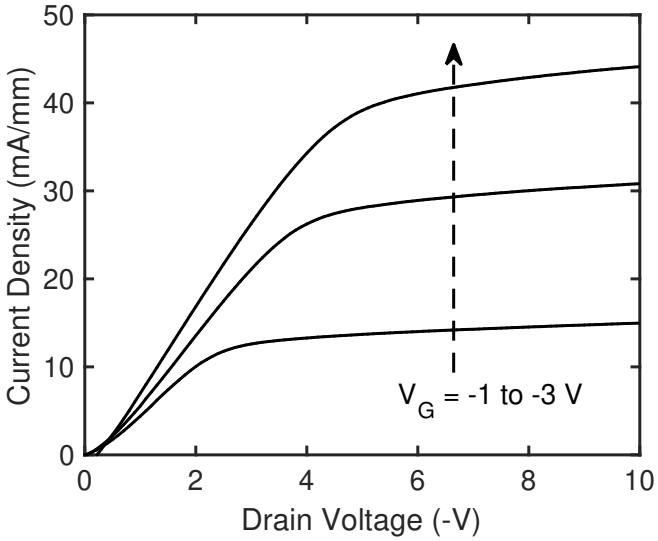

Figure 3.15: Drain current vs. Drain voltage of H:diamond MESFET. Such FETs can be realized using Schottky contacts directly on H:diamond. In this device, the metal gate was Al/Pt.

was swept bidirectionally at $f = 10$ kHz, which produced a small clockwise hysteresis value of ΔV_H=78 mV. This hysteresis was produced by charge trapping near the interface, which can also be estimated using Eq. (3.1). Thus, by substituting ΔV_H, a positively-charged trap density of $Q_t \approx 1.27\times10^{11}$ cm^{-2} explains the hysteresis behavior. This is a low value, which is promising for device stability. Given the moderately low measurement frequency of 10 kHz, it is reasonable to conclude that deeper, border-like traps are included in Q_t.

Moreover, Fig. 3.14(a) exhibits a large ON/OFF ratio. Due to the current detection limit of the parameter analysis, the ratio is measured to be from 10^7 to 10^8. The sub-threshold slope (SS) was measured to be $\sim$ 250 mV/dec, which is a reasonable for a 25 nm oxide. The SS may be further reduced by altering the ALD conditions to deposit higher-k dielectric films, thus boosting C_{ox} and in turn lowering the SS.

Finally, we show the robust MESFET behavior in Fig. 3.15, which was realized by depositing a Al/Pt (20/30 nm) gate directly onto unpassivated H:diamond. It is clear that the current density is significantly higher, which is owed to the superior acceptor density in air-doped diamond in comparison to the acceptor density in ALD-Al_2O_3. Once again, the values for L_g, L_{ch}, and the channel width are 1 μm, 6 μm, and 20 μm, respectively. Thus, channel modulation behavior is observed at the saturation regions. Both MISFET and MESFET structures were useful in studying the radiation-induced degradation observed in H:diamond. This will be the subject of the next chapter.

3.4 Chapter Summary

We have fabricated Hall-effect devices on multiple diamond substrates with varying 2DHG conduction properties. Extensive Hall-effect measurements were taken at temperatures ranging from 25 K to 700 K, and a scattering model was developed to explore the mobility-limiting mechanisms. A multi-band treatment of the HH, LH, and SO band was included using a Schrödinger/Poisson solver, where only the first energy level of each band was considered. The Hall-effect measurements at low-to-intermediate temperatures suggest that long-range potential fluctuations exist for a wide range of ρ_{2D}, which contributes to the "ceiling" observed for the hole mobilities at low sheet densities. These fluctuations may arise both from charged surface acceptors and disorder related to the C-H surface. The nature of this disorder is a subject that remains to be studied.

Moreover, IV and CV measurements were taken on MISFETs, MESFETs, and MISCAPs, in order to analyze the FET behavior. A reasonable ON/OFF ratio and subthreshold slope was observed. However, altering the ALD conditions can improve these values by either lowering the oxide thickness or increasing the dielectric constant. Using CV measurements, it was determined that negatively fixed charge exists in the oxide, and that a small density of traps become positively-charged near the interface as the gate bias is swept, thus producing a small hysteresis behavior. This is promising for robust FET operation. Finally, reasonable $I_D V_D$ saturation was observed for both MISFETs and MESFETs, although the MESFET drain current was significantly higher.

Chapter 4

Radiation Response of H:diamond Devices

As discussed previously, diamond-based electronics have been investigated for many years, showing promising performance for high-power and high-frequency applications, owing to its figures of merit (FOM). Such FOM values are high due to diamond's wide band gap, high breakdown voltage, high thermal conductivity, and high saturation velocity. Moreover, diamond's relatively small lattice constant makes it incredibly hardened, thus exhibiting high resistance to particle radiation. As shown in Fig. 2.8, for example, the energy requiring to permanently displace a carbon atom from the diamond's lattice is considerably higher than other semiconductors. This makes diamond-based devices an attractive candidate for radiation-rich environments. However, most of the work of irradiated diamond has focused on radiation-monitoring applications, which usually consists of two electrodes for biasing and charge collection [77–82]. This includes both charged ion irradiation and neutron irradiation [83–86]. Additionally, one paper studied the effects of H:diamond FETs under neutron irradiation, which concluded that the operation post-irradiation was robust and degradation effects were minuscule or undetectable [86].

Unlike neutrons, however, penetrating charged particles interact strongly with the electron subsystem of a lattice via ionization (Fig. 2.6(a)), and such particles are highly abundant in space environments (Fig. 2.6(b)). For hydrogen-terminated diamond, several questions arise in the context of charged particle irradiation. Although the threshold atomic displacement energy is high for diamond, the ionization that occurs as a charged particle penetrates the lattice may degrade the device architecture, and thus its electrical performance. For example, H:diamond passivated with oxides are vulnerable to total ionizing dose (TID) effects. The material properties

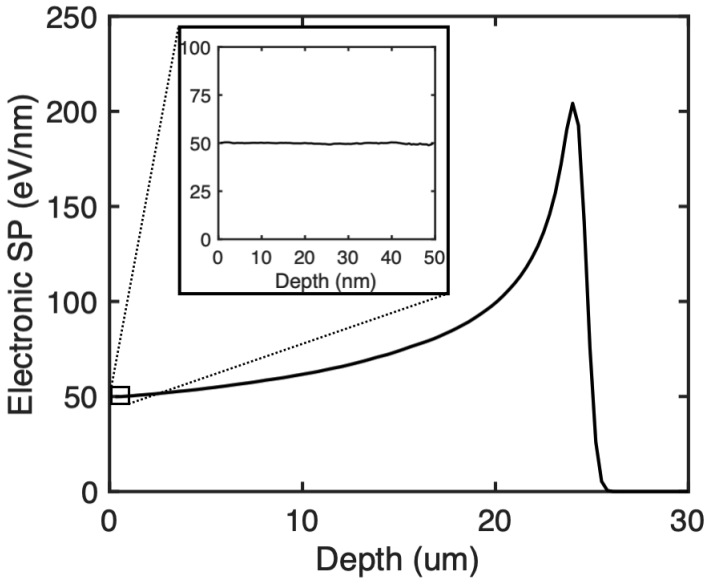

Figure 4.1: SRIM simulation of electronic energy deposition by one 2 MeV proton penetrating single crystal diamond [87].

of oxides are notoriously effected over time as they are exposed to radiation. This can shift the threshold voltage of the device and degrade the mobility, for example. Thus, technology with oxides as part of their architecture are especially vulnerable, and must be graded for radiation-environments prior to being exposed to penetrating charged particles. Moreover, the *p*-type conductivity of H:diamond relies on the C-H bonds at the diamond surface. These bonds may thus dissociate as the lattice is locally ionized by penetrating charged particles. Over large integral fluences, the C-H dissociation may be significant enough to degrade the electrical properties.

Figure 4.1 shows the energy deposited via ionization (i.e., electronic stopping power) for a 2 MeV proton penetrating a diamond lattice. We can see from the inset that superficially, the proton energy is deposited at a rate of 50 eV/nm, or about ∼18 eV for every lattice constant of diamond. This energy deposition rate occurs locally along the proton trajectory, thus producing a cylindrical ionization volume. However localized that these effects may be, it is important to determine if the integral fluence is sufficient to modify the electrical properties. Thus, in this work, we study this by proton-irradiating four H:diamond samples at two different fluences. The proton energy used is 2 MeV, as it is within a typical energy range for particles in space environments. The fluences were 0.5 $\times 10^{14}$ and 1 $\times 10^{14}$ cm^{-2}. The proton irradiation was conducted in the Tandem Accelerator at the Ion Beam Materials Laboratory at Los Alamos National Laboratory.

To study the oxide TID effects, two of the irradiated samples were passivated Al_2O_3/H:diamond

structures with fabricated MISFETs, MISCAPs, and Hall-effect devices. It is worth noting, however, that any degradation intrinsic to the H:diamond structure may be difficult to decouple from the electrical impact induced by the degraded oxide. For this reason, the other two irradiated samples were left unpassivated. For these samples, MESFETs and Hall-effect devices were used to probe the irradiation effects. This will give us a more holistic perspective of the degradation modes of all H:diamond devices.

4.1 Proton Irradiation of Passivated H:diamond

Two H:diamond samples, which we denote here as AlOx:D1 and AlOx:D2, were passivated simultaneously with 25 nm of Al_2O_3 via ALD at a 250°C chamber pressure. This was a thermal deposition process, so the precursors used were trimethylaluminum (TMA) and H_2O. Prior to the oxide deposition, the two samples were annealed in the ALD chamber for 30 minutes in order to desorb the atmospheric molecules. This ensured that the Al_2O_3 film was the sole source of acceptors, since air-dopants have been shown to vary the sheet density over time. Once passivated, aluminum gates were patterned and evaporated as detailed in section 3.1.4.

The proton irradiation was conducted in the Tandem Accelerator at the Ion Beam Materials Laboratory at Los Alamos National Laboratory. A TiH_2 cathode was used to accelerate a beam

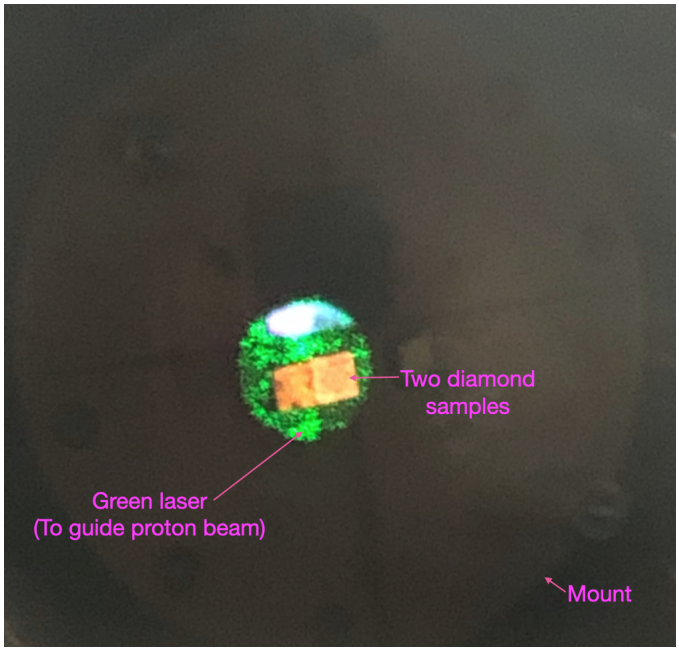

Figure 4.2: Diamond samples scintillating as they are being exposed to a proton beam. The green circle is a laser used to guide the user of the proton beam location.

of 2 MeV protons at the diamond samples in an ultra-high vacuum chamber. A proton flux approximating 1.43×10^{12} $cm^{-2}s^{-1}$ was exposed to AlOx:D1 and AlOx:D2 for 34 s and 70 s, respectively. The integral fluence was thus 0.5 and 1 $\times 10^{14}$ protons/cm^2. If we use the following parameters, we can extract the proton dose in Mrad: the mass density of Al_2O_3 (3.04 g/cm^3 for ALD at 250°C [88]), the electronic stopping power of 2 MeV protons in Al_2O_3 (35 eV/nm as calculated using SRIM [87]), and the aforementioned fluences. The conversion expression to rad units is given by (Fluence [cm^{-2}])×(Ionization rate [J/cm]) / (Mass Density [kg/cm^3]). The doses are thus 0.95 and 1.9 Mrad for 0.5 and 1 $\times 10^{14}$ protons/cm^2, respectively. The picture in Fig. 4.2 shows the samples scintillating as they are being exposed to the proton beam.

Prior to the proton-irradiation, the MISFETs and MISCAPs on the samples were characterized using a B1500 semiconductor parameter analyzer. This included current-voltage and capacitance-voltage measurements. Moreover, the Hall-effect devices were used to extract the hole sheet density and hole mobility. The same measurements were performed after the irradiation exposure. The analysis that follows is on the observed irradiation effects based on these measurements.

4.1.1 MISFET and MISCAP Measurements Pre/Post-Irradiation

IV Measurements

Note that for all plots in this chapter, black and red lines/data points refer to the pre- and post-irradiated measurements, respectively. The ID-VD measurements of the samples pre/post irradiation are shown in Fig. 4.3. These results demonstrate a clear degradation in the saturation drain current post-irradiation exposure. The degradation continues with higher proton fluences. The source of this degradation is primarily in the hole mobility reduction, caused by an increase in scattering induced by band distortions along the 2D hole well. The source of these distortions arise from the Coulombic interactions with the negatively-charged states in the Al_2O_3, which, as we shall see, increase post-irradiation. Moreover, we will later discuss how these distortions may also arise from the degradation of the C-H dipoles.

The ID-VG measurements are shown in Fig. 4.4. This figure demonstrated both a degradation of the drain current and a shift in the threshold voltage. Therefore, one degradation mechanism is a total ionizing dose (TID) effect of the oxide. Specifically, a positive shift in the threshold voltage indicates a negative charge build-up in the oxide. This has been observed in literature for proton doses on Al_2O_3. In Ref. [89], for example, thermal ALD Al_2O_3 exhibited a negative charge build-up for proton doses exceeding 500 krad. Ref. [90] also showed a similar effect but

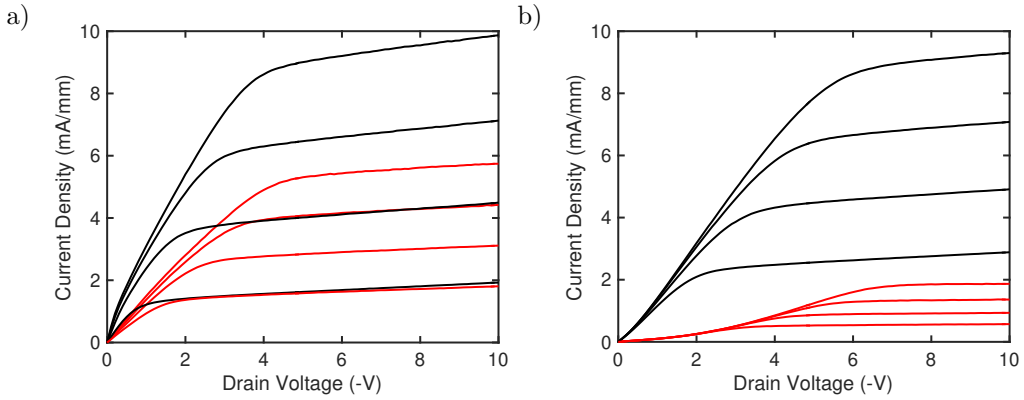

Figure 4.3: ID-VD measurements on the MISFETs of pre/post irradiated samples (black/red line). (a) AlOx:D1, exposed to 0.5 $\times 10^{14}$ protons/cm^2 and (b) AlOx:D2, exposed to 1 $\times 10^{14}$ protons/cm^2. These drain current was measured for gate voltages ranging from -0.5 to -3.5 V, in increments of -1 V.

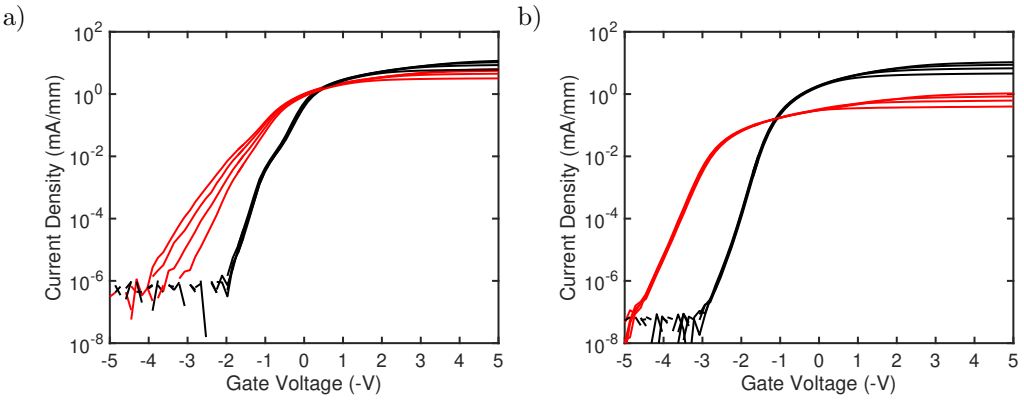

Figure 4.4: ID-VG measurements on the MISFETs of pre/post irradiated samples (black/red line). (a) AlOx:D1, exposed to 0.5 $\times 10^{14}$ protons/cm^2 and (b) AlOx:D2, exposed to 1 $\times 10^{14}$ protons/cm^2. A positive threshold voltage is observed, totaling (a) $\Delta V_{th} \approx 0.55$ V and (b) $\Delta V_{th} \approx 2$ V. This is indicative of a negative charge build-up post-irradiation.

for plasma ALD and for proton doses below 533 krad. Finally, the measured leakage current post-irradiation was negligible.

CV Measurements

To further explore the negative charge build-up in the oxide, we conducted CV measurements. The results are shown in Fig. 4.5. As discussed in section 3.3, the flatband voltage was extracted using the second derivative method (i.e., $d^2C(V)/dV^2 \approx 0$ when $V=V_{FB}$ [76]). Post-irradiation, the flatband voltage shift ΔV_{FB} was 0.65 and 1.45 V for samples AlOx:D1 and D2, respectively. This is once again indicative of a negative charge build-up in the oxide bulk, which (using Eq. (3.1)) is estimated to be 1.05×10^{12} and 2.35×10^{12} cm^{-2}, respectively. Moreover, we can gain insight on the trapping behavior at (or near) the Al_2O_3/H:diamond interface by measuring the hysteresis behavior. From Fig. 4.5, we can observe a counter-clockwise hysteresis behavior denoted as V_H (as a *p*-type device, the sweeping was performed from positive to negative V_G). For both samples, the hysteresis pre-irradiation was 80 mV. Post-irradiation, the hysteresis for samples AlOx:D1 and D2 increased to 210 and 220 mV, respectively. Interestingly, this increase was almost identical for both doses. This may indicate that the trap densities at (or near) the Al_2O_3/H:diamond interface increase and remain constant after a particular dose. Alternatively, the negative charge build-up can facilitate the tunneling of holes into traps that are deeper in the oxide, which would thus enhance the hysteresis.

The irradiated samples AlOx:D1 and D2 contained five different MISCAPs each. The ΔV_{FB} and ΔV_H were taken for each device and plotted in Fig. 4.6. Although the flatband voltage shift has a moderately large range for the higher fluence, these statistics give us a more conclusive interpretation of the degradation effects discussed above. That is, ΔV_{FB} increases with proton dose accumulation due to a negative charge build-up in the oxide. Moreover, the increase in ΔV_H post-irradiation indicates a mild increase in active trap densities at (or near) the oxide/diamond interface. However, ΔV_H yield similar average values for both doses, although the variance is larger across different MISCAPs in the AlOx:D2 sample.

To gain further insight into how this build-up of negative charge influences the properties of the 2DHG, Hall-effect measurements were conducted.

4.1.2 Hall-effect Measurements

Hall-effect devices were fabricated on samples AlOx:D1 and D2 in order to gain further insight as to how the conduction properties of the 2DHG are influenced with radiation dose. Shown in Table 4.1 are the mobility values for each sample. We observe a decrease in the hole mobility,

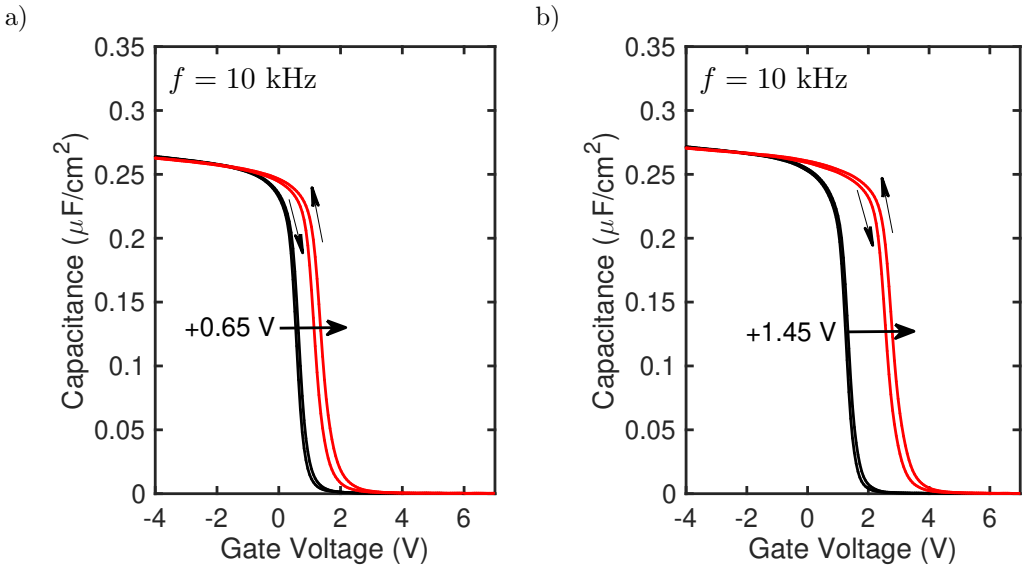

Figure 4.5: CV measurements on the MISCAPs of pre/post irradiated samples (black/red line) (a) AlOx:D1 and (b) AlOx:D2. A positive shift in the flatband voltage is observed, totaling (a) $\Delta V_{FB} \approx 0.65$ V and (b) $\Delta V_{FB} \approx 1.45$ V. As in the case of the IDVG measurements in the MISFETs, this is indicative of a negative charge build-up post-irradiation. Using Eq. (3.1) this negative charge density accumulation is estimated to be (a) 1.05×10^{12} cm^{-2} and (b) 2.35×10^{12} cm^{-2}.

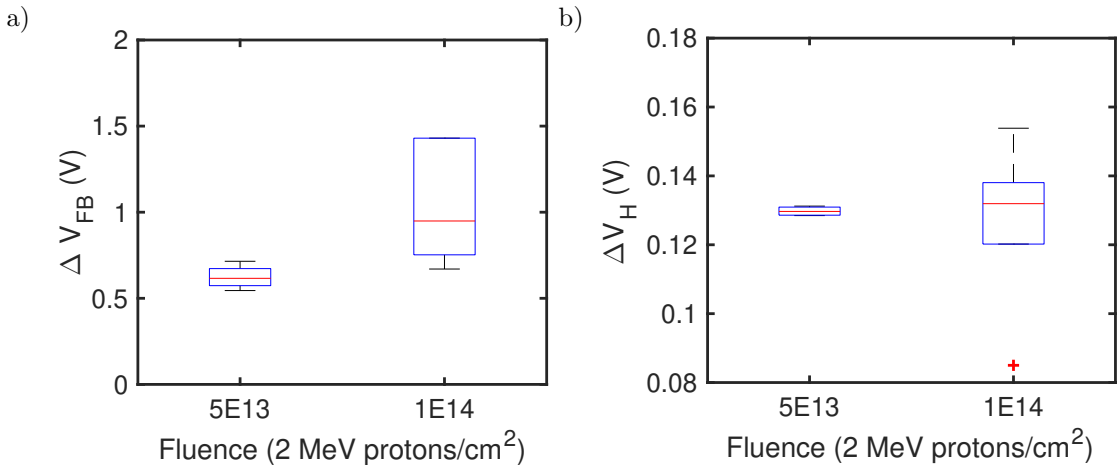

Figure 4.6: (a) Flatband voltage shift and (b) hysteresis increase extracted from five MISCAPs on samples AlOx:D1 and AlOx:D2

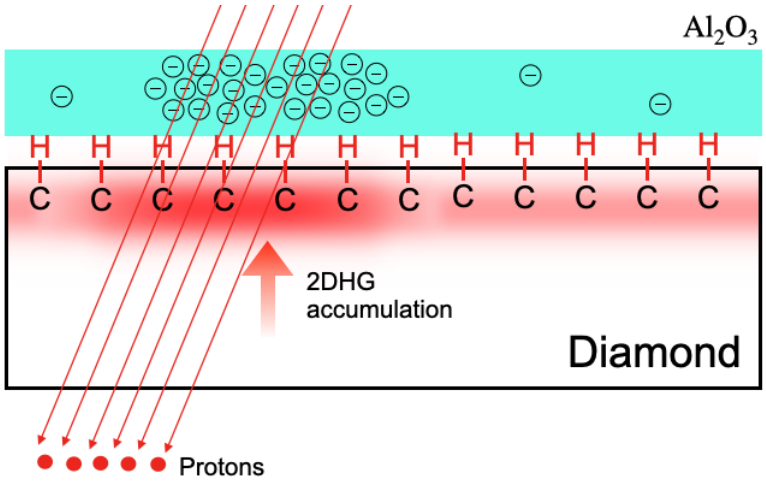

Figure 4.7: Schematic demonstrating the accumulation of holes due to the negative charge build-up in the Al_2O_3.

changing by -29.5% and -35.6% for AlOx:D1 and D2, respectively. This is likely due to enhanced remote impurity scattering induced from the negative charge build-up in the oxide, as well as an alteration of the C-H uniformity. This can be interpreted as an enhanced SI scattering, both for types (i) and (ii) (Eq. (A.6)). The result would therefore explain the saturation degradation observed in Fig. 4.3.

With regards to the hole sheet density, we observe that it increases with proton dose, as shown in Table 4.2. This is a direct consequence of the negative charge build-up as a function of dose, just as we have observed from the CV measurements. Effectively, the 2DHG is further accumulated after irradiation, which manifests in the Hall-effect measurements as a higher sheet density. This mechanism is shown schematically in Fig. 4.7. In addition, the irradiation may have increased the concentration of O_i and Al_v sites, which are believed to act as acceptors, as discussed in Chapter 3. This may contribute to the greater 2DHG concentration.

Interestingly, the hole mobility appears to degrade at a higher rate than the increase in hole sheet density. It may be the case that other scattering mechanisms are being exacerbated by the ionizing effects of the penetrating protons. Unfortunately, it is difficult to decouple the mobility limitations as induced by a degraded oxide from other limitations that are intrinsic

Table 4.1: Hall-effect mobility values for samples AlOx:D1 and AlOx:D2 pre/post irradiation.

Substrate	Fluence (H+/cm^2)	Pre-Irrad. μ_H (cm^2/(Vs))	Post-Irrad. μ_H (cm^2/(Vs))	% Change
AlOx:D1	0.5×10^{14}	48.5	34.2	-29.5
AlOx:D2	1×10^{14}	49.7	32.0	-35.6

Table 4.2: Hall-effect sheet density values for samples AlOx:D1 and AlOx:D2 pre/post irradiation.

Substrate	Fluence ($H+/cm^2$)	Pre-Irrad. n_{2D} (cm^{-2})	Post-Irrad. n_{2D} (cm^{-2})	% Change
AlOx:D1	0.5×10^{14}	1.51×10^{12}	1.81×10^{12}	+19.9
AlOx:D2	1×10^{14}	3.4×10^{12}	4.36×10^{12}	+28.2

to the H:diamond structure. We therefore dig deeper in our analysis by experimenting with irradiated H:diamond samples that were left unpassivated.

4.2 Proton Irradiation of Unpassivated H:diamond

Similar to the passivated samples, two air-doped and unpassivated H:diamond samples (denoted as Air:D1 and Air:D2) were proton-irradiated. Samples Air:D1 and D2 were also irradiated with 2 MeV protons at 0.5×10^{14} and 1×10^{14} cm^{-2}. Thus, the oxide charging effects (as induced via TID) on the degraded mobility is isolated. At present, the only known study of irradiated H:diamond surfaces is from Verona *et. al.*. However, this was for neutron irradiation, and negligible degradation was observed. Unlike neutrons, penetrating protons release energy in the form of ionization due to its charge, as shown in Fig. 4.1. Moreover, we know that the properties of the *p*-type surface conduction is dependent on the formation and stability of C-H surface dipoles. Since the ionization rate of a 2 MeV proton in diamond is 5 eV/Å near the surface (or about 18 eV/a_c, where a_c is diamond's lattice constant), it can be deduced that the penetrating protons can deposit enough energy to dissociate the C-H bonds. If so, this would have significant implications on the general stability of H:diamond devices (passivated or unpassivated) in environments rich with charged radiation particles.

4.2.1 MESFET Measurements Pre/Post-Irradiation

Shown in Fig. 4.8 are ID-VD measurements of the Air:D1 and D2 samples. We can once again observe a degradation in the drain current, which worsens with proton dose. However, this degradation rate is not as severe as the passivated samples in Fig. 4.3, likely owing to the absence of an enhanced scattering mechanism associated with the negative charge build-up in the oxides. However, the saturation current for the unpassivated devices still declines post-irradiation, which indicates another scattering mechanism whose rate increases with proton dose. This degradation is further supported in Fig. 4.9, where the ID-VD was measured for ten MESFETs on each sample. We can see that the percent degradation of $I_{D,SAT}$ approximately doubles with the proton fluence. It is thus conclusive that the ionization as induced by the energetic protons has

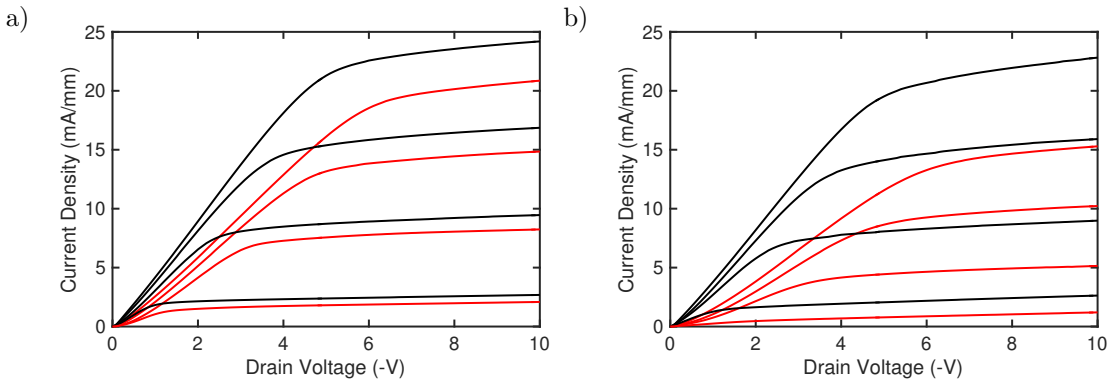

Figure 4.8: ID-VD measurements on the MESFETs of the pre/post irradiated (black/red line) (a) Air:D1, exposed to 0.5×10^{14} protons/cm^2, and (b) Air:D2, exposed to 1×10^{14} protons/cm^2.

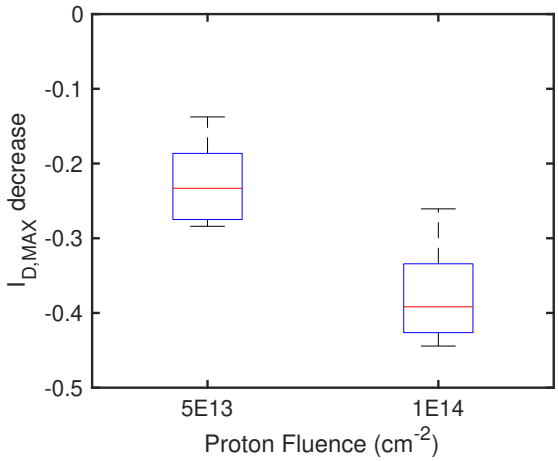

Figure 4.9: $I_{D,SAT}$ decrease of MESFETs on pre/post-irradiated Air:D1 and Air:D2.

significant degradation effects on the electrical properties of H:diamond. However, to gain insight on the exact mechanisms degrading these properties, we turn to Hall-effect measurements.

4.2.2 Hall-effect Measurements

Hall-effect devices were also fabricated on Air:D1 and D2. This gives us the means to extract the hole mobility and sheet density. Moreover, we perform Hall-effect measurements from 300 to 70 K. The measurements were taken from RT to low temperatures, and back up to RT, and negligible hysteresis was observed. As we shall see, this provides us with the information necessary to infer the mechanisms responsible for this degradation.

Shown in Fig. 4.10(a-b) and (c-d) are the Hall-effect measurements for samples Air:D1 and D2, respectively. Note the room temperature measurement, which is the first data point on each plot.

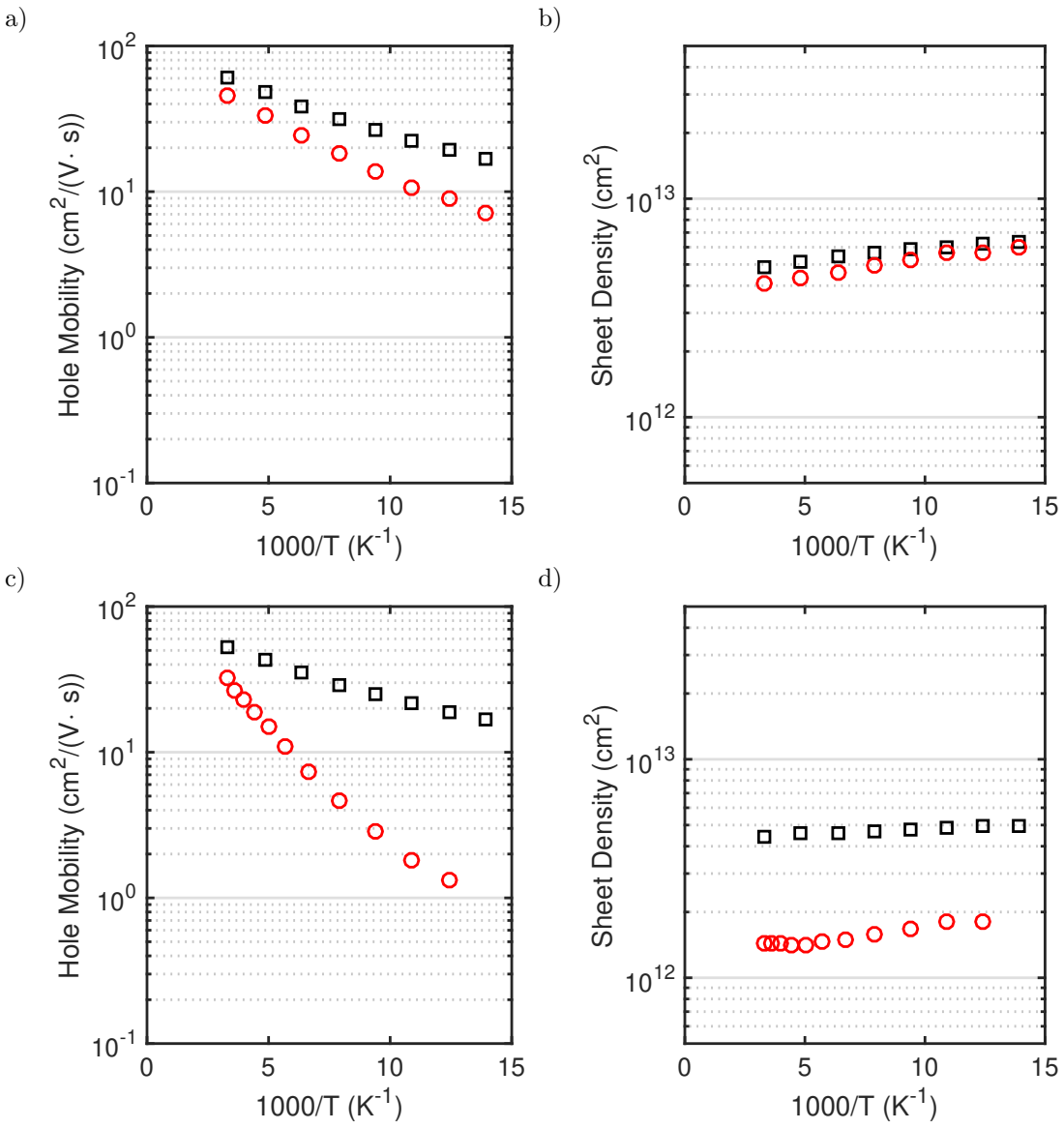

Figure 4.10: Hall-effect measurements of pre/post irradiation (black/red data points) of (a,b) sample Air:D1 and samples Air:D2 (a,b)

Here we see a notable degradation of the mobility for both samples, from 60.5 to 45.4 $cm^2/(V\text{-}s)$ for Air:D1, and from 53.2 to 32.7 $cm^2/(V\text{-}s)$ for Air:D2. There is thus a scattering mechanism that is enhanced post-irradiation. At least two plausible mechanisms can explain this observation. First, the ionization of the penetrating protons may impart enough energy to create vacancies and interstitials throughout the diamond surface. Second, the ionization may impart enough energy to dissociate the C-H dipoles. Both of these degradation mechanisms would create band distortions which would, in turn, scatter the conducting holes and lower their mobility.

We believe that the first of these explanations (creation of lattice vacancies and interstitials) is unlikely, given the electronic and nuclear stopping power functions for a 2 MeV proton in diamond. Using SRIM, we can simulate both the ionization rate (e.g., Fig. 4.1), as well as the vacancy production rate (in units vacancies per nm), for any charged ion and target material. Near the surface, each 2 MeV proton produces approximately 1×10^{-4} vacancies/nm. That is, a proton must penetrate through 10 micrometers before a single vacancy is produced. Fortunately, an experimental study by Manfredotti *et. al.* supports this reasoning [91]. These authors also exposed 2 MeV protons to single crystal diamond samples (which were purchased from the same manufacturer that supplied the samples for this study). During and after proton exposure, Manfredotti *et. al.* performed luminescence measurements and found that the peak for the H3 center (regarded as the center for vacancies and interstitials in diamond, and is commonly enhanced by irradiation [92–94]) increases marginally after a fluence of 9×10^{14} cm^{-2}. This is $9\times$ the maximum fluence in this study. Moreover, these luminescence techniques collect light from a depth of multiple microns. Since the induced lattice damage increases with the depth of the ion, this means that the signal for the H3 center would be even weaker near the superficial regions where the 2DHG exists. For this reason, it is doubtful that the lattice defects are the primary reason behind the degraded mobility measured in samples Air:D1 and D2.

However, ionization of the surface may impart sufficient energy to dissociate the C-H bonds, which we know are necessary for the formation of the 2DHG. Other studies on the irradiation of H:diamond with neutrons [86], as well as gamma [95], show no evidence of degradation. This is likely because these uncharged radiation species do not emit a trail of ionization energy as charged particles do. There have been studies of keV-electrons dissociating the C-H bonds, however [96]. Moreover, the charged particle radiation effects on surfaces and interfaces have been studied extensively for a wide variety of materials. For example, it is well established that the adhesion of metal/ceramic interfaces increase significantly after irradiating with MeV ions [97, 98], which is attributed to the interactions caused by ionization. C-H bonds have also been shown to dissociate upon MeV irradiation in a multitude of hydrocarbon-rich materials [99]. In general, in multiple

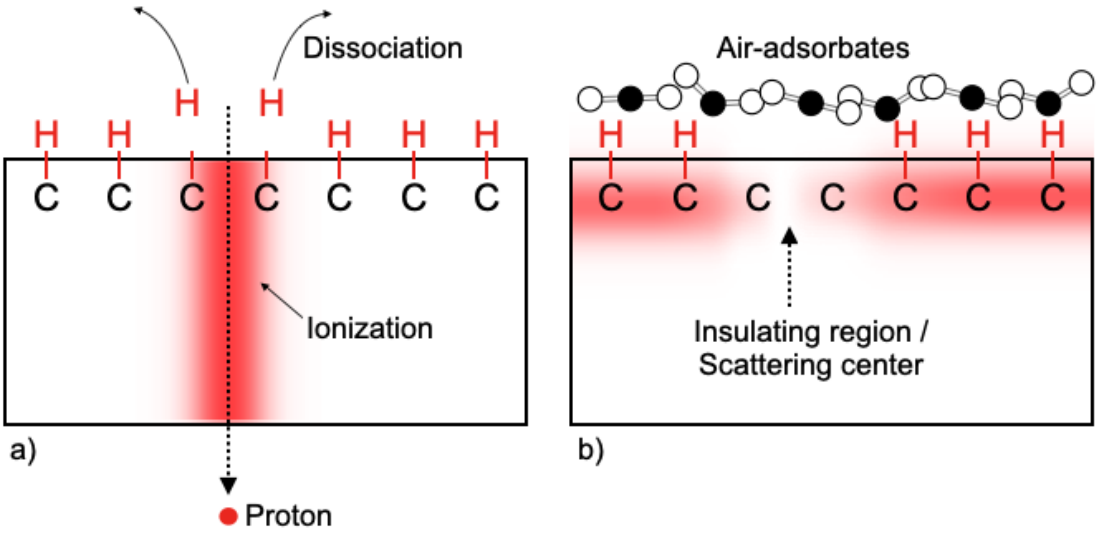

Figure 4.11: Schematic demonstrating the dissociation of C-H bonds resulting from proton ionization. (a) Proton irradiation of H:diamond in the vacuum chamber, and (b) the induced 2DHG after air exposure. Any dissociation of the C-H surface would degrade the 2DHG electrical properties.

contexts involving MeV-ion irradiation, the ionization-induced desorption of surface molecules is widely inferred to explain various phenomena [100, 101].

As we discussed in the previous chapter, we already hypothesized that long-range potential fluctuations act as scattering centers, which may in turn arise from incomplete hydrogen termination. Along this line of reasoning, should the ionization induced by the protons dissociate the C-H bonds, more scattering centers would be produced along the 2D hole well, which would explain the degraded mobility and saturation current. This is shown schematically in Fig. 4.11.

With respect to the irradiation effects on the 2DHG sheet density, this is shown in Figs 4.10(b,d). We see from both samples that the sheet density degrades. For the sample Air:D1, we observe that the degradation is small, yet noticeable, from 4.86 to 4.06 $\times 10^{12}$ cm^{-2}, which is a 16.5% decrease. On the other hand, the sheet density degradation for Air:D2 is much more, from 4.46 to 1.45 $\times 10^{12}$ cm^{-2}, which is a 67.0% decrease. The general trend here is that the 2DHG density degrades with fluence, which is presumably caused by the dissociated C-H bonds. As discussed in the previous chapter, surface orientations with higher C-H densities exhibit a higher 2DHG density [56]. We can therefore infer that decreasing the effective C-H density by dissociating the hydrogen would, in turn, degrade the 2DHG density. It is worth noting, however, that the large drop in sheet density between samples Air:D1 and D2 is unexpected, given that the dose

for Air:D2 is only double that of Air:D1. Since these are separate samples, there may be intricacies of the surface that explain such a large drop. Alternatively, there may be a degradation mechanism with a threshold between both fluences, which could only be interpolated with more fluence data points between 0.5 and 1×10^{14} cm^2.

4.2.3 Effective Medium Theory

As discussed in the previous chapter, the Hall-effect measurements as a function of temperature exhibit three important behaviors of the 2DHG properties. First, the hole sheet density is relatively constant across temperatures. Second, the hole mobility and conductivity are thermally activated, starting from their highest value at RT and declining rapidly at low temperatures. Third, the activation energy increases as the hole sheet density decreases. The transport properties of 2D carriers in distorted potential wells is a subject that has been studied in many technologies (e.g., MOSFET inversion layers with defective or rough oxides). The Anderson mobility edge and the Arnold long-range fluctuation model are two examples that describe the nature of these potential wells [62, 102]. As discussed in the last chapter, the 2DHG in this work follows the observations made by Arnold. In qualifying the conduction dynamics, Arnold treats the carriers semiclassically as the percolation around, scattering from, and thermal emission over random potential barriers.

With this in mind, the results of the proton-irradiated H:diamond raise an obvious question: Are the average density and energy barrier heights of these "random potential barriers" along the 2DHG channel being affected by the penetrating protons, and if so to what degree? We can attempt to answer this question by invoking the effective medium theory (EMT). Using EMT we define the average density of barriers as an insulating fraction ξ of the active region. That is, ξ and (1-ξ) are the fraction of the mixed insulating and conductive regions, respectively. Further, the average potential barrier height E_b defines the energy that holes must thermally gain to "activate" and conduct through the insulating regions. The EMT expression for the sheet conductivity in this mixed system is thus [62],

$$\sigma(T) = \frac{1}{2}\left(1-2\xi\right)\left(\sigma_1 - \sigma_2(T)\right) + \left[\frac{1}{4}\left(1-2\xi\right)^2\left(\sigma_1 - \sigma_2(T)\right)^2 + \sigma_1\sigma_2(T)\right]^{1/2}, \qquad (4.1)$$

where σ_1 and $\sigma_2(T)$ are the average conductivities of the metallic and insulating regions, respectively. The activation behavior stems directly from $\sigma_2(T)$, which is approximated as,

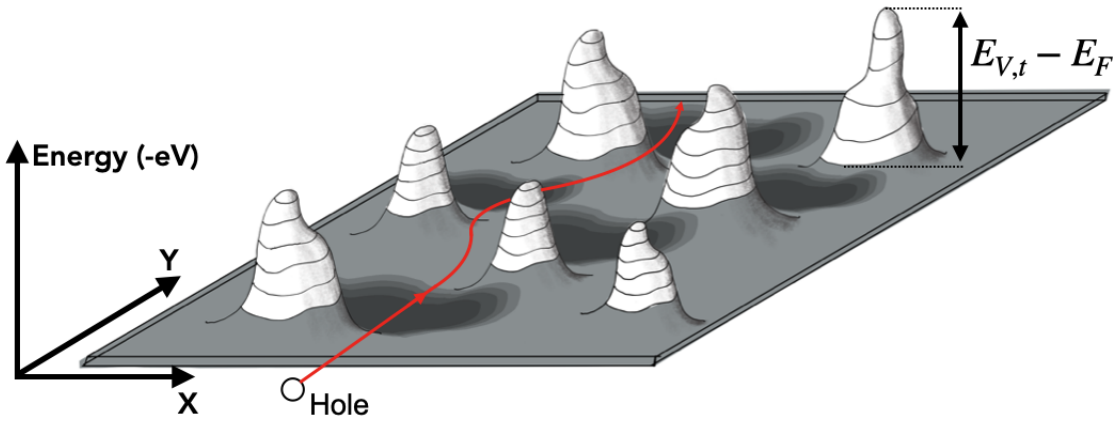

Figure 4.12: Percolating holes along the 2D valence band well.

$$\sigma_2(T) = \sigma_1 \exp\left(E_b/k_b T\right), \tag{4.2}$$

where k_b is Boltzmann's constant and T is temperature. Note that in reality, the barrier heights along the potential well take on a Gaussian distribution, as opposed to a single value E_b, as shown schematically in Fig. 4.12. We instead use Eq. (4.2) as an approximation and define the average barrier value,

$$E_b = \langle E_{V,t} - E_F \rangle, \text{where } E_F \geq E_{V,t} \tag{4.3}$$

where $E_{V,t}$ is the top of the barrier and E_F is the Fermi energy. Therefore, we represent the activation energy as a global average of the barrier heights.

Fig. 4.13(a) and (b) show two distinct Hall-effect devices on Air:D1. Likewise for Fig. 4.14 on Air:D2. The barrier height averages and insulation fractions are determined via fitting to the experimental data points, as shown by the solid lines. These fitting values are presented in

Table 4.3: Effective Medium Theory parameters

Substrate (Device)	Fluence (cm^{-2})	Pre-Irrad. E_b (meV)	Post-Irrad. E_b (meV)	Pre-Irrad. ξ	Post-Irrad. ξ
Air:D1 (1)	0.5×10^{14}	27	30	0.43	0.455
Air:D1 (2)	0.5×10^{14}	23	30	0.42	0.465
Air:D2 (1)	1.0×10^{14}	27	65	0.39	0.52
Air:D2 (2)	1.0×10^{14}	29	45	0.40	0.48

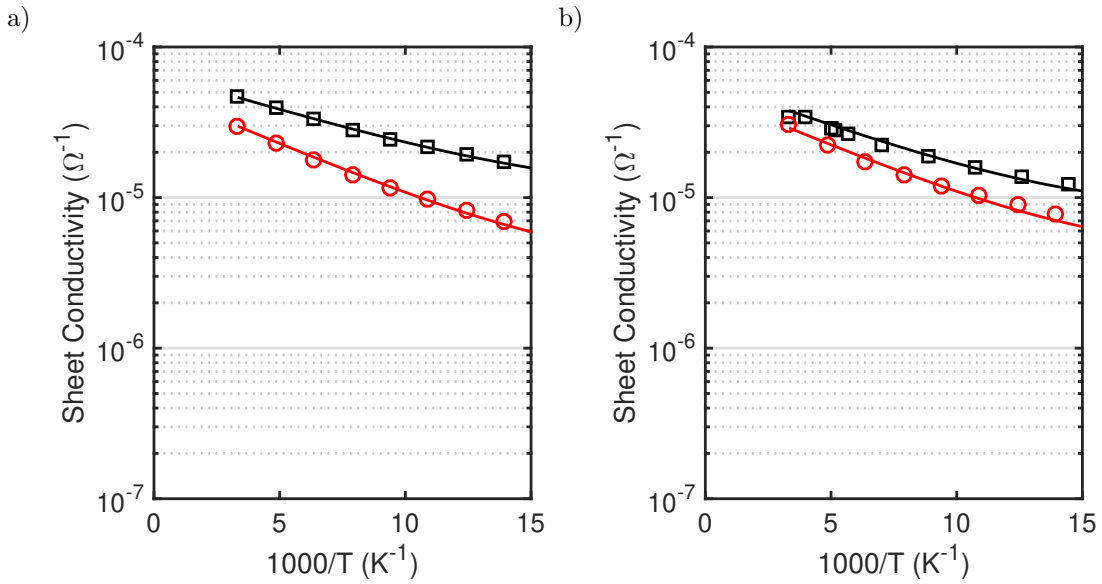

Figure 4.13: Sheet conductivity of sample Air:D1 pre/post irradiation (black/red data) for (a) Device 1 and (b) Device 2. The function $\sigma(T)$ of Eq.(4.1) is fitted to the data points using parameters presented in Table 4.3 for Air:D1.

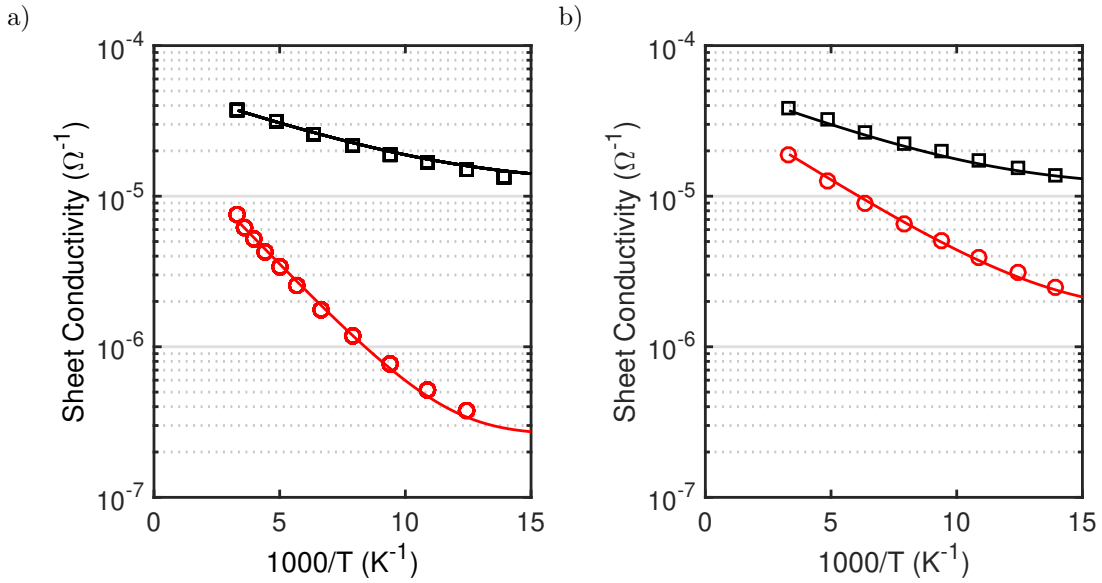

Figure 4.14: Sheet conductivity of sample Air:D2 pre/post irradiation (black/red data) for (a) Device 1 and (b) Device 2. The function $\sigma(T)$ of Eq.(4.1) is fitted to the data points using parameters presented in Table 4.3 for Air:D2.

Table 4.3. For sample Air:D1, the activation energies for both samples increased moderately post-irradiation. This is partially explained by an increase of the average barrier height, presumably stemming from the surface effects from the proton ionization. For sample Air:D2, the activation energies once again increase post-irradiation, but more significantly so. This barrier height increase stems mostly from the drop in the hole sheet density, which, as discussed earlier, strongly determines the activation behavior of the mobility (and therefore the conductivity). This cannot be said about Air:D1, since the sheet density remains rather identical pre/post-irradiation. Thus, we can infer that although the activation behavior is most sensitive to the hole sheet density, the irradiated sample has some, though mild, impact on the average barrier height.

The insulation fraction ξ also appears to increase with irradiation. For sample Air:D1, both devices increase moderately post-irradiation, and more-so in sample Air:D2. The average delta of insulating fraction $\Delta\xi$ is 3.5% and 10.5% samples Air:D1 and D2, respectively. This degree of impact is reasonable if we consider the C-atom density on the surface of (001)-2x1 reconstructed diamond, which is 1.57×10^{15} cm^{-2} [56]. Thus, 3.5% and 10.5% of the surface layer corresponds to 0.55×10^{14} and 1.65×10^{14} cm^{-2} surface atoms, respectively. These values are close to the fluence levels, corresponding to $\sim$1 to 1.65 C-H atoms per penetrating proton. Therefore, to the extent that dissociated C-H atoms are indeed a consequence of the irradiation, the degrading ionization effects do not extend far from the proton's track center. Under these assumptions, a proton fluence on the order of 10^{15} cm^{-2} would dissociate the entire C-H surface. Fortunately, the integral fluence of MeV-protons in low-Earth orbit (LEO) environments is on the order of 10^{9} cm^{-2} for multi-year missions [103]. Thus, at least for LEO environments, it is unreasonable to anticipate the degradation levels observed in this work.

It is worth noting that there are complicated interactions that are beyond the scope of the approximations made hereto, including the screening of and tunneling through the insulating barriers. For example, a small barrier may be screened effectively by the 2D hole gas, which would, in effect, reduce the activation energy. Moreover, at low temperatures, where the Fermi energy range is narrow and conduction over barriers is limited, holes may still tunnel through them, which is especially important at low Fermi energies (i.e., low sheet densities). This tunneling phenomenon discussed in more detail by Arnold [62].

4.3 Chapter Summary

In this chapter, we discussed the work of irradiating four single-crystal diamond samples, two of which were passivated with Al_2O_3, and the other two left unpassivated. Several devices were

fabricated and measured prior to irradiation, which include MISFETs, MISCAPs, MESFETs and Hall-effect devices. The samples were irradiated with 2 MeV protons at two fluences, 0.5×10^{14} and 1×10^{14} cm^{-2}. In order to decouple the degradation that is intrinsic to the H:diamond from the degradation of the passivation layer, the characteristics of MESFETs and Hall-effect devices of unpassivated H:diamond samples were exposed and measured.

It was determined that the Al_2O_3 were negatively charged post-irradiation, which consequently degraded the hole mobility, but also increased the sheet density via electrostatic attraction. The net result was a substantial decrease in the drain saturation currents, and shifts in the threshold and flatband voltages. It was also determined that the hole mobility and sheet density drop on the unpassivated H:diamond samples. The net result was also a decrease in the drain saturation current. Since MeV-protons exhibit negligible nuclear scattering, and deposit their energy entirely via ionization, we suspect that the degraded hole mobility is caused via enhanced scattering off insulating barrier centers throughout the 2D hole well. Effective medium theory was used to infer the height of these barriers and the surface fraction that they occupy. Together, this study provides a holistic understanding of the degradation mechanisms of all H:diamond devices, passivated or not.

Although significant degradation was observed in H:diamond surfaces, we estimate that proton fluences on the order of 10^{15} cm^{-2} are required to dissociate the entire C-H surface. Fortunately, the integral fluence of MeV-protons in LEO environments is on the order of 10^{9} cm^{-2} for multi-year missions [103]. This difference is many orders of magnitude. Thus, H:diamond technology remains promising for space environment applications, given that it is unreasonable to anticipate degradation levels observed for 10^{14} cm^{-2} fluences. Moreover, 2DHGs are promising for low temperature applications. For example, the ambitious endeavours by space agencies to explore space environments (e.g., Europa) have drawn attraction toward electronics that can sustain low temperatures [104]. On this front, 2DHGs channels are the most promising type of diamond-based technologies, owing to their metallic nature (i.e., the sheet density is stable at low temperatures). Bulk-doped diamond, on the other hand, suffers from carrier freeze-out of dopants [105].

Chapter 5

Radiation-Induced Annealing in Wide Band-gap Materials

The resurgence of space exploration has called for electronic devices and materials capable of withstanding irradiation-rich environments. High particle radiation induces several measurable phenomena in semiconductor devices used in space-born systems. The first phenomenon is transient in nature, also known as a single event effect (SEE), which typically occurs when a radiation species penetrates sensitive regions of a device. The second is via material degradation due to long-term radiation exposure (e.g. total ionization dose), which slowly deteriorates the electrical behavior of the device. These two phenomena can ultimately lead to catastrophic mission failure due to device instability or unrecoverable damage.

Silicon carbide, in comparison to silicon, has shown impressive operational stability under high temperature and radiation-rich environments [106]. But, in order to fully leverage the properties of SiC, predicting its behavior under such extreme conditions is required – a feat that necessitates a profound understanding of a device's response to ion strikes. For example, it has been shown that a penetrating ion induces transient lattice heating (i.e., thermal spikes), which may exceed the melting/sublimation point of the host material [107]. This especially occurs during swift heavy ion (SHI) radiation events, where inelastic interactions with the host material can locally produce "hot electrons" with temperatures on the order of 10^4 K. Empirical data and models have shown that such electron temperatures couple to the atomic system to produce exceedingly high lattice temperatures [108]. This phenomenon alone is a cause for concern for operational stability of electronics, as it can produce single event transients that irreversibly modify the electrical properties [109].

For SiC in particular, annealing and recrystallization is a much more reported phenomenon for SHI exposure [110, 111]. Multiple studies have demonstrated SHI-induced annealing in SiC for electronic energy depositions exceeding 10 keV/nm, and some as large as 33 keV/nm [110, 112]. Moreover, Zhang et al., reported a threshold value of 1.4 keV/nm, whereby defect annihilation in SiC was observed [111]. This low threshold value (which the authors termed the "intermediate regime" regime of ion types) is far more accessible to industrial accelerators and can be considered an avenue to develop low-temperature annealing techniques.

On the other hand, catastrophic failure was observed in SiC diode devices under high reverse biasing conditions [113–115], where it was predicted that high field conditions amplified the thermal transient event, which cascaded into a permanently damaged device. Although the ion species and field conditions considered in these references far exceed the conditions considered in this work, it nonetheless stresses the need to explore this relationship further. Thus, we expand upon the implications of ionization events near high fields (i.e., sensitive volumes), where the average energy of ionized electrons is dramatically increased and consequently results in enhanced phonon emission. Although the defect annihilation from ionization-induced heating has been documented for SiC, there is limited work studying these events in the context of high electric fields. This is particularly important for low-Z number ions, which are far more abundant in radiation environments [116] and more accessible to industrial accelerators.

In this study, we use molecular dynamics (MD) to simulate thermal spike events in SiC, which results in significant defect recovery. In particular, for the first time, we demonstrate how high background field strengths common in wide bandgap materials can augment the energy deposition of the radiation-induced thermal transient, and observe the degree to which defect recovery is enhanced. In the next section, we examine how the thermal spike profiles are calculated. In section 3, we discuss the Ensemble Monte Carlo (EMC) technique used to quantify the thermal energy density with varying electric fields. In section 4, we detail the MD technique used to determine its effects on defect recovery, and lastly we discuss our results in section 5 before the concluding remarks.

The work of this chapter can also be found in our published work [117].

5.1 Localized Thermal Transients Induced by Ionizing Particle Radiation

5.1.1 Thermal Spike Calculation

For decades, spatial profiles of thermal transients induced by single event effects have been thoroughly investigated using the inelastic thermal spike model (ITSM) [118]. We use this model herein, the results of which define the inputs of our EMC and MD methods that follow. The ITSM is based on coupled cylindrical heat transport equations, each representing the spatial and temporal evolution of the electron temperature, T_e, and atomic temperature, T_a. The heat transport equations are

$$C_e(T_e)\frac{\partial T_e}{\partial t} = \frac{1}{r}\frac{\partial}{\partial r}\left[rK_e(T_e)\frac{\partial T_e}{\partial r}\right] - g\cdot(T_e - T_a) + A(r,t) \tag{5.1}$$

and

$$C_a(T_a)\frac{\partial T_a}{\partial t} = \frac{1}{r}\frac{\partial}{\partial r}\left[rK_a(T_a)\frac{\partial T_a}{\partial r}\right] + g\cdot(T_e - T_a), \tag{5.2}$$

where the parameters C and K are the heat capacity and thermal conductivity, respectively, r is the radial distance from the track center, and t is time. The parameters K_a and C_a are a function of temperature and extracted from Ref. [119]. The term $g\cdot(T_e - T_a)$ is the electron-phonon interaction term that defines the coupling between the two subsystems. The coupling constant g was calculated from the relation $g = D_eC_e/\lambda^2$, where λ is the electron mean free path and is deduced from the 3C-SiC band-gap (~ 6 nm) [108]. The parameters D_e and C_e are the electron diffusivity and specific heat, respectively, and are taken to be constant ($C_e = 1$ J cm^{-3} K^{-1} and $D_e = 2$ cm^2 s^{-1}). This simplification is based on the premise that conductive electrons in insulators behave like electrons in metals [108]. The initial energy distribution of the electrons is $A(r,t)$ is the source term (i.e. ion strike) defining the energy density deposited to the electron subsystem. We calculate this function using TOPAS (TOol for PArticle Simulation), a user-friendly software interface that is built on the GEANT4 Monte-Carlo toolkit [120], although analytical approaches that accurately approximate MC methods are often used [108, 121].

5.2 Enhanced Recovery-effect using Strong Electric Fields

5.2.1 Field-dependent Hot Electron Energy Dissipation

One main advantage of wide bandgap materials in electronic device design is their high breakdown electric field, which is on the order of ~ 1 MV/cm for 3C-SiC (and several fold higher for 4H-SiC and GaN). Although these properties are advantageous for high power device applications, the much higher electric fields enhance the sensitivity of the device and thus exacerbate any SEEs that may occur when operating in radiation environments [113]. Specifically, in the event of an ion strike, the center of a cylindrical volume around the particle track becomes saturated with high-energy electrons, which subsequently relax by interacting inelastically with the lattice (i.e., in the form of phonons). In this work, our proposition is that this heating phenomenon is far more pronounced near field-sensitive volumes (e.g. Schottky interfaces at large biases, or channel-drain regions in field-effect transistors), where the full relaxation of energetic electrons is prolonged by the energy gain from an applied field. Although the ion strike alone can induce sufficient heating to alter the crystal structure of the host material, such events can be far more pronounced near field-sensitive volumes.

It is widely understood that "hot electrons" deposit most of their energy to the atomic subsystem via electron-optical phonon scattering. In order to quantify the emission of optical phonons as a function of background electric fields, the EMC method is employed, which uses a well-documented algorithm described elsewhere [122, 123]. For this method, we assume that the electric field is oriented along the $\langle 111 \rangle$ direction of the 3C-SiC crystal so that we ignore the redistribution of carriers among equivalent band-structure valleys (as in Ref. [124]). This simplification allows us to use a single equivalent non-parabolic valley in our calculations, expressed by

$$E(1 + \alpha E) = \frac{\hbar^2 k^2}{2m_c} \tag{5.3}$$

where $\alpha = 0.323$ eV^{-1}. The density-of-state mass $m_d = 0.346m_0$ was used to determine scattering rates and $m_c = 0.313m_0$ was used for the equations of motion. For our purposes, we focus on the total energy deposited (in the form of optical phonons) as a function of background electric field. The scattering mechanisms considered here are acoustic, polar-optical and two non-polar optical interactions (zeroth-order and first-order). Due to the simulation times of interest

here (< 5 ps) and high electron energies, the thermal energy deposition is defined by the emitted optical phonons (defined by electron-optical phonon scattering events), which is comparably much higher than the emitted acoustic phonons. Empirically, optical phonons couple to acoustic phonons, which initiates heat transport [125]. However, this mechanism is ignored here since we are primarily interested in the initial conditions of the ion strike event and the subsequent energy deposited to the lattice (which is augmented by the electric field).

5.2.2 Ensemble Monte Carlo Simulations

The EMC simulation begins by initializing the energy distribution of 10,000 particles (representing electrons) such that the energy per unit length matches the electronic stopping power S_e, with a radial distribution approximating $A(r,t)$ from section 2. The total depth of the simulated particles was 500 nm. In the case of 50 MeV O+ in 3C-SiC, the net energy of the simulated particles is 1.60 keV/nm. During the EMC algorithm, a random number is drawn to determine the time of free flight for each particle. At the end of the free flight, a scattering operation may occur with a probability that is a function of the particle's energy. The particle's momentum after scattering (Eq. 3) is determined via the conservation of energy, $E'_k = E_k - \hbar\omega_{LO}$, which is the inelastic scattering process that defines the deposited thermal energy. Note that due to the stationary nature of an optical phonon, no dispersion is assumed. Thus, since heat transport is ignored and unnecessary during these time frames, the position of each particle (after scattering) is regarded as a quantum of the atomic thermal energy. The phonon energies have been set to 100 meV and 120 meV for nonpolar and polar-optical phonons, respectively [126]. The EMC simulation is run for 3 ps (well after steady-state is reached), after which the total energy of the emitted optical phonons is stored. Although phonon emission would continue past this simulation time (assuming high E_z), the energy density decreases substantially as the particles diffuse radially. The results are shown in Fig. 5.1 and Fig. 5.2. We observe in Fig. 5.2(a) that high energy carriers will continue emitting optical phonons at time scales several-fold higher than a typical energy relaxation time for hot electrons. By binning the system, we normalize using the 3C-SiC atomic density and plot the added thermal energy per atom (Fig. 5.2(b)). In other words, Fig. 5.2(b) plots the difference between the thermal energy per atom at non-zero and zero E_z, which can be expressed as $\langle k_B T \rangle(E_z) - \langle k_B T \rangle(E_z = 0)$. This process is repeated for multiple electric fields for 50 MeV O+ and 50 MeV Al+, the data of which is used in the MD simulations that follow. The parameters used in our EMC simulation are presented in Table 5.1, and the ions considered are presented in Table 5.2.

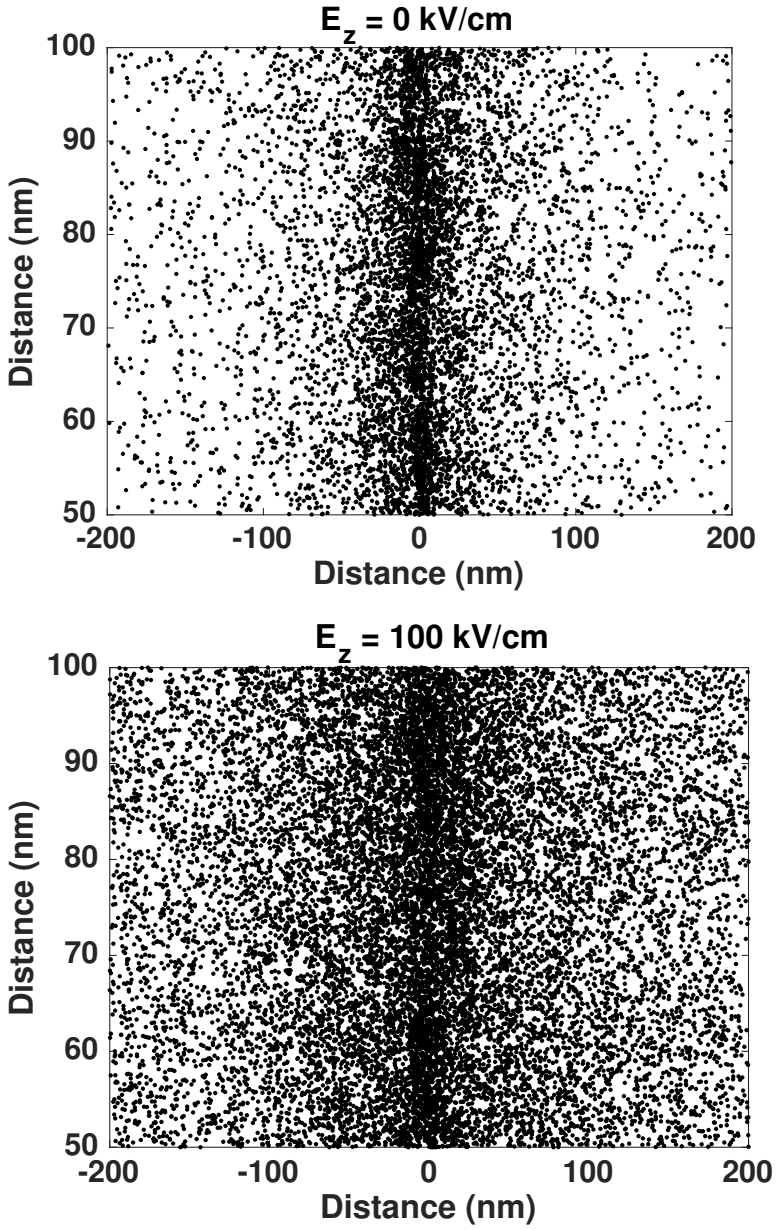

Figure 5.1: Illustration of optical phonon scattering positions in a 3C-SiC crystal as simulated by EMC. Images are snapshots at $t = 3$ ps. For contrast, only the phonons produced by 1% of particles are shown.

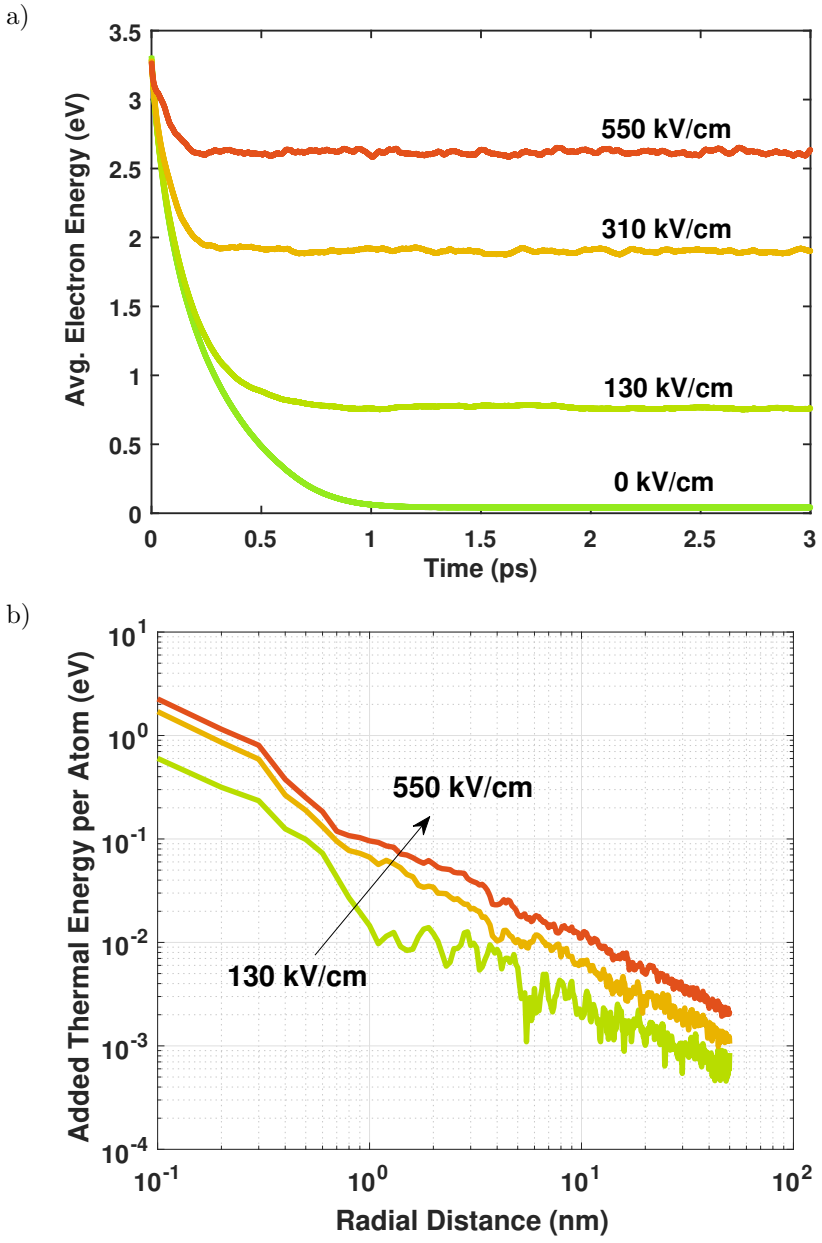

Figure 5.2: (a) Average electron energy at different electric fields, where $t = 0$ corresponds to the moment of a 50 MeV O+ strike. (b) Added thermal energy per atom as a result of a non-zero electric field at $t = 3$ ps (i.e. $\langle k_B T \rangle (E_z) - \langle k_B T \rangle (E_z = 0)$)

Table 5.1: EMC modeling parameters [126].

Parameter	Value
Bandgap (eV)	2.3
Nonparabolicity factor (eV^{-1})	0.323
Density (g/cm^3)	3.21
Acoustic deformation potential (eV)	16
Nonpolar optical phonon coupling:	
Zeroth-order (10^8 eV/cm)	9
First-order (eV)	5.6
Nonpolar optical phonon energy (meV)	100
Polar optical phonon energy (meV)	120
Low-frequency dielectric constant	9.7
High-frequency dielectric constant	6.5

Table 5.2: Ion specifications. The electronic stopping power S_e is calculated using SRIM [127].

	O+	Al+
Ion Energy (MeV)	50	50
Ion Specific Energy (MeV/u)	3.12	1.85
S_e (keV/nm)	1.60	4.0
$T_{a,max}(r = 0)$ (K)	850	1400

5.3 Molecular Dynamics Modeling

The ITSM temperature distribution $T_{a,max}(r)$, which is induced by the ion strike (as calculated in section 2), is subsequently imported into our molecular dynamics simulations, which we employ using the Large-Scale Atomic/Molecular Massively Parallel Simulator (LAMMPS) [128]. The function $T_{a,max}$ corresponds to the time when the thermal spike reaches its maximum temperature. The Si and C interactions are modeled by the hybrid Gao-Weber (GW)/ZBL potential [129], since it has previously been used to model defect annihilation [111, 130], recrystallization [131], and recovery due to swift heavy ions [112]. Hence, this potential is expected to accurately describe the damage production and recovery processes. The simulated 3C-SiC system was 36 $\times$ 36 $\times$ 6 nm^3 containing 768,000 atoms.

Prior to simulating the thermal spike event, defects were created by initializing the 3C-SiC system with thousands of randomly generated Frenkel pairs (FPs). Upon the generation of FPs, the system energy was minimized using a NPT ensemble for 100 ps, causing the generated defects to migrate to metastable positions and to bring the system to room temperature. This process was repeated until approximately 2% of the system was defective (by modifying the initial set of displaced atoms). To prevent divergence, a varying timestep was used, with a minimum / maximum timestep of 0.1 fs / 1 fs, respectively. The defects were defined using a built-in

Voronoi method in LAMMPS, where a polyhedral volume is defined around each atom in the pristine 3C-SiC. Thus, one atom per Voronoi volume implies a pristine crystal. The simulator identifies a vacancy if no atom is present in the volume, whereas an interstitial is identified if 2 or more atoms are present. Incidentally, the thermal dissipation properties of the lattice is expected to have a dependence on the lattice disorder. However, we ignore this dependence here since it has been demonstrated to have little effect on the defect recovery behavior [112].

With the defective 3C-SiC in thermal equilibrium, a thermal spike event was subsequently simulated. The system was defined to keep the number of atoms and volume constant while controlling the temperature through a 2 nm-thick Berendsen thermostat in the x-y boundaries, which acts as a thermal reservoir. The thermal spike was defined by binning the system into multiple cylindrical volumes so that the atoms in each bin could be separately operated on. The average kinetic energy of the atoms in each bin was defined such that the MD temperature profile best fitted $T_{a,max}(r)$ from the ITSM, as shown in Fig. 5.3 for the case of 50 MeV O+. The temperature profile is approximately at its maximum within the first picosecond of simulation, thus $t = 0.8$ ps was chosen for Fig. 5.3. To represent an increase in E_z, the EMC method was used to extract the added thermal energy per atom (Fig. 5.2(b)). This profile was subsequently used at the initialization of the MD simulation, where the kinetic energy of atoms inside the cylindrical bins was increased in accordance to the calculations from EMC. The thermal spike simulation was run for a total of 50 ps with a 0.2 fs timestep, after which the defect concentration was characterized (extending the simulation time for longer periods did not noticeably affect the lattice disorder). The result is plotted in Fig. 5.4 at $t = 0.8$ ps for up to 1000 kV/cm.

Although the GW potential has been demonstrated multiple times to model defect dynamics in MD, it is critical to question how our results relate to the activation energies associated with defect production and recovery. One study has demonstrated that close-range FP recombination barriers in GW can range between 0.22 eV and 1.6 eV [130], which was regarded as relatively low according to *ab initio* results from reference [132]. More generally, however, computational and experimental values obtained for recombination barriers for both silicon and carbon FPs vary, which is likely caused by inconsistent methods used in *ab initio* calculations [133]. For this reason, we believe it is appropriate to simulate a thermal spike event using the environment-dependent interatomic potential (EDIP), which exhibits activation energies higher than those of GW, while accurately describing bulk properties and point defects of 3C-SiC [134]. However, a detailed comparison between these two MD potentials is beyond the scope of this paper.

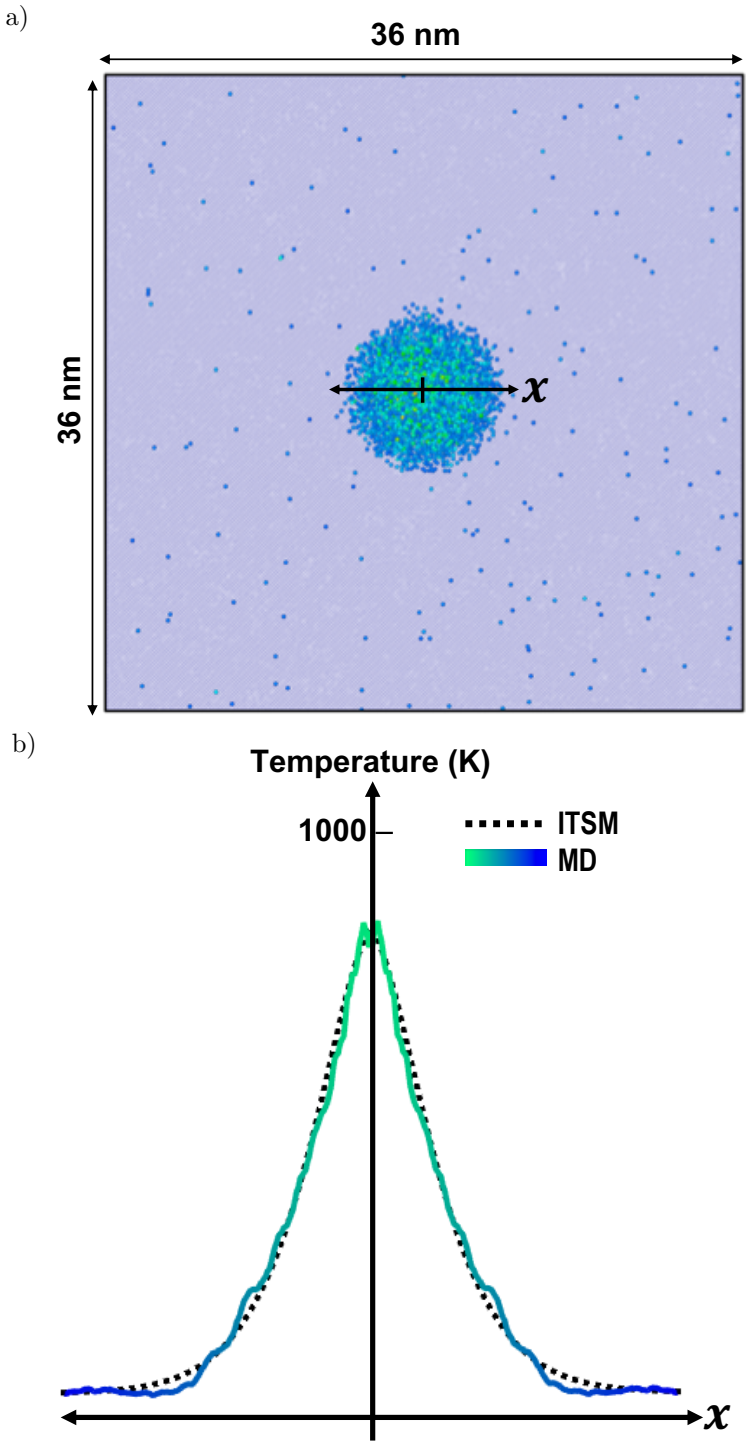

Figure 5.3: MD thermal spike spatial visualization of 50 MeV O+ ion impact in a 3C-SiC crystal for zero electric field (hence the profile matches the ITSM exactly). The MD temperature profile is taken at $t = 0.8$ ps. The lighter-colored atoms correspond to higher kinetic energies. In (a) atoms at room temperature $k_B T$ are made semi-transparent. The center region illustrates a thermal spike event, with a temperature profile shown in (b).

a)

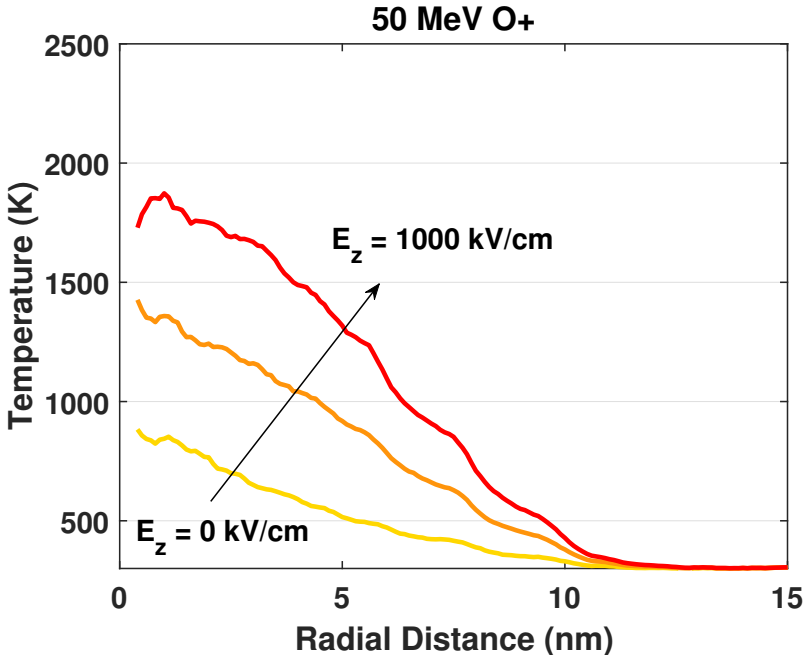

b)

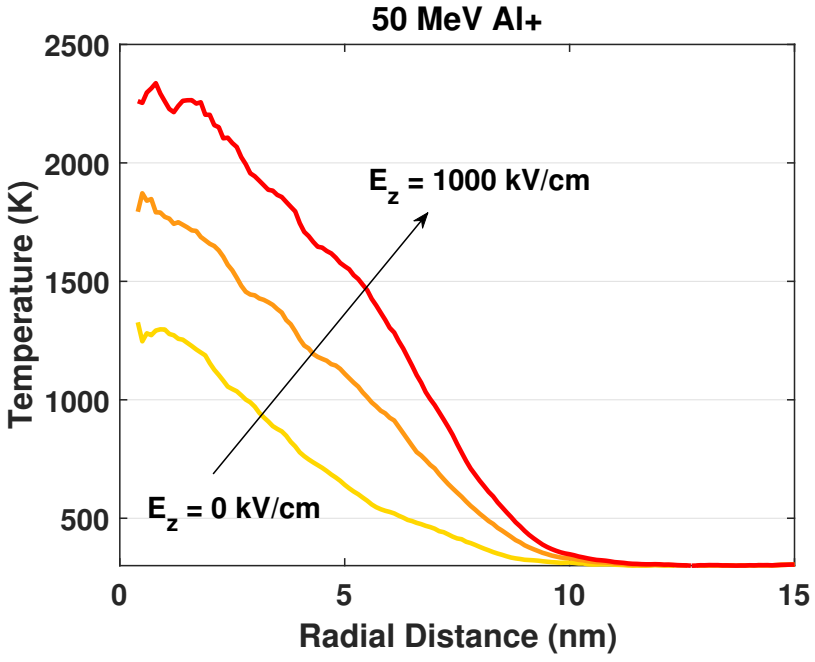

Figure 5.4: Thermal spike output of MD at $t = 0.8$ ps of a 3C-SiC crystal for a (a) 50 MeV O+ ion and a (b) 50 MeV Al+ ion.

5.4 Defect Recovery Induced by Thermal Transients in Disordered Systems

Two different ion species (50 MeV O+ and 50 MeV Al+) were considered in this work, which were selected according to their relatively larger abundance and accessibility in radiation environments [116, 135]. Analysis of the lattice disorder reveals significant defect recovery induced by the thermal spike events. Fig. 5.5 shows the lattice disorder of the relaxed system after each event, radially averaged around the center of the ion track. The relative disorder is calculated by normalizing the number of defects over a given volume by the initial defect concentration. Hence, the mean value of the radial distribution "Before Strike" is equal to unity. In the case of zero electric field, lattice healing is observed for both ion species. In particular, the slight recovery observed for O+ (1.60 keV/nm) is consistent with the data reported in [111], where a threshold value for recovery was found to be 1.40 keV/nm. It is worth noting that the nature of defect recovery is sensitive to the initial state of the defective lattice [136]. Thus, depending on the initial concentration of Si and C defects, the recovery process may differ significantly.

More importantly, Fig. 5.5 and Fig. 5.6 show significant defect recovery as E_z increases. For instance, in the case of O+, $E_z \sim 1000$ kV/cm decreases the final disorder by 33%, as shown in Fig. 5.6(a). This field is approximately at the breakdown level of 3C-SiC, and several MV/cm below the breakdown field of other SiC polytypes. The lattice disorder continues to decrease with E_z, although the silicon defect recovery appears to converge (Fig. 5.6(b)). Indeed, the concentration of carbon defects are known to be significantly greater than silicon, which is explained in part by the lower vacancy/interstitial energy barriers [130, 137]. This explains the difference in the fractional contribution of disorder for each element, as shown in Fig. 5.6(b).

However, a thermal spike simulation using the EDIP potential yields a significant difference in the defect recovery effect, as also shown in Fig. 5.6(a). For an identical thermal spike profile, negligible defect recovery is observed after a 50 MeV O+ strike when using EDIP. However, when presuming $E_z \sim 1000$ kV/cm, the defect recovery effect is observed, although the magnitude is about 20% lower when compared to the Gao-Weber potential. This difference is likely attributed to the higher activation energies associated with the EDIP potential, as reported in [134]. We stress, however, that a dedicated study on the differences between these potentials for this application is needed and encouraged (e.g. [137]).

It is worth noting that the initial charge distribution as defined by $A(r,t)$ in section 2 is a close reflection of rate of Coulomb scattering. For example, the electrons at the center of the ion track (where $n_e \sim 10^{23}$ cm^{-3}) exhibit greater Coulomb scattering than the electrons in the

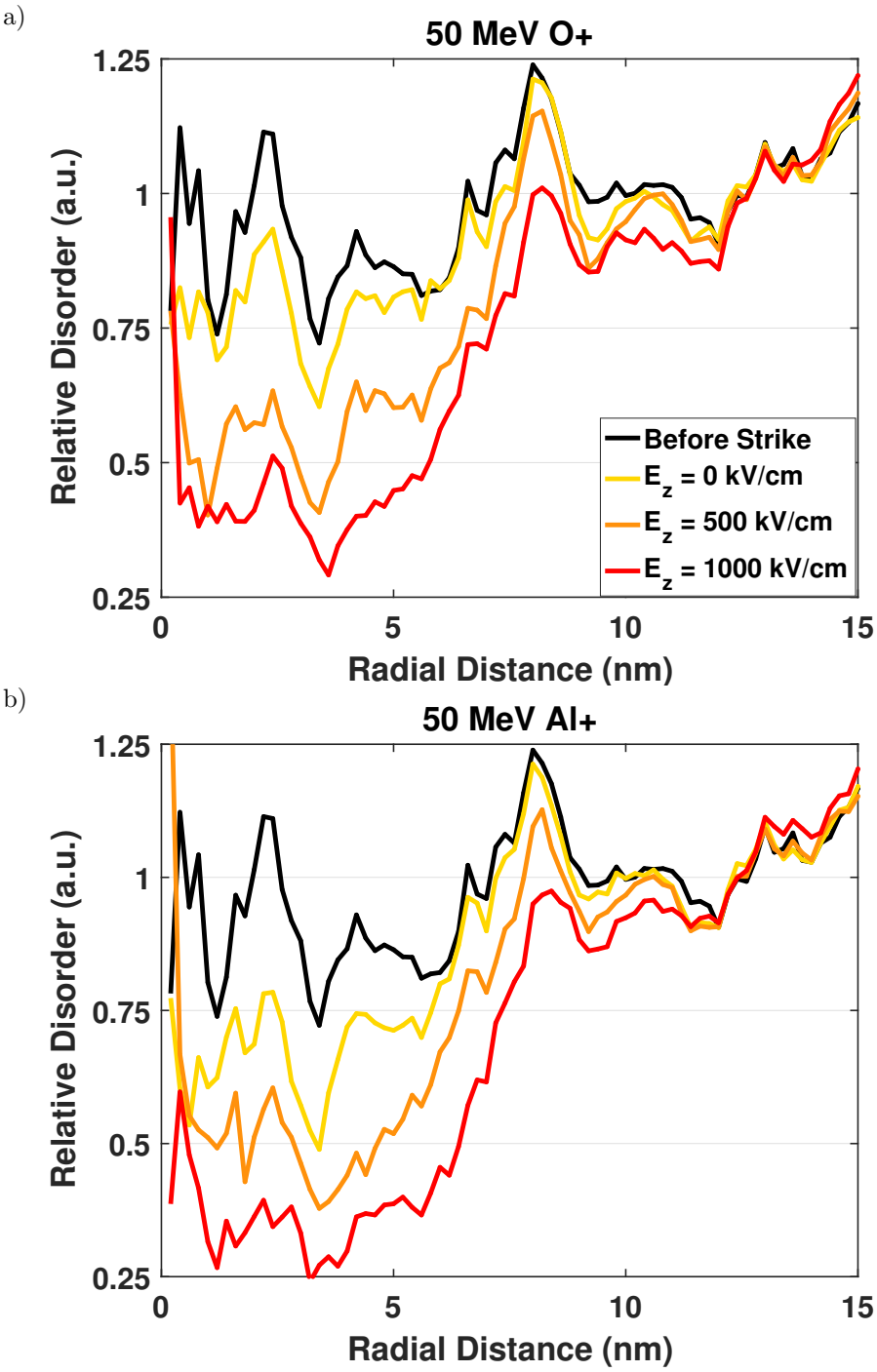

Figure 5.5: Relative disorder of SiC system at thermal equilibrium ($t = 50$ ps) for a (a) 50 MeV O+ ion and a (b) 50 MeV Al+ ion. The black line represents the disorder of the defective lattice before the ion strike. The colored lines represent the disorder of the lattice at increasing E_z.

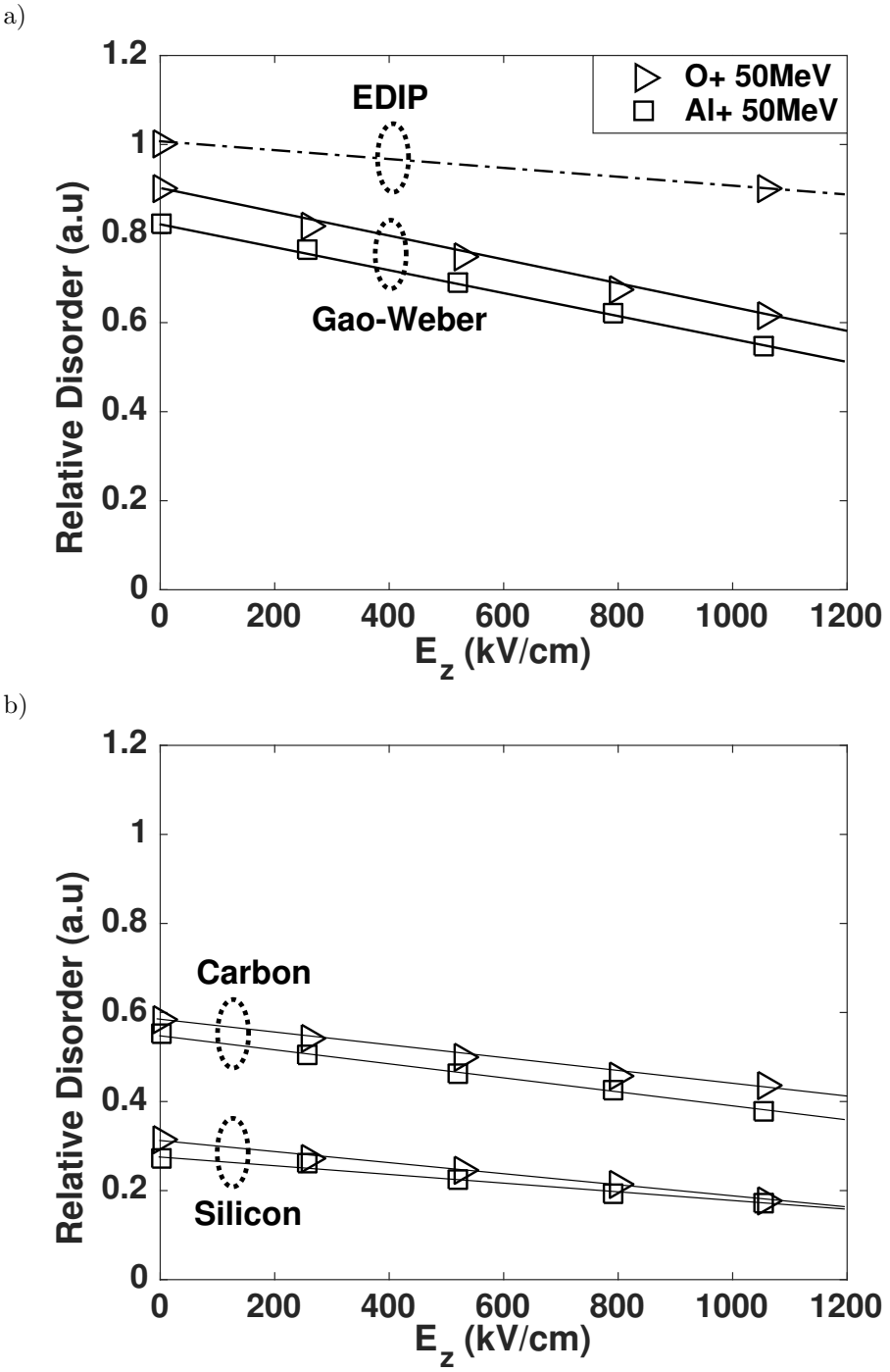

Figure 5.6: Relative disorder of 3C-SiC lattice at thermal equilibrium after thermal spike at increasing E_z. (a) A $\sim 33\%$ decrease in lattice disorder is observed as E_z increases to ~ 1000 kV/cm. The EDIP potential [134], on the other hand, exhibits a $\sim 10\%$ decrease over the same field range. (b) The contributions of disorder for carbon and silicon. The disorder was averaged over a 10 nm radius cylindrical volume around the ion path.

periphery of the ion track (where $n_e \ll 10^{21}$ cm^{-3}). Each elastic collision inhibits the energy that electrons could otherwise gain ballistically. Thus, it follows that drifting carriers gain more energy at the peripheries of the excited region. This can be consequential for ion strikes that deposit energy over larger volumes (as evidenced by the velocity effect [138]), where Coulomb scattering can be comparably much less.

These results show us that lighter ions ($S_e < 5$ keV/nm) are sufficient to induce defect recovery up to about ~ 8 nm from the track center. This translates to a modest ion fluence on the order of 10^{12} cm^{-2} if one wishes to anneal large sample regions. Previous work has demonstrated defect recovery in 3C-SiC, which include annealing induced by heavy and highly energetic ions (e.g., Pb ions of 33 keV/nm [112]) to much lighter and less energetic ions (e.g., 1.4 keV/nm [111]). Here we reiterate this phenomenon while demonstrating that, by increasing the average electron energy via an applied field bias, this recovery effect can be enhanced.

5.5 Chapter Summary

Localized heating as a consequence of radiation-induced ionization has been studied for decades, with implications that vary widely across different host materials. For 3C-SiC in particular, defect recovery resulting from heavy ion irradiation has consistently been reported. Here we report that this phenomenon can amplify in the presence of high background fields, which is a direct consequence of the high steady-state electron energy. We also hypothesize that this higher field response is more pronounced in regions with lower carrier densities, such as in ionized regions from high-velocity ions (which deposit energy over larger volumes). This work can be insightful for SiC-based applications, such as for fuel coating and structural components in nuclear reactors, or for SiC-based electronics operating in radiation-rich environments. Future work is needed to experimentally demonstrate the simulated results of this work.

Chapter 6

Conclusions and Future Work

6.1 Thesis Summary

In this thesis, we discussed the potential of diamond-based electronics for harsh environment applications. The demand to probe harsh environments will escalate in the years to come, and with it the need for electronics to sustain those conditions. Looking forward, the reliability of electronics for harsh environments becomes more feasible, so long as we fervently progress in the R&D space and optimize the performance of WBG-based devices. This latter point is what a portion of this thesis was dedicated to accomplishing: by understanding the conduction limitations of hydrogen-terminated diamond, we pave the way toward the realization of robust diamond-based electronics.

We began this thesis by overviews the merits and potential of diamond as a platform for electronics. This included its fundamental material properties which are superior to its WBG counterparts, most notably its thermal conductivity. In Chapter 2, we discussed the difficulties of doping and the promise behind hydrogen-terminated diamond surface in detail. We also overviewed the hole transport properties, including a theoretical formulation of the mobility which was used to fit to the experimental Hall-effect measurements. The background information was concluded by a discussion on irradiated materials, including the TID effects, atomic displacement events, and thermal-spikes induced by swift heavy ions.

In Chapter 3, we discussed the fabrication process of devices on diamond substrates. Extensive Hall measurements were taken at temperatures ranging from 25 K to 700 K, and a theoretical model was used to understand the mobility-limiting mechanisms. A multi-band treatment of the HH, LH, and SO band was included using a Schrödinger/Poisson solver. We determined that the

Hall-effect measurements at low-to-intermediate temperatures suggest that long-range potential fluctuations exist for a wide range of ρ_{2D}, which contributes to the "ceiling" observed for the hole mobilities at low sheet densities. These fluctuations may arise both from charged surface acceptors and disorder related to the C-H surface. The nature of this disorder is a subject that remains to be studied. Moreover, IV and CV measurements were taken on MISFETs, MESFETs, and MISCAPs, in order to analyze the FET behavior. A reasonable ON/OFF ratio and subthreshold slope was observed. Using CV measurements, it was determined that negatively fixed charge exists in the oxide, and that a small density of traps become positively-charged near the interface as the gate bias is swept, thus producing a small clockwise hysteresis behavior. Although these are promising FET characteristics, improvements must be made in increasing the saturation drain currents, which underscore the significance of maximizing the 2DHG mobility.

We reinforced our understanding of the mobility limiting mechanisms in Chapter 4, where we irradiated four single-crystal diamond samples, two of which were passivated with Al_2O_3, and the other two left unpassivated. The samples were irradiated with 2 MeV protons at two fluences, 0.5×10^{14} and 1×10^{14} cm^{-2}. In order to decouple the degradation that is intrinsic to the H:diamond from the degradation of the passivation layer, the characteristics of MESFETs and Hall-effect devices of unpassivated H:diamond samples were also exposed and measured. It was determined that the Al_2O_3 were negatively charged post-irradiation, which consequently degraded the hole mobility, but also increased the sheet density via electrostatic attraction. The net result was a substantial decrease in the drain saturation currents, and shifts in the threshold and flatband voltages. It was also determined that the hole mobility and sheet density drop on the unpassivated H:diamond samples. The net result was also a decrease in the drain saturation current. Since MeV-protons exhibit negligible nuclear scattering, and deposit their energy entirely via ionization, we suspect that the degraded hole mobility is caused via enhanced scattering off insulating barrier centers throughout the 2D hole well. Effective medium theory was used to infer the height of these barriers and the surface fraction that they occupy. By irradiating both Al_2O_3/H:diamond and Air-doped/H:diamond substrates, this study provided a holistic understanding of the degradation mechanisms of all H:diamond devices, passivated or not.

Lastly, in Chapter 5, we overviewed an instance where particle irradiation of materials is beneficial. For 3C-SiC, the recovery of defects resulting from swift heavy ion irradiation has consistently been reported. In this Chapter, however, we report that this annealing phenomenon can be amplified in the presence of high background fields, which is a direct consequence of the high steady-state electron energy. We also hypothesize that this higher field response is more

pronounced in regions with lower carrier densities, such as in ionized regions from high-velocity ions (which deposit energy over larger volumes). In general, this work can be insightful for any application in need of localized annealing solutions. For example, SiC applications include fuel coating and structural components in nuclear reactors, as well as electronics operating in radiation-rich environments. Future work is needed to experimentally demonstrate the simulated results presented in this chapter.

6.2 Future Work

Recommendations for future work are as follows:

- A highly controlled design of experiment of the hydrogen-terminated surface. The objective should be to obtain as uniform of a C-H dipole surface as possible. Moreover, a study on the spatial variation of the negatively-charged acceptors is worthwhile, as that would also produce valence band ripples. Characterization methods such as Raman and Fourier transform infrared spectroscopy can be utilized to measure the C-H vibrational mode signal as an indicator for the "completeness" of the hydrogen termination. However, the C-H signal would likely be too weak on smooth diamond surfaces, but this can be addressed by including a diamond powder in this analysis, as it will increase the probed surface area and produce a resolvable signal during spectroscopic measurements.

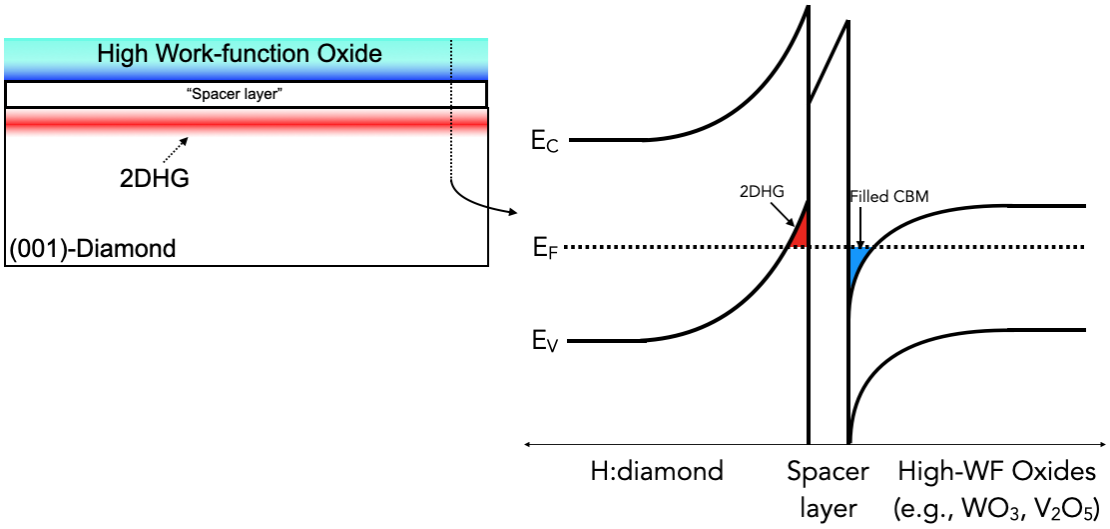

Figure 6.1: Schematic and band diagram of an H:diamond structure with a spacer layer. By separating the 2DHG from the compensating negative charge (thus increasing d from Eq. (A.6)), the hole mobility can be boosted significantly.

- The deposition of an ultra thin, high-quality "spacer" layer in between the oxide and the H:diamond would separate the 2DHG and the compensating oxide charge, thus increase d from Eq. (A.6) and substantially reducing the type-(i) SI scattering rate. A schematic and band diagram of this is shown in Fig. 6.1. One promising candidate is the deposition of hexagonal boron nitride onto (111)-oriented diamond, as done in Ref. [139]. It is important to ensure that the spacer layer has negligible acceptor levels and is high quality.

- Surface analysis studies such as transmission electron microscopy (TEM) of the H:diamond surface can add insight to the mobility-limitations of the 2DHG. It has been shown, for example, that sub-surface defects can be generating during the polishing process of the diamond surfaces (which is a typical manufacturing step after diamond synthesis) [140, 141]. TEM and other characterization methods can be used to study the quality of the atomic structure where the 2DHG exists.

- For the devices produced in this work, as well as the architectures recommended above, a thorough stress test is recommended. This includes Hall-effect and FET measurements at very high temperatures to observe oxidation effects. It was shown in Fig. 3.3, for example, that the 2DHG sheet density remained stable at temperatures just above 400°C for Al_2O_3/H:diamond Hall-effect devices.

- To build on the work presented in Chapter 5, experimental studies demonstrating the irradiation-induced healing and its dependence on applied electric fields is needed for validation. Moreover, it remains to be studied the high-energy irradiation effects on other defective semiconductor materials, and if any irradiation conditions can induce the annealing effects as observed in silicon carbide.

Appendix A

Formulation of Mobility Model

A.1 Poisson/Schrödinger solver

A.1.1 Multi-band treatment of 2DHG

Determining the average hole relaxation time requires calculating the Fermi level with respect to the valence band maximum (VBM), which is unique to each valence band and confined subbands. Moreover, since the scattering matrix elements are usually functions of effective masses, the calculated relaxation times will also be unique to each band. Therefore, in this calculation, three single-band effective mass Schrödinger equations are solved and coupled to the Poisson equation. This is performed for each of the heavy hole, light hole, and split-off valence bands (herein denoted by HH, LH, and SO). This calculation was performed using a Schrödinger/Poisson solver (nextnano^3 software) [142], as it has been used in some of the prior works for the same 2DHG H:diamond technology [143, 144]. To induce a confined accumulation of holes at the surface, a negative interface sheet density was imposed as a boundary condition at the surface. At a given temperature, the negative charge density was modulated until the hole density matched the sheet density extracted from Hall-effect measurements. Finally, a Neumman boundary condition ($\partial\varphi/\partial z = 0$) was set at 500 nm from the surface.

Once at the desired conditions, the Fermi levels for each band were extracted, given by

$$\mathcal{E}_{F,j\ell} = \mathcal{E}_{j\ell}^{VBM} - \mathcal{E}_F, \tag{A.1}$$

where $\mathcal{E}_{j\ell}^{VBM}$ is the VBM of band j (HH, LH, and SO) and subband ℓ (1, 2, and 3), and $\mathcal{E}_F$ is

the global Fermi level. The confined hole wave functions out-of-plane $\psi_{j\ell}(z)$ are used for the scattering matrix element calculations. Further, since the relative hole occupation $\rho_{2D}^{j\ell} \propto |\psi_{j\ell}(z)|^2$, we can justify simplifying our calculations by ignoring higher subbands with a low occupation number. Given the p-like orbital degeneracy of the valence bands, the occupation of holes is dominated by the ground state for each band j, even for very high sheet densities. For this reason, only the first subband ($\ell = 1$) of each band j is considered for our calculations [Fig. A.1(a)].

Together with the respective effective masses, this data establishes the starting point for the calculation of the hole relaxation times.

A.1.2 Effective masses

The mobility of any crystal structure is in large part influenced by the effective masses of the majority carriers, which therefore ties the diamond band structure into this analysis. As with any semiconductor, the behavior of holes are dictated by the two-fold degenerate HH and LH bands, as well as the SO band separated by ΔE_{so}, located at the Γ point in the $E(k)$ dispersion

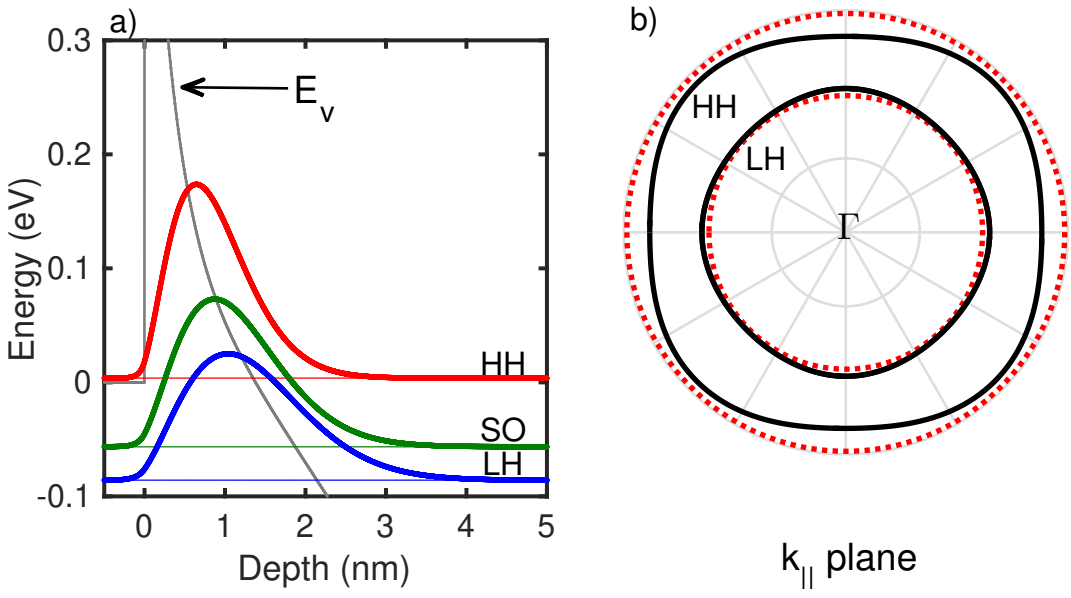

Figure A.1: (a) Ground state energy ($\ell = 1$) of HH, LH, and SO bands at the diamond surface, where the reference energy is the Fermi level at 0 eV. Superimposed are the hole probability densities for each band. (b) Constant energy surface on a $\mathbf{k}$ plane of the diamond HH and LH bands. The solid black lines are calculated using the Luttinger parameters by Naka *et al.* [145]. The dashed red lines are a parabolic approximation using the angle-averaged masses.

Valence Band	Angle-averaged	[001] direction
Heavy hole, j=HH	0.667	0.540
Light hole, j=LH	0.260	0.288
Split-off, j=SO	0.375	0.375

Table A.1: Effective masses used for our calculations. Values are in free-electron mass units [145].

diagram. Typical examples of ΔE_{so} are 44 and 28 meV for Si and Ge, respectively. Diamond is unusual in this regard, with $\Delta E_{so} \approx 6$ meV [146]. This implies that the hole occupation in the SO band is more probable, hence the importance of the multi-band treatment in our calculations.

With the exception of holes in the SO band, it is typical that the hole dispersion be highly anisotropic due to warping of the constant energy surfaces of the HH and LH bands. Via the $\mathbf{k} \cdot \mathbf{p}$ perturbation scheme, this dispersion can be analytically expressed as $E(\mathbf{k})_{HH,LH} = A\mathbf{k}^2 \pm [B^2\mathbf{k}^4 + C^2(k_x^2k_y^2 + k_y^2k_z^2 + k_z^2k_x^2)^{1/2}$, where $\mathbf{k} = \langle k_x, k_y, k_z \rangle$ is the wave vector, and the constants A, B, and C are functions of the Luttinger parameters determined experimentally [147].

For our calculations, only the most recent literature of experimental hole effective masses is considered. In one study, Y. Takahide *et al.* measured a range of effective masses through Shubnikov-de Haas oscillations on hydrogen-terminated surfaces for magnetic fields perpendicular to (111) plane. The oscillation peaks corresponded to effective masses which the authors grouped into two separate ranges: $m^*/m_0 = 0.17 - 0.36$ and $0.57 - 0.78$ [148]. These ranges reasonably encapsulate the masses reported a year prior by Naka *et al.* using cyclotron resonance experiments [145]. The latter study provides the most recently obtained Luttinger parameters of $\gamma_1 = 2.67$, $\gamma_2 = -0.403$, and $\gamma_3 = 0.680$, which in turn yield 2.67, -0.8, and 1.9049 for constants A, B, and C, respectively. Cross-sections of the constant energy surfaces for HH and LH bands are plotted in Fig. A.1(b) about the Γ point. This plot shows that, although warping of the valence bands is visible, it is reasonable for our purposes to treat dispersion as parabolic (i.e., $E(k) = \hbar^2k^2/(2m^*)$). Thus, using the data by N. Naka, we use the angle-averaged hole masses for the in-plane effective masses in our scattering model. For the out-of-plane calculations performed by the Schrödinger/Poisson solver, the [001] effective masses are used. These masses are listed in Table A.1.

A.2 Relaxation time expressions

A.2.1 Surface Impurity Scattering

A major consequence of the charge transfer phenomenon is that the 2DHG is compensated by negatively charged acceptor states, which can be provided by air-adsorbates or oxide films. The sheet separation of the hole gas and negative compensating charge is on the order of angstroms. Thus, the induced Coulombic forces perturb the 2D potential well, which significantly degrades the hole mobility. Such 2D carrier channels in other material stacks, such as the 2DEG in remotely-doped AlGaAs/GaAs heterostructures, are relatively distant from the charged donors, which allows for electron mobilities as high as 10^4 cm^2/(V·s). However, even for these structures, the mobility can be limited by these remote impurities, especially at low temperatures. Hence, this scattering mechanism has been modeled for 2D carriers, and is adopted herein [149]. Moreover, disorder related to the C-H dipoles (such as incomplete hydrogen termination [38, 61], non-homogeneous acceptor distribution [67], and variation in surface reconstruction [24], the existence of oxygen-related catalysts [65], etc.) may interfere with the conductivity of holes. Together with the negatively charged acceptor states, these field-inducing phenomena distort the band structure and thus act as scattering centers which dominate at low sheet densities. We will unravel this further in the discussion and results section. Here we denote the scattering by the negatively charged surface acceptors as type (i), and the scattering induced by the C-H disorder as type (ii). The matrix element is expressed as

$$\begin{aligned} M_{si}(\mathbf{q}) &= \int_0^\infty |\psi(z)|^2 \, dz \int V(\mathbf{r}, z) \exp(i\mathbf{q} \cdot \mathbf{r}) d^2\mathbf{r}, \\ &= \int_0^\infty |\psi(z)|^2 \, \mathcal{V}(q, z) dz, \end{aligned} \tag{A.2}$$

where $\mathcal{V}(q, z)$ is the Fourier transform of the potential form of a charged impurity. Following Ref. [149], properly taking charged screening into account gives us

$$\mathcal{V}(q, z) = \frac{Ze^2}{2\varepsilon_0 \epsilon(q)} \frac{\exp(-q(z + |d|))}{q}, \tag{A.3}$$

where Z is the electronic charge number and $\epsilon(q)$ is the dielectric constant defined by

$$\epsilon(q) = \varepsilon_s \left(1 + \frac{q_{TF} F(q)}{q}\right). \tag{A.4}$$

Here, screening is treated via the 2D Thomas-Fermi wave vector $q_{TF} = m^*_{dos} e^2/(2\pi\varepsilon_0\varepsilon_s\hbar^2)$, and $F(q)$ is a form factor defined by

$$F(q) = \int dz \int dz' |\psi(z)|^2 |\psi(z')|^2 \exp\left(-q|z - z'|\right). \tag{A.5}$$

With the wave functions (confined along z) and the wave vectors treated parabolically in two-dimensions, the scattering rate can be expressed as

$$\frac{1}{\tau_{si}^{(i),(ii)}} = \frac{(Z^2 N_{si})^{(i),(ii)} m^*_{dos}}{2\pi\hbar^3 k^3} \left(\frac{e^2}{2\varepsilon_0\varepsilon_s}\right)^2 \int_0^\infty dz\, |\psi(z)|^2 \times \int_0^{2k} \frac{\exp(-2q(z + |d|))}{(q + F(q) q_{TF})^2} \frac{q^2 dq}{\sqrt{1 - (q/2k)^2}}, \tag{A.6}$$

where $(Z^2 N_{si})^{(i)}$ and $(Z^2 N_{si})^{(ii)}$ are the fitting parameters for SI scattering of types (i) and (ii), respectively. Throughout the text, Z is absorbed into the fitting parameter for type (ii) scattering since the nature of the induced fields is uncertain. Thus we define $\mathcal{N}_{si}^{(ii)} = (Z^2 N_{si})^{(ii)}$. For type (i) scattering, however, each ionized surface acceptor is presumed to have a charge of unity. Thus we set $(Z^2 N_{si})^{(i)} = N_{si}^{(i)}$.

A.2.2 Surface Roughness Scattering

Roughness in the form of spatial fluctuations at the H:diamond surface may be induced via diamond growth, exposure to hydrogen plasma, or during the fabrication process. Hence, the fluctuations produce localized potentials randomly distributed along the plane, which act as scattering centers for holes. If the fluctuations are on the order of carrier wavelengths, then scattering can be significant. We denote the average out-of-plane fluctuations as Δ (i.e., root-mean-squared (RMS) roughness height) and the average in-plane separation of these fluctuations as Λ (i.e., correlation length). These roughness variables are expressed by a Gaussian distribution as $\langle \Delta(\mathbf{r}) \Delta(\mathbf{r}') \rangle = \Delta^2 \exp\left[(\mathbf{r} - \mathbf{r}')^2/\Lambda^2\right]$. The formalism by Ando *et al.* [150] is adopted here for H:diamond, which expresses the scattering matrix element as

$$|M_{sr}(\mathbf{q})|^2 = \frac{e^4\rho_{2D}^2}{4\varepsilon^2}\frac{\pi\Delta^2\Lambda^2}{L^2}\exp\left(\frac{-q^2\Lambda^2}{4}\right), \tag{A.7}$$

where the Fourier transform of the **r**-Gaussian distribution $\langle|\Delta(\mathbf{q})|^2\rangle$ was used for the matrix element. Here we presume that the sheet hole density ρ_{2D} is the only form of charge and ignore other variants (e.g., space charge density). With the substitution of Eq. (A.7) into the 2D transport lifetime expression and integrating over the wave vector plane, the final form is

$$\frac{1}{\tau_{sr}} = \frac{\pi m_{dos}^*\Delta^2\Lambda^2 e^4\rho_{2D}^2}{\hbar^3(\varepsilon_0\epsilon(q))^2}\exp\left(-\frac{q^2\Lambda^2}{4}\right), \tag{A.8}$$

Note from Eq. (A.8) that the scattering rate increases with the square of ρ_{2D}, and may thus be insignificant at low sheet densities.

A.2.3 Non-polar Optical Phonon Scattering

Scattering of carriers by phonons dominate at high temperatures, which is an intrinsic phenomenon in all materials. Thus, hole-phonon interactions are dependent on the physical parameters of the material, such as the effective mass, material density, and (in the case of carriers confined to a 2D plane) the z-plane probability density of the 2DHG. It is for this reason that in the limit of higher temperatures, carrier-phonon interactions are the insurmountable limiting factor of carrier mobilities. In this section, we define the relaxation time for holes interactions with non-polar optical phonon (NOP), which exhibits a steep slope with respect to temperature.

This scattering matrix is commonly defined as the product of the deformation potential D_{op} and the optical phonon displacement vector $\mathbf{u}_{op}$, expressed as $|M_i(\mathbf{q})| = D_{op}\cdot\mathbf{u}_{op}$. The displacement vector, derived in Ref. [151], yields the scattering matrix

$$|M_{nop}(\mathbf{q})|^2 = \frac{D_{op}^2\hbar}{2\rho L^3\omega_0}\times\left(n(\omega_0)+\frac{1}{2}\pm\frac{1}{2}\right), \tag{A.9}$$

where ρ is the material density of diamond, $n(\omega_0)$ is the phonon occupation factor, and $\hbar\omega_0$ is the NOP energy, which is assumed to be dispersion-less and thus independent of $\mathbf{q}$. Due to confinement along the z-direction, carriers are restricted along the $\mathbf{r}$ plane, while phonons are treated in three dimensions ($\mathbf{q}^2+q_z^2$). Hence, the three-dimensional form of Eq. (2.10) is used and quantized along the q_z direction. The final expression yields

$$\frac{1}{\tau_{nop}} = \int |I(q_z)|^2 dq_z \cdot \frac{m^*_{dos} D^2_{nop}}{4\pi\rho\hbar^2\omega_0} \times \left(n_0(\omega_0) + \frac{1}{2} \pm \frac{1}{2} \right) \Theta(\mathcal{E}_k \mp \hbar\omega_0), \tag{A.10}$$

where the overlap integral is defined by $|I(q_z)| = \int |\psi(z)|^2 \exp(iq_z z)dz$, and $\Theta(x)$ is the step function which is unity when $x \geq 0$ and zero otherwise. Here we also recognized that the integration over $\delta[\mathcal{E}_{\mathbf{k}'} - \mathcal{E}_{\mathbf{k}}]/(2\pi)^2$ is the definition of the 2D density of states $m^*_{dos}/\pi\hbar^2$.

We note that, in reality, the momentum transitions may be sufficient to scatter between the HH, LH, and SO bands. In our calculations, such inter-valence band scattering is not explicitly differentiated between intra-band scattering. Instead, the coupling strength associated with intra- and inter-valence band scattering is expressed by the coupling constant D_{nop}, as it is impractical to independently distinguish between them when fitting to experiments.

A.2.4 Acoustic Phonons

At low to intermediate temperatures, acoustic phonons are the most dominant species of electron-phonon scattering. As with NOP scattering, the potential D_{ac} and the acoustic phonon displacement vector $\mathbf{u}_{ap}$ define the scattering matrix as

$$\begin{aligned} |M_{ap}(\mathbf{q})|^2 &= \frac{q^2 D^2_{ap}\hbar}{2\rho L^3\omega_q} \times \left(n(\omega_q) + \frac{1}{2} \pm \frac{1}{2} \right), \\ &= \frac{D^2_{ap} k_B T}{2\rho L^3 v_s^2}, \end{aligned} \tag{A.11}$$

where v_s is the longitudinal sound velocity. Here we invoked the equipartition theorem, where $\hbar\omega_q \ll k_B T$, therefore the phonon occupation number $n(\omega_q) = 1/(\exp(\hbar\omega_q/k_B T) - 1)) \gg 1$. Hence we can say that $n(\omega_q) \approx n(\omega_q) + 1 \approx k_B T/\hbar\omega_q$. We also treat the acoustic dispersion relation as linear, i.e. $\omega_q \approx v_s q$. Treating the integration similarly as in Eqs. (A.9)–(A.10) yields

$$\frac{1}{\tau_{ap}} = \int |I(q_z)|^2 dq_z \cdot \frac{m^*_{dos} k_B T D^2_{ap}}{\pi\hbar^3\rho v_s^2}. \tag{A.12}$$

Appendix B

H:diamond Fabrication Process

Below is the H:diamond fabrication runsheet. This sheet is followed by an identical sheet with comments associated with each fabrication step. A database with this runsheet is available on Stanford's SNF website at: https://snfexfab.stanford.edu/snf/projects-processes/runsheets

H:diamond FABRICATION RUNSHEET

Name	Step#	Process	Time	Tool	Recipe
Spin/ Expose Process	0				
	0.1	Clean sample	6 min	wbsolv	Acetone/IPA
	0.2	Spin LOL2000	40 sec	Headway3	6000 RPM
	0.3	Post-spin bake	5 min	Hot plate	170 degC
	0.4	Spin SPR3612	60 sec	Headway3	8000 RPM
	0.5	Post-spin bake	60 sec	Hot plate	90 degC
	0.6	Exposure	-	Heidelberg2	Uploaded Layout
	0.7	Post-bake	60 sec	Hot plate	115 degC
	0.8	Develop	35-40 sec	wbdev	MF26A
	0.9	Rinse	30 sec	wbdev	DI water
	0.1	Inspect	-	Microscope	-
Mask1 (Bond Pads)	1				
	1.1	Spin resists/Expose	-	-	-
	1.2	O-plasma	90 sec	Technics/Samco	100W
	1.3	Metal evaporation	-	AJA	5/20/20nm Ti/Pt/Au
	1.4	Lift off contacts	2 hours	wbsolv	1165 remover
	1.5	Rinse	2 min	wbsolv	Acetone/IPA
Mask2 (Ohmic Contacts)	2				
	2.1	Spin resists/Expose	-	-	-
	2.2	Metal evaporation	-	AJA	80nm Au
	2.3	Lift off contacts	2 hours	wbsolv	1165 remover
	2.4	Rinse clean	2 min	wbsolv	Acetone/IPA
Mask3 (Isolation regions)	3				
	3.1	Spin resists/Expose	-	-	-
	3.2	O-plasma	90 sec	Technics/Samco	100W
	3.3	Lift off 3612	2 hours	wbsolv	1165 remover
	3.4	Rinse clean	2 min	wbsolv	Acetone/IPA
ALD	4				
	4.1	Rinse clean	2 min	wbsolv	Acetone/IPA
	4.2	Season ALD chamber	-	Fiji2	Thermal Al2O3, 250C
	4.3	Deposition	∼90 min	Fiji2	Thermal Al2O3, 250C
	4.4	Inspect	-	Microscope	-

Mask4 (Gate Contacts)	5				
	5.1	Spin resists/Expose	-	-	-
	5.2	Metal evaporation	-	AJA	50/20 nm Ti/Pt
	5.3	Lift off contacts	2 hours	wbsolv	1165 remover
	5.4	Rinse clean	2 min	wbsolv	Acetone/IPA
Mask5 (Open Contacts)	6				
	6.1	Spin resist/Expose	-	-	-
	6.2	Etch oxide	90 sec	wbflexcorr	20:1 BOE
	6.3	Rinse clean	60 sec	wbflexcorr	DI water
	6.4	Strip resist	1 hour	wbsolv	Acetone
	6.5	Rinse clean	60 sec	wbsolv	IPA

RUNSHEET COMMENTS

Name	**Step#**	**Process**	**Comment**
Spinning/ Expose Process	0		
	0.1	Clean sample	5min Acetone, 1min IPA. Sonication is optional
	0.2	Spin LOL2000	Ramp rate 3000 RPM/sec. Use pipets.
	0.3	Post-spin bake	Use carrier wafer for handling
	0.4	Spin SPR3612	Ramp rate 4000 RPM/sec. Use pipets
	0.5	Post-spin bake	Use carrier wafer for handling
	0.6	Exposure	70 power/-2 defocus
	0.7	Post-bake	Use carrier wafer for handling
	0.8	Develop	Place sample on top of wipes, and get a good grip with tweezers. Agitate sample well in the MF26A. Don't let go of sample.
	0.9	Rinse	Agitate sample well in the water. Dry well with N2 gun.
	0.10	Inspect	This is where you determine if the spin-exposure process went well or dire.
Mask1 (Bond Pads)	1		
	1.1	Spin resists/Expose	Complete step 0
	1.2	O-plasma	Ensure sample is dry, use hot plate if necessary.
	1.3	Metal evaporation	Max deposition rate 1 Ang/sec
	1.4	Lift off contacts	Submerge into 1165 for 10 min, remove and quickly spray with acetone to remove metal, and resubmerge in 1165 for $\sim$2 hours.
	1.5	Rinse	1 min acetone, 1 min IPA
Mask2 (Ohmic Contacts)	2		
	2.1	Spin resists/Expose	Complete step 0
	2.2	Metal evaporation	Max deposition rate 1 Ang/sec
	2.3	Lift off contacts	Submerge into 1165 for 10 min, remove and quickly spray with acetone to remove metal, and resubmerge in 1165 for $\sim$2 hours.
	2.4	Rinse clean	1 min acetone, 1 min IPA

Mask3 (Isolation regions)	3		
	3.1	Spin resists/Expose	Complete step 0, INVERT layout during Heidelberg exposure
	3.2	O-plasma	Ensure sample is dry, use hot plate if necessary.
	3.3	Lift off 3612	Submerge into 1165 for 10 min, remove and quickly spray with acetone, and resubmerge in 1165 for ∼2 hours.
	3.4	Rinse clean	1 min acetone, 1 min IPA
ALD	4		
	4.1	Rinse clean	1 min acetone, 1 min IPA
	4.2	Season ALD chamber	50-75 cycle seasoning of chamber
	4.3	Deposition	1200 sec wait time. Deposit 200-250 cycles (∼20-25nm)
	4.4	Inspect	Surface should have a yellow hue.
Mask4 (Gate Contacts)	5		
	5.1	Spin resists/Expose	Complete step 0
	5.2	Metal evaporation	Max deposition rate 1 Ang/sec
	5.3	Lift off contacts	Submerge into 1165 for 10 min, remove and quickly spray with acetone to remove metal, and resubmerge in 1165 for ∼1 hours.
	5.4	Rinse clean	1 min acetone, 1 min IPA
Mask5 (Open Contacts)	6		
	6.1	Spin resist/Expose	Complete step 0, skip steps 0.2 and 0.3
	6.2	Etch oxide	Ensure that you have a good grip on your sample.
	6.3	Rinse clean	
	6.4	Strip resist	
	6.5	Rinse clean	

Appendix C

Codes

The raw and processed data required to reproduce the ensemble monte carlo and molecular dynamics results are available to download from doi:10.17632/wj2cy3kvy4.1.

Bibliography

[1] M. Mehregany, C. A. Zorman, N. Rajan, and C. H. Wu, "Silicon carbide mems for harsh environments," *Proceedings of the IEEE*, vol. 86, no. 8, pp. 1594–1609, 1998.

[2] P. G. Neudeck, R. S. Okojie, and L.-Y. Chen, "High-temperature electronics-a role for wide bandgap semiconductors?," *Proceedings of the IEEE*, vol. 90, no. 6, pp. 1065–1076, 2002.

[3] R. W. Johnson, J. L. Evans, P. Jacobsen, J. R. Thompson, and M. Christopher, "The changing automotive environment: high-temperature electronics," *IEEE transactions on electronics packaging manufacturing*, vol. 27, no. 3, pp. 164–176, 2004.

[4] P. G. Neudeck, R. D. Meredith, L. Chen, D. J. Spry, L. M. Nakley, and G. W. Hunter, "Prolonged silicon carbide integrated circuit operation in venus surface atmospheric conditions," *AIP Advances*, vol. 6, no. 12, p. 125119, 2016.

[5] R. Patterson, A. Hammoud, and M. Elbuluk, "Assessment of electronics for cryogenic space exploration missions," *Cryogenics*, vol. 46, no. 2-3, pp. 231–236, 2006.

[6] E. A. Gutierrez-D, J. Deen, and C. Claeys, *Low temperature electronics: physics, devices, circuits, and applications*. Elsevier, 2000.

[7] J. Tsao, S. Chowdhury, M. Hollis, D. Jena, N. Johnson, K. Jones, R. Kaplar, S. Rajan, C. Van de Walle, E. Bellotti, *et al.*, "Ultrawide-bandgap semiconductors: Research opportunities and challenges," *Advanced Electronic Materials*, vol. 4, no. 1, p. 1600501, 2018.

[8] M. W. Geis, T. C. Wade, C. H. Wuorio, T. H. Fedynyshyn, B. Duncan, M. E. Plaut, J. O. Varghese, S. M. Warnock, S. A. Vitale, and M. A. Hollis, "Progress toward diamond power field-effect transistors (phys. status solidi a 22/ 2018)," *physica status solidi (a)*, vol. 215, no. 22, p. 1870050, 2018.

[9] M. Rosker, C. Bozada, H. Dietrich, A. Hung, D. Via, S. Binari, E. Vivierios, E. Cohen, and J. Hodiak, "The darpa wide band gap semiconductors for rf applications (wbgs-rf) program: Phase ii results," *CS ManTech*, vol. 1, pp. 1–4, 2009.

[10] J. Dodson, J. Brandon, H. Dhillon, I. Friel, S. Geoghegan, T. Mollart, P. Santini, G. Scarsbrook, D. Twitchen, A. Whitehead, *et al.*, "Single crystal and polycrystalline cvd diamond for demanding optical applications," in *Window and Dome Technologies and Materials XII*, vol. 8016, p. 80160L, International Society for Optics and Photonics, 2011.

[11] L. Childress and R. Hanson, "Diamond nv centers for quantum computing and quantum networks," *MRS bulletin*, vol. 38, no. 2, pp. 134–138, 2013.

[12] D. Kania, M. Landstrass, M. Plano, L. Pan, and S. Han, "Diamond radiation detectors," *Diamond and related materials*, vol. 2, no. 5-7, pp. 1012–1019, 1993.

[13] V. Avrutin, D. J. Silversmith, Y. Mori, F. Kawamura, Y. Kitaoka, and H. Morkoc, "Growth of bulk gan and aln: Progress and challenges," *Proceedings of the IEEE*, vol. 98, no. 7, pp. 1302–1315, 2010.

[14] S. Strite, M. Lin, and H. Morkoc, "Progress and prospects for gan and the iii–v nitride semiconductors," *Thin Solid Films*, vol. 231, no. 1-2, pp. 197–210, 1993.

[15] T. Kachi, "Recent progress of gan power devices for automotive applications," *Japanese Journal of Applied Physics*, vol. 53, no. 10, p. 100210, 2014.

[16] Y.-f. Meng, C.-s. Yan, S. Krasnicki, Q. Liang, J. Lai, H. Shu, T. Yu, A. Steele, H.-k. Mao, and R. J. Hemley, "High optical quality multicarat single crystal diamond produced by chemical vapor deposition," *physica status solidi (a)*, vol. 209, no. 1, pp. 101–104, 2012.

[17] H. Yamada, A. Chayahara, Y. Mokuno, Y. Kato, and S. Shikata, "A 2-in. mosaic wafer made of a single-crystal diamond," *Applied Physics Letters*, vol. 104, no. 10, p. 102110, 2014.

[18] H. Yamada, A. Chayahara, Y. Mokuno, Y. Kato, and S. Shikata, "A 2-in. mosaic wafer made of a single-crystal diamond," *Applied Physics Letters*, vol. 104, no. 10, p. 102110, 2014.

[19] M. Schreck, S. Gsell, R. Brescia, and M. Fischer, "Ion bombardment induced buried lateral growth: the key mechanism for the synthesis of single crystal diamond wafers," *Scientific reports*, vol. 7, p. 44462, 2017.

[20] S. C. Eaton, A. B. Anderson, J. C. Angus, Y. E. Evstefeeva, and Y. V. Pleskov, "Co-doping of diamond with boron and sulfur," *Electrochemical and Solid State Letters*, vol. 5, no. 8, p. G65, 2002.

[21] W. Götz, N. Johnson, J. Walker, D. Bour, and R. Street, "Activation of acceptors in mg-doped gan grown by metalorganic chemical vapor deposition," *Applied Physics Letters*, vol. 68, no. 5, pp. 667–669, 1996.

[22] V. Heera, D. Panknin, and W. Skorupa, "p-type doping of sic by high dose al implantation—problems and progress," *Applied Surface Science*, vol. 184, no. 1-4, pp. 307–316, 2001.

[23] S. Keller, G. Parish, P. Fini, S. Heikman, C.-H. Chen, N. Zhang, S. DenBaars, U. Mishra, and Y.-F. Wu, "Metalorganic chemical vapor deposition of high mobility algan/gan heterostructures," *Journal of applied physics*, vol. 86, no. 10, pp. 5850–5857, 1999.

[24] H. Kawarada, "Hydrogen-terminated diamond surfaces and interfaces," *Surface Science Reports*, vol. 26, no. 7, pp. 205 – 259, 1996.

[25] L. E. Brus, "A simple model for the ionization potential, electron affinity, and aqueous redox potentials of small semiconductor crystallites," *The Journal of chemical physics*, vol. 79, no. 11, pp. 5566–5571, 1983.

[26] F. Maier, J. Ristein, and L. Ley, "Electron affinity of plasma-hydrogenated and chemically oxidized diamond (100) surfaces," *Physical Review B*, vol. 64, no. 16, p. 165411, 2001.

[27] J. Rameau, J. Smedley, E. Muller, T. Kidd, and P. Johnson, "Properties of hydrogen terminated diamond as a photocathode," *Physical review letters*, vol. 106, no. 13, p. 137602, 2011.

[28] F. Maier, M. Riedel, B. Mantel, J. Ristein, and L. Ley, "Origin of surface conductivity in diamond," *Phys. Rev. Lett.*, vol. 85, pp. 3472–3475, Oct 2000.

[29] H. Kawarada, T. Yamada, D. Xu, Y. Kitabayashi, M. Shibata, D. Matsumura, M. Kobayashi, T. Saito, T. Kudo, M. Inaba, *et al.*, "Diamond mosfets using 2d hole gas with 1700v breakdown voltage," in *2016 28th International Symposium on Power Semiconductor Devices and ICs (ISPSD)*, pp. 483–486, IEEE, 2016.

[30] Z. Ren, D. Lv, J. Xu, J. Zhang, J. Zhang, K. Su, C. Zhang, and Y. Hao, "High temperature (300 c) ald grown al2o3 on hydrogen terminated diamond: Band offset and electrical properties of the mosfets," *Applied Physics Letters*, vol. 116, no. 1, p. 013503, 2020.

[31] C. Verona, W. Ciccognani, S. Colangeli, E. Limiti, M. Marinelli, and G. Verona-Rinati, "Comparative investigation of surface transfer doping of hydrogen terminated diamond by high electron affinity insulators," *Journal of Applied Physics*, vol. 120, no. 2, p. 025104, 2016.

[32] M. Kubovic and M. Kasu, "Enhancement and stabilization of hole concentration of hydrogen-terminated diamond surface using ozone adsorbates," *Japanese Journal of Applied Physics*, vol. 49, no. 11R, p. 110208, 2010.

[33] S. Gi, K. Tashiro, S. Tanaka, T. Fujisawa, H. Kimura, T. Kurosu, M. Iida, *et al.*, "Hall effect measurements of surface conductive layer on undoped diamond films in no2 and nh3 atmospheres," *Japanese journal of applied physics*, vol. 38, no. 6R, p. 3492, 1999.

[34] M. Kasu, H. Sato, and K. Hirama, "Thermal stabilization of hole channel on h-terminated diamond surface by using atomic-layer-deposited al2o3 overlayer and its electric properties," *Applied Physics Express*, vol. 5, p. 025701, feb 2012.

[35] H. Sato and M. Kasu, "Maximum hole concentration for hydrogen-terminated diamond surfaces with various surface orientations obtained by exposure to highly concentrated no2," *Diamond and related materials*, vol. 31, pp. 47–49, 2013.

[36] K. G. Crawford, A. Tallaire, X. Li, D. A. Macdonald, D. Qi, and D. A. Moran, "The role of hydrogen plasma power on surface roughness and carrier transport in transfer-doped h-diamond," *Diamond and Related Materials*, vol. 84, pp. 48–54, 2018.

[37] D. Oing, M. Geller, A. Lorke, and N. Wohrl, "Tunable carrier density and high mobility of two-dimensional hole gases on diamond: The role of oxygen adsorption and surface roughness," *Diamond and Related Materials*, vol. 97, p. 107450, 2019.

[38] J. A. Garrido, T. Heimbeck, and M. Stutzmann, "Temperature-dependent transport properties of hydrogen-induced diamond surface conductive channels," *Phys. Rev. B*, vol. 71, p. 245310, Jun 2005.

[39] R. Peterson, M. Malakoutian, X. Xu, C. Chapin, S. Chowdhury, and D. G. Senesky, "Analysis of mobility-limiting mechanisms of the two-dimensional hole gas on hydrogen-terminated diamond," *Phys. Rev. B*, vol. 102, p. 075303, Aug 2020.

[40] E. R. Benton and E. Benton, "Space radiation dosimetry in low-earth orbit and beyond," *Nuclear Instruments and Methods in Physics Research Section B: Beam Interactions with Materials and Atoms*, vol. 184, no. 1-2, pp. 255–294, 2001.

[41] E. W. Lemmon, M. L. Huber, M. O. McLinden, *et al.*, "Nist standard reference database 23," *Reference fluid thermodynamic and transport properties (REFPROP), version*, vol. 9, 2010.

[42] S. J. Pearton, F. Ren, E. Patrick, M. Law, and A. Y. Polyakov, "Ionizing radiation damage effects on gan devices," *ECS Journal of solid state science and technology*, vol. 5, no. 2, p. Q35, 2015.

[43] A. Ionascut-Nedelcescu, C. Carlone, A. Houdayer, H. Von Bardeleben, J.-L. Cantin, and S. Raymond, "Radiation hardness of gallium nitride," *IEEE Transactions on Nuclear Science*, vol. 49, no. 6, pp. 2733–2738, 2002.

[44] F. Nava, G. Bertuccio, A. Cavallini, and E. Vittone, "Silicon carbide and its use as a radiation detector material," *Measurement Science and Technology*, vol. 19, no. 10, p. 102001, 2008.

[45] W. Monch, "Role of virtual gap states and defects in metal-semiconductor contacts," in *Electronic Structure of Metal-Semiconductor Contacts*, pp. 224–227, Springer, 1990.

[46] H. Kawarada, M. Aoki, H. Sasaki, and K. Tsugawa, "Characterization of hydrogen-terminated cvd diamond surfaces and their contact properties," *Diamond and Related Materials*, vol. 3, no. 4-6, pp. 961–965, 1994.

[47] I. Motochi, N. Makau, and G. Amolo, "Metal–semiconductor ohmic contacts: An ab initio density functional theory study of the structural and electronic properties of metal–diamond (111)-(1× 1) interfaces," *Diamond and related materials*, vol. 23, pp. 10–17, 2012.

[48] T. Ichibha, K. Hongo, I. Motochi, N. Makau, G. Amolo, and R. Maezono, "Adhesion of electrodes on diamond (111) surface: A dft study," *Diamond and Related Materials*, vol. 81, pp. 168–175, 2018.

[49] A. Daicho, T. Saito, S. Kurihara, A. Hiraiwa, and H. Kawarada, "High-reliability passivation of hydrogen-terminated diamond surface by atomic layer deposition of al2o3," *Journal of Applied Physics*, vol. 115, no. 22, p. 223711, 2014.

[50] Z. Ren, G. Yuan, J. Zhang, L. Xu, J. Zhang, W. Chen, and Y. Hao, "Hydrogen-terminated polycrystalline diamond mosfets with al2o3 passivation layers grown by atomic layer deposition at different temperatures," *AIP Advances*, vol. 8, no. 6, p. 065026, 2018.

[51] H. Kawarada, T. Yamada, D. Xu, H. Tsuboi, Y. Kitabayashi, D. Matsumura, M. Shibata, T. Kudo, M. Inaba, and A. Hiraiwa, "Durability-enhanced two-dimensional hole gas of ch diamond surface for complementary power inverter applications," *Scientific reports*, vol. 7, p. 42368, 2017.

[52] K. Matsunaga, T. Tanaka, T. Yamamoto, and Y. Ikuhara, "First-principles calculations of intrinsic defects in al 2 o 3," *Physical Review B*, vol. 68, no. 8, p. 085110, 2003.

[53] M. Y. Yang, K. Kamiya, and K. Shiraishi, "Interstitial oxygen induced fermi level pinning in the al2o3-based high-k misfet with heavy-doped n-type poly-si gates," *AIP Advances*, vol. 3, no. 10, p. 102113, 2013.

[54] F. Werner and J. Schmidt, "Manipulating the negative fixed charge density at the c-si/al2o3 interface," *Applied Physics Letters*, vol. 104, no. 9, p. 091604, 2014.

[55] Y. Li, J.-F. Zhang, G.-P. Liu, Z.-Y. Ren, J.-C. Zhang, and Y. Hao, "Mobility of two-dimensional hole gas in h-terminated diamond," *physica status solidi (RRL) Rapid Research Letters*, vol. 12, no. 3, p. 1700401, 2018.

[56] K. Hirama, H. Takayanagi, S. Yamauchi, J. H. Yang, H. Kawarada, and H. Umezawa, "Spontaneous polarization model for surface orientation dependence of diamond hole accumulation layer and its transistor performance," *Applied Physics Letters*, vol. 92, no. 11, p. 112107, 2008.

[57] F. Liu, Y. Cui, M. Qu, and J. Di, "Effects of hydrogen atoms on surface conductivity of diamond film," *AIP Advances*, vol. 5, no. 4, p. 041307, 2015.

[58] K. Tsugawa, H. Umezawa, and H. Kawarada, "Characterization of diamond surface-channel metal-semiconductor field-effect transistor with device simulation," *Japanese Journal of Applied Physics*, vol. 40, pp. 3101–3107, May 2001.

[59] J. Pernot, P. N. Volpe, F. Omnès, P. Muret, V. Mortet, K. Haenen, and T. Teraji, "Hall hole mobility in boron-doped homoepitaxial diamond," *Phys. Rev. B*, vol. 81, p. 205203, May 2010.

[60] M. N. Yoder, ch. 1, p. 4. Wiley, 1994.

[61] C. Nebel, F. Ertl, C. Sauerer, M. Stutzmann, C. Graeff, P. Bergonzo, O. Williams, and R. Jackman, "Low temperature properties of the p-type surface conductivity of diamond," *Diamond and Related Materials*, vol. 11, no. 3, pp. 351 – 354, 2002.

[62] E. Arnold, "Conduction mechanisms in bandtails at the si/sio2 interface," *Surface Science*, vol. 58, no. 1, pp. 60 – 70, 1976.

[63] T. Ando, K. Yamamoto, M. Ishii, M. Kamo, and Y. Sato, "Vapour-phase oxidation of diamond surfaces in o2 studied by diffuse reflectance fourier-transform infrared and temperture-programmed desorption spectroscopy," *J. Chem. Soc., Faraday Trans.*, vol. 89, pp. 3635–3640, 1993.

[64] Y. Yang, F. A. Koeck, M. Dutta, X. Wang, S. Chowdhury, and R. J. Nemanich, "Al2o3 dielectric layers on h-terminated diamond: Controlling surface conductivity," *Journal of Applied Physics*, vol. 122, no. 15, p. 155304, 2017.

[65] M. Riedel, J. Ristein, and L. Ley, "Recovery of surface conductivity of h-terminated diamond after thermal annealing in vacuum," *Phys. Rev. B*, vol. 69, p. 125338, Mar 2004.

[66] M. Geis, T. Fedynyshyn, M. Plaut, T. Wade, C. Wuorio, S. Vitale, J. Varghese, T. Grotjohn, R. Nemanich, and M. Hollis, "Chemical and semiconducting properties of no2-activated h-terminated diamond," *Diamond and Related Materials*, vol. 84, pp. 86–94, 2018.

[67] H. Sato and M. Kasu, "Electronic properties of h-terminated diamond during no2 and o3 adsorption and desorption," *Diamond and Related Materials*, vol. 24, pp. 99 – 103, 2012.

[68] K. Tsukioka and H. Okushi, "Hall mobility and scattering mechanism of holes in boron-doped homoepitaxial chemical vapor deposition diamond thin films," *Japanese Journal of Applied Physics*, vol. 45, pp. 8571–8577, nov 2006.

[69] M. Cardona and N. Christensen, "Deformation potentials of the direct gap of diamond," *Solid State Communications*, vol. 58, no. 7, pp. 421 – 424, 1986.

[70] A. Ortiz-Conde, F. G. Sánchez, J. J. Liou, A. Cerdeira, M. Estrada, and Y. Yue, "A review of recent mosfet threshold voltage extraction methods," *Microelectronics reliability*, vol. 42, no. 4-5, pp. 583–596, 2002.

[71] S. A. Russell, L. Cao, D. Qi, A. Tallaire, K. G. Crawford, A. T. Wee, and D. A. Moran, "Surface transfer doping of diamond by moo3: A combined spectroscopic and hall measurement study," *Applied Physics Letters*, vol. 103, no. 20, p. 202112, 2013.

[72] M. Kubovic and M. Kasu, "Improvement of hydrogen-terminated diamond field effect transistors in nitrogen dioxide atmosphere," *Applied Physics Express*, vol. 2, no. 8, p. 086502, 2009.

[73] K. Hirama, H. Sato, Y. Harada, H. Yamamoto, and M. Kasu, "Diamond field-effect transistors with 1.3 a/mm drain current density by al2o3 passivation layer," *Japanese Journal of Applied Physics*, vol. 51, no. 9R, p. 090112, 2012.

[74] J.-f. Zhang, Z.-y. Ren, J.-c. Zhang, C.-f. Zhang, D.-z. Chen, S.-r. Xu, Y. Li, and Y. Hao, "Characterization and mobility analysis of moo3-gated diamond mosfet," *Japanese Journal of Applied Physics*, vol. 56, no. 10, p. 100301, 2017.

[75] M. Groner, J. Elam, F. Fabreguette, and S. M. George, "Electrical characterization of thin al2o3 films grown by atomic layer deposition on silicon and various metal substrates," *Thin solid films*, vol. 413, no. 1-2, pp. 186–197, 2002.

[76] R. Winter, J. Ahn, P. C. McIntyre, and M. Eizenberg, "New method for determining flat-band voltage in high mobility semiconductors," *Journal of Vacuum Science & Technology B, Nanotechnology and Microelectronics: Materials, Processing, Measurement, and Phenomena*, vol. 31, no. 3, p. 030604, 2013.

[77] W. Adam, E. Berdermann, P. Bergonzo, G. Bertuccio, F. Bogani, E. Borchi, A. Brambilla, M. Bruzzi, C. Colledani, J. Conway, *et al.*, "Radiation tolerance of cvd diamond detectors for pions and protons," *Nuclear Instruments and Methods in Physics Research Section A: Accelerators, Spectrometers, Detectors and Associated Equipment*, vol. 476, no. 3, pp. 686–693, 2002.

[78] W. Adam, E. Berdermann, P. Bergonzo, G. Bertuccio, F. Bogani, E. Borchi, A. Brambilla, M. Bruzzi, C. Colledani, J. Conway, *et al.*, "Performance of irradiated cvd diamond micro-strip sensors," *Nuclear Instruments and Methods in Physics Research Section A: Accelerators, Spectrometers, Detectors and Associated Equipment*, vol. 476, no. 3, pp. 706–712, 2002.

[79] Y. Sato, T. Shimaoka, J. H. Kaneko, H. Murakami, M. Isobe, M. Osakabe, M. Tsubota, K. Ochiai, A. Chayahara, H. Umezawa, *et al.*, "Radiation hardness of a single crystal cvd diamond detector for mev energy protons," *Nuclear Instruments and Methods in Physics Research Section A: Accelerators, Spectrometers, Detectors and Associated Equipment*, vol. 784, pp. 147–150, 2015.

[80] I. Zamboni, Ž. Pastuović, and M. Jakšić, "Radiation hardness of single crystal cvd diamond detector tested with mev energy ions," *Diamond and related materials*, vol. 31, pp. 65–71, 2013.

[81] M. Bruzzi, M. Bucciolini, G. Cirrone, G. Cuttone, A. Guasti, S. Mazzocchi, S. Pirollo, M. Sabini, and S. Sciortino, "Characterization of cvd diamond films as radiation detectors for dosimetric applications," in *1999 IEEE Nuclear Science Symposium. Conference Record. 1999 Nuclear Science Symposium and Medical Imaging Conference (Cat. No. 99CH37019)*, vol. 1, pp. 121–124, IEEE, 1999.

[82] V. Grilj, N. Skukan, M. Jakšić, W. Kada, and T. Kamiya, "Irradiation of thin diamond detectors and radiation hardness tests using mev protons," *Nuclear Instruments and Methods in Physics Research Section B: Beam Interactions with Materials and Atoms*, vol. 306, pp. 191–194, 2013.

[83] J. Liu, J. Chang, G. Zhong, J. Zhang, X. Pang, and J. Jia, "Fabrication and performance of single crystal diamond neutron and gamma ray detectors," *AIP Advances*, vol. 9, no. 9, p. 095103, 2019.

[84] P. Bergonzo, D. Tromson, C. Mer, B. Guizard, F. Foulon, and A. Brambilla, "Particle and radiation detectors based on diamond," *physica status solidi (a)*, vol. 185, no. 1, pp. 167–181, 2001.

[85] Y. Yokota, H. Kotsuka, T. Sogi, J. Ma, A. Hiraki, H. Kawarada, K. Matsuda, and M. Hatada, "Formation of optical centers in cvd diamond by electron and neutron irradiation," *Diamond and Related Materials*, vol. 1, no. 5-6, pp. 470–477, 1992.

[86] C. Verona, W. Ciccognani, S. Colangeli, E. Limiti, M. Marinelli, G. Verona-Rinati, E. Santoni, M. Angelone, M. Pillon, F. Pompili, *et al.*, "14.8-mev neutron irradiation on h-terminated diamond-based mesfets," *IEEE Electron Device Letters*, vol. 37, no. 12, pp. 1597–1600, 2016.

[87] J. F. Ziegler, M. D. Ziegler, and J. P. Biersack, "Srim–the stopping and range of ions in matter (2010)," *Nuclear Instruments and Methods in Physics Research Section B: Beam Interactions with Materials and Atoms*, vol. 268, no. 11-12, pp. 1818–1823, 2010.

[88] J. R.-C. Hu, *Device technology for nanoscale III-V compound semiconductor field effect transistors*. PhD thesis, Stanford University, 2011.

[89] J. Rafí, G. Pellegrini, V. Fadeyev, Z. Galloway, H.-W. Sadrozinski, M. Christophersen, B. Phlips, D. Lynn, J. Kierstead, M. Hoeferkamp, *et al.*, "Gamma and proton irradiation effects and thermal stability of electrical characteristics of metal-oxide-silicon capacitors

with atomic layer deposited al2o3 dielectric," *Solid-State Electronics*, vol. 116, pp. 38–45, 2016.

[90] A. J. Suria, H. C. Chiamori, A. Shankar, and D. G. Senesky, "Capacitance-voltage characteristics of gamma irradiated al2o3, hfo2, and sio2 thin films grown by plasma-enhanced atomic layer deposition," in *Sensors for Extreme Harsh Environments II*, vol. 9491, p. 949105, International Society for Optics and Photonics, 2015.

[91] C. Manfredotti, S. Calusi, A. L. Giudice, L. Giuntini, M. Massi, P. Olivero, and A. Re, "Luminescence centers in proton irradiated single crystal cvd diamond," *Diamond and related materials*, vol. 19, no. 7-9, pp. 854–860, 2010.

[92] S. Pezzagna, D. Rogalla, D. Wildanger, J. Meijer, and A. Zaitsev, "Creation and nature of optical centres in diamond for single-photon emission—overview and critical remarks," *New Journal of Physics*, vol. 13, no. 3, p. 035024, 2011.

[93] S. Almaviva, M. Angelone, M. Marinelli, E. Milani, M. Pillon, G. Prestopino, A. Tucciarone, C. Verona, and G. Verona-Rinati, "Characterization of damage induced by heavy neutron irradiation on multilayered l 6 if-single crystal chemical vapor deposition diamond detectors," *Journal of Applied Physics*, vol. 106, no. 7, p. 073501, 2009.

[94] J. Steeds, T. Davis, S. Charles, J. Hayes, and J. Butler, "3h luminescence in electron-irradiated diamond samples and its relationship to self-interstitials," *Diamond and related materials*, vol. 8, no. 10, pp. 1847–1852, 1999.

[95] M. Krátká, O. Babchenko, E. Ukraintsev, J. Vachelová, M. Davídková, M. Vandrovcová, A. Kromka, and B. Rezek, "Gamma radiation effects on hydrogen-terminated nanocrystalline diamond bio-transistors," *Diamond and Related Materials*, vol. 63, pp. 186–191, 2016.

[96] J. Cui, R. Graupner, J. Ristein, and L. Ley, "Electron affinity and band bending of single crystal diamond (111) surface," *Diamond and related materials*, vol. 8, no. 2-5, pp. 748–753, 1999.

[97] R. P. Livi, "Adhesion enhancement induced by mev ion beams," *Nuclear Instruments and Methods in Physics Research Section B: Beam Interactions with Materials and Atoms*, vol. 10, pp. 545–548, 1985.

[98] B. Werner, T. Vreeland Jr, M. Mendenhall, Y. Qui, and T. Tombrello, "Enhanced adhesion from high energy ion irradiation," *Thin Solid Films*, vol. 104, no. 1-2, pp. 163–166, 1983.

[99] T. Tombrello, "The ubiquity of ch bond breaking by mev ion irradiation," *Nuclear Instruments and Methods in Physics Research Section B: Beam Interactions with Materials and Atoms*, vol. 24, pp. 517–521, 1987.

[100] T. Tombrello, "Surface modification using mev ion beams," *Nuclear Instruments and Methods in Physics Research*, vol. 218, no. 1-3, pp. 679–683, 1983.

[101] R. E. Johnson, *Interaction with Surfaces*, pp. 75–135. Berlin, Heidelberg: Springer Berlin Heidelberg, 1990.

[102] S. Allen Jr, D. Tsui, and F. DeRosa, "Frequency dependence of the electron conductivity in the silicon inversion layer in the metallic and localized regimes," *Physical Review Letters*, vol. 35, no. 20, p. 1359, 1975.

[103] T. Armstrong and B. Colborn, "Predictions of induced radioactivity for spacecraft in low earth orbit," *International Journal of Radiation Applications and Instrumentation. Part D. Nuclear Tracks and Radiation Measurements*, vol. 20, no. 1, pp. 101–130, 1992.

[104] S. S. Board, E. National Academies of Sciences, Medicine, *et al.*, *Thriving on our changing planet: A decadal strategy for Earth observation from space.* National Academies Press, 2019.

[105] S. Yamanaka, H. Watanabe, S. Masai, D. Takeuchi, H. Okushi, and K. Kajimura, "High-quality b-doped homoepitaxial diamond films using trimethylboron," *Japanese journal of applied physics*, vol. 37, no. 10A, p. L1129, 1998.

[106] P. G. Neudeck, R. Okojie, and L.-Y. Chen, "High-temperature electronics - a role for wide bandgap semiconductors?," *Proceedings of the IEEE*, vol. 90, pp. 1065–1076, 2002.

[107] M. Toulemonde, C. Dufour, A. Meftah, and E. Paumier, "Transient thermal processes in heavy ion irradiation of crystalline inorganic insulators," *Nuclear Instruments and Methods in Physics Research Section B: Beam Interactions with Materials and Atoms*, vol. 166-167, pp. 903 – 912, 2000.

[108] M. Toulemonde, W. Assmann, C. Dufour, A. Meftah, F. Studer, and C. Trautmann, "Experimental phenomena and thermal spike description of ion tracks in amorphisable inorganic insulators," *Mat. Fys. Medd*, pp. 263–292, 2006.

[109] P. Lopez, L. Pelaz, I. Santos, L. A. Marqués, and M. Aboy, "Molecular dynamics simulations of damage production by thermal spikes in Ge," *Journal of Applied Physics*, vol. 111, p. 033519, 2012.

[110] A. Benyagoub and A. Audren, "Mechanism of the swift heavy ion induced epitaxial recrystallization in predamaged silicon carbide," *Journal of Applied Physics*, vol. 106, p. 083516, 2009.

[111] Y. Zhang, R. Sachan, O. H. Pakarinen, M. F. Chisholm, P. Liu, H. Xue, and W. J. Weber, "Ionization-induced annealing of pre-existing defects in silicon carbide," *Nature Communications*, vol. 6, p. 8049, 2015.

[112] M. Backman, M. Toulemonde, O. Pakarinen, N. Juslin, F. Djurabekova, K. Nordlund, A. Debelle, and W. Weber, "Molecular dynamics simulations of swift heavy ion induced defect recovery in SiC," *Computational Materials Science*, vol. 67, pp. 261 – 265, 2013.

[113] S. Kuboyama, C. Kamezawa, N. Ikeda, T. Hirao, and H. Ohyama, "Anomalous charge collection in silicon carbide schottky barrier diodes and resulting permanent damage and single-event burnout," *IEEE Transactions on Nuclear Science*, vol. 53, pp. 3343–3348, Dec 2006.

[114] A. Javanainen, M. Turowski, K. F. Galloway, C. Nicklaw, V. Ferlet-Cavrois, A. Bosser, J. M. Lauenstein, M. Muschitiello, F. Pintacuda, R. A. Reed, R. D. Schrimpf, R. A. Weller, and A. Virtanen, "Heavy-ion-induced degradation in SiC schottky diodes: Incident angle and energy deposition dependence," *IEEE Transactions on Nuclear Science*, vol. 64, pp. 2031–2037, Aug 2017.

[115] C. Abbate, G. Busatto, P. Cova, N. Delmonte, F. Giuliani, F. Iannuzzo, A. Sanseverino, and F. Velardi, "Analysis of heavy ion irradiation induced thermal damage in SiC schottky diodes," *IEEE Transactions on Nuclear Science*, vol. 62, pp. 202–209, Feb 2015.

[116] R. Mewaldt, "Galactic cosmic ray composition and energy spectra," *Advances in Space Research*, vol. 14, pp. 737 – 747, 1994.

[117] R. Peterson and D. G. Senesky, "Modeling of radiation-induced defect recovery in 3c-sic under high field bias conditions," *Computational Materials Science*, vol. 161, pp. 10 – 15, 2019.

[118] A. Chettah, H. Kucal, Z. Wang, M. Kac, A. Meftah, and M. Toulemonde, "Behavior of crystalline silicon under huge electronic excitations: A transient thermal spike description," *Nuclear Instruments and Methods in Physics Research Section B: Beam Interactions with Materials and Atoms*, vol. 267, pp. 2719 – 2724, 2009. Proceedings of the 23rd International Conference on Atomic Collisions in Solids.

[119] L. L. Snead, T. Nozawa, Y. Katoh, T.-S. Byun, S. Kondo, and D. A. Petti, "Handbook of SiC properties for fuel performance modeling," *Journal of Nuclear Materials*, vol. 371, no. 1, pp. 329 – 377, 2007.

[120] J. Perl, J. Shin, J. Schümann, B. Faddegon, and H. Paganetti, "Topas: An innovative proton monte carlo platform for research and clinical applications," *Medical Physics*, vol. 39, pp. 6818–6837.

[121] M. Waligórski, R. Hamm, and R. Katz, "The radial distribution of dose around the path of a heavy ion in liquid water," *International Journal of Radiation Applications and Instrumentation. Part D. Nuclear Tracks and Radiation Measurements*, vol. 11, no. 6, pp. 309 – 319, 1986.

[122] M. Lundstrom, "Fundamentals of carrier transport, 2nd ed.," *Cambridge University Press, Cambridge*, 2000.

[123] D. Vasileska and S. M. Goodnick, "Computational electronics," *Synthesis Lectures Comput. Electromagn.*, pp. 139 – 175, 2005.

[124] K. Tsukioka, D. Vasileska, and D. Ferry *Physica B: Condensed Matter*, vol. 185, pp. 466–470, 1993.

[125] E. Pop, S. Sinha, and K. E. Goodson, "Heat generation and transport in nanometer-scale transistors," *Proceedings of the IEEE*, vol. 94, pp. 1587–1601, Aug 2006.

[126] H.-E. Nilsson, U. Englund, M. Hjelm, E. Bellotti, and K. Brennan, "Full band monte carlo study of high field transport in cubic phase silicon carbide," *Journal of Applied Physics*, vol. 93, pp. 3389–3394, 2003.

[127] J. F. Ziegler, M. Ziegler, and J. Biersack, "Srim – the stopping and range of ions in matter (2010)," *Nuclear Instruments and Methods in Physics Research Section B: Beam Interactions with Materials and Atoms*, vol. 268, pp. 1818 – 1823, 2010. 19th International Conference on Ion Beam Analysis.

[128] S. Plimpton, "Fast parallel algorithms for short-range molecular dynamics," *Journal of Computational Physics*, vol. 117, pp. 1 – 19, 1995.

[129] F. Gao and W. J. Weber, "Empirical potential approach for defect properties in 3C-SiC," *Nuclear Instruments and Methods in Physics Research Section B: Beam Interactions with Materials and Atoms*, vol. 191, pp. 504 – 508, 2002.

[130] F. Gao and W. J. Weber, "Recovery of close frenkel pairs produced by low energy recoils in sic," *Journal of Applied Physics*, vol. 94, no. 7, pp. 4348–4356, 2003.

[131] A. Debelle, M. Backman, L. Thomé, W. J. Weber, M. Toulemonde, S. Mylonas, A. Boulle, O. H. Pakarinen, N. Juslin, F. Djurabekova, K. Nordlund, F. Garrido, and D. Chaussende, "Combined experimental and computational study of the recrystallization process induced by electronic interactions of swift heavy ions with silicon carbide crystals," *Phys. Rev. B*, vol. 86, p. 100102, Sep 2012.

[132] G. Lucas and L. Pizzagalli, "Theoretical study of the recombination of frenkel pairs in irradiated silicon carbide," *Journal of Physics: Condensed Matter*, vol. 19, no. 8, p. 086208, 2007.

[133] M.-J. Zheng, N. Swaminathan, D. Morgan, and I. Szlufarska, "Energy barriers for point-defect reactions in 3*c*-sic," *Phys. Rev. B*, vol. 88, p. 054105, Aug 2013.

[134] G. Lucas, M. Bertolus, and L. Pizzagalli, "An environment-dependent interatomic potential for silicon carbide: calculation of bulk properties, high-pressure phases, point and extended defects, and amorphous structures," *Journal of Physics: Condensed Matter*, vol. 22, no. 3, p. 035802, 2010.

[135] G. D. Badhwar, "The radiation environment in low-earth orbit," *Radiation Research*, vol. 148, pp. S3–S10, 1997.

[136] D. R. Sahoo, I. Szlufarska, D. Morgan, and N. Swaminathan, "Role of pre-existing point defects on primary damage production and amorphization in silicon carbide (-SiC)," *Nuclear Instruments and Methods in Physics Research Section B: Beam Interactions with Materials and Atoms*, vol. 414, pp. 45 – 60, 2018.

[137] G. Samolyuk, Y. Osetsky, and R. Stoller, "Molecular dynamics modeling of atomic displacement cascades in 3C-SiC: Comparison of interatomic potentials," *Journal of Nuclear Materials*, vol. 465, pp. 83 – 88, 2015.

[138] A. Meftah, F. Brisard, J. M. Costantini, M. Hage-Ali, J. P. Stoquert, F. Studer, and M. Toulemonde, "Swift heavy ions in magnetic insulators: A damage-cross-section velocity effect," *Phys. Rev. B*, vol. 48, pp. 920–925, Jul 1993.

[139] Y. Sasama, K. Komatsu, S. Moriyama, M. Imura, T. Teraji, K. Watanabe, T. Taniguchi, T. Uchihashi, and Y. Takahide, "High-mobility diamond field effect transistor with a monocrystalline h-bn gate dielectric," *APL Materials*, vol. 6, no. 11, p. 111105, 2018.

[140] P. Bergonzo, D. Tromson, C. Mer, B. Guizard, F. Foulon, and A. Brambilla, "Particle and radiation detectors based on diamond," *physica status solidi (a)*, vol. 185, no. 1, pp. 167–181, 2001.

[141] M.-L. Hicks, A. C. Pakpour-Tabrizi, V. Zuerbig, L. Kirste, C. Nebel, and R. B. Jackman, "Optimizing reactive ion etching to remove sub-surface polishing damage on diamond," *Journal of Applied Physics*, vol. 125, no. 24, p. 244502, 2019.

[142] S. Birner, T. Zibold, T. Andlauer, T. Kubis, M. Sabathil, A. Trellakis, and P. Vogl, "nextnano: General purpose 3-d simulations," *IEEE Transactions on Electron Devices*, vol. 54, no. 9, pp. 2137–2142, 2007.

[143] M. Dankerl, A. Lippert, S. Birner, E. U. Stützel, M. Stutzmann, and J. A. Garrido, "Hydrophobic interaction and charge accumulation at the diamond-electrolyte interface," *Phys. Rev. Lett.*, vol. 106, p. 196103, May 2011.

[144] A. N. Newell, D. A. Dowdell, and D. H. Santamore, "Surface effects on nitrogen vacancy centers neutralization in diamond," *Journal of Applied Physics*, vol. 120, no. 18, p. 185104, 2016.

[145] N. Naka, K. Fukai, Y. Handa, and I. Akimoto, "Direct measurement via cyclotron resonance of the carrier effective masses in pristine diamond," *Phys. Rev. B*, vol. 88, p. 035205, Jul 2013.

[146] C. J. Rauch, "Millimeter cyclotron resonance experiments in diamond," *Phys. Rev. Lett.*, vol. 7, pp. 83–84, Aug 1961.

[147] G. Dresselhaus, A. F. Kip, and C. Kittel, "Cyclotron resonance of electrons and holes in silicon and germanium crystals," *Phys. Rev.*, vol. 98, pp. 368–384, Apr 1955.

[148] Y. Takahide, H. Okazaki, K. Deguchi, S. Uji, H. Takeya, Y. Takano, H. Tsuboi, and H. Kawarada, "Quantum oscillations of the two-dimensional hole gas at atomically flat diamond surfaces," *Phys. Rev. B*, vol. 89, p. 235304, Jun 2014.

[149] J. H. Davies, pp. 329–370. Cambridge University Press, 1997.

[150] T. Ando, A. B. Fowler, and F. Stern, "Electronic properties of two-dimensional systems," *Rev. Mod. Phys.*, vol. 54, pp. 437–672, Apr 1982.

[151] C. Hamaguchi, pp. 265–364. Springer International Publishing, 2017.